12-2016

Thermomechanical properties of novel lanthanum zirconate based thermal barrier coatings - an integrated experimental and modeling study

Xingye Guo
Purdue University

Recommended Citation

Guo, Xingye, "Thermomechanical properties of novel lanthanum zirconate based thermal barrier coatings - an integrated experimental and modeling study" (2016). *Open Access Dissertations*. 928.
https://docs.lib.purdue.edu/open_access_dissertations/928

Graduate School Form
30 Updated 12/26/2015

PURDUE UNIVERSITY
GRADUATE SCHOOL
Thesis/Dissertation Acceptance

This is to certify that the thesis/dissertation prepared

By Xingye Guo

Entitled
THERMOMECHANICAL PROPERTIES OF NOVEL LANTHANUM ZIRCONATE BASED THERMAL BARRIER COATINGS – AN INTEGRATED EXPERIMENTAL AND MODELING STUDY

For the degree of Doctor of Philosophy

Is approved by the final examining committee:

Jing Zhang
Co-chair

Yung C. Shin
Co-chair

Fu Zhao

Peter J. Schubert

To the best of my knowledge and as understood by the student in the Thesis/Dissertation Agreement, Publication Delay, and Certification Disclaimer (Graduate School Form 32), this thesis/dissertation adheres to the provisions of Purdue University's "Policy of Integrity in Research" and the use of copyright material.

Approved by Major Professor(s): Jing Zhang, Yung C. Shin

Approved by: Jay P. Gore 11/28/2016
Head of the Departmental Graduate Program Date

THERMOMECHANICAL PROPERTIES OF NOVEL LANTHANUM ZIRCONATE BASED THERMAL BARRIER COATINGS – AN INTEGRATED EXPERIMENTAL AND MODELING STUDY

A Dissertation

Submitted to the Faculty

of

Purdue University

by

Xingye Guo

In Partial Fulfillment of the

Requirements for the Degree

of

Doctor of Philosophy

December 2016

Purdue University

West Lafayette, Indiana

Dedicated to my family.

ACKNOWLEDGMENTS

I would like to express my sincere appreciation for my academic advisor, Professor Jing Zhang, and Professor Yung C. Shin, for their expert advice, valuable guidance, and kind support during my study and research at Purdue. I would also like to thank my committee members Professor Peter Schubert and Professor Fu Zhao, for serving on my committee, and great help for my studies.

I am thankful to my collaborators Professor Yeon-Gil Jung from Changwon National University, Dr. Li Li and Dr. James Knapp from Praxair Surface Technologies, and Dr. Yang Ren from Argonne National Laboratory, who helped me in the thermal barrier coating project and inspired me through effective advice and fruitful discussions. I would like to thank the financial support provided by the U.S. Department of Energy (Award Number: DE-FE0008868; Project Title: Novel Functionally Graded Thermal Barrier Coatings in Coal-fired Power Plant Turbines; Program Manager: Richard Dunst). I would like to thank Michael Golub, for his help in my experiments. I also would like to thank my lab mates Linmin Wu, Yi Zhang, Jiayang Liu, Weng Hoh Lee, and many others, who gave me help in many aspects.

Finally, I would like to thank my wife and my parents, for their love and support during my doctoral studies and in my whole life.

TABLE OF CONTENTS

LIST OF TABLES

LIST OF FIGURES

ABSTRACT

Guo, Xingye. Ph.D., Purdue University, December 2016. Thermomechanical Properties of Novel Lanthanum Zirconate Based Thermal Barrier Coatings – An Integrated Experimental and Modeling Study. Major Professors: Jing Zhang, School of Engineering and Technology and Yung C. Shin, School of Mechanical Engineering.

Thermal barrier coatings (TBCs) are refractory materials deposited on gas turbine components, which provide thermal protection for metallic components at operating conditions. The current state-of-art TBC material is yttria-stabilized zirconia (YSZ), whose service temperature is limited to 1200 °C, due to sintering and phase transition at higher temperatures. In comparison, lanthanum zirconate ($La_2Zr_2O_7$, LZ) has become a promising candidate material for TBCs due to its lower thermal conductivity and higher phase stability compared to YSZ.

The primary objective of this thesis is to design a novel robust LZ-based TBC system suitable for applications beyond 1200 °C. Due to LZ' s low coefficient of thermal expansion and fracture toughness, which cause poor thermal cycling performance, two TBC architectures are proposed: (1) multiple layered coating, and (2) LZ/8YSZ composite coating.

In this work, LZ powders are fabricated using the solid-state reaction method, and all of the coatings are deposited using air plasma spray (APS) technique. The physical, thermal and mechanical properties of the sprayed LZ coatings have been systematically investigated, including temperature-dependent thermal conductivity, coefficient of thermal expansion, density, hardness, Young' s modulus, bond strength, and erosion resistance. The durability of the coatings in various thermal and mechanical conditions is also investigated, including furnace cycling test, thermal gradient mechanical fatigue test, and jet engine thermal shock test. The results show that for the layered TBCs, porous YSZ + LZ has reasonably good thermal cycling performance. For the composite TBCs, LZ/8YSZ (vol. % is 50:50) with a thin buffer layer LZ/8YSZ (vol. % is 25:75) has the greatest thermal cycling performance, comparable to pure 8YSZ coatings. The improved performance is explained by graded coefficient of thermal expansion and enhanced fracture toughness.

In parallel to experimental investigations, a multi-scale modeling approach is employed to study the fundamental thermal and mechanical properties of LZ crystal and coatings. Physics-based models are developed, including using density functional theory (DFT), molecular dynamics (MD), and finite element (FE) methods. The nanoscale tensile and shear deformations of LZ single crystal are simulated using DFT calculations with the generalized gradient approximation (GGA) functional. The anisotropic Young' s moduli are studied using two approaches: (1) stress-strain curve of large deformation, and (2) analytical method in small deformation. Additionally, the nanoscale tensile and shear large deformations of LZ single crystal are simulated using the MD method with Buckingham and Coulomb potentials at room temperature (300K). Both DFT and MD results show that LZ has strong anisotropic Young' s modulus with the ranking [111] > [110] > [100]. The shear modulus in {111}<110> direction is slightly larger than that in $\{111\}\langle 11\bar{2}\rangle$ direction. Both Bader charge transfer and electron charge density analyses indicate that the electron interactions between O and Zr ions in LZ are stronger in [111] for tensile and in {111}<110> for shear deformation.

For thermal properties, the temperature-dependent thermal conductivities of LZ coating are calculated using a multiscale approach. First, the thermal conductivity of LZ single crystal is calculated using a reverse non-equilibrium molecular dynamics (reverse NEMD) approach. The single crystal data is then passed to an FE model which takes into account realistic TBC microstructures. The predicted thermal conductivities from the FE model are in good agreement with experimental validations using both flash laser technique and pulsed thermal imaging-multilayer analysis.

Furthermore, the mechanical properties at the ceramic-metal (C-M) interface in TBCs are investigated. The nanoscale tensile and shear deformations of the ZrO_2/Ni interface, an approximation of the interface between the top and bond coats, are performed using both DFT and MD calculations. The DFT results indicate that the elastic modulus, ultimate strength, and toughness of the C-M interface increase with the decrease of the Ni layer thickness. The charge transfer analysis and the charge density distribution show that a thin interface layer exhibits a strong interaction between Ni and O ions. The MD simulations using COMB3 potential show that the Young' s modulus of ZrO_2/Ni interface in [111] direction is larger than that in [100] direction, and the shear modulus in $\{111\}<110>$ direction is larger than that in $\{111\}<11\bar{2}>$ direction.

In summary, this thesis work provides important thermomechanical properties of LZ-based thermal barrier coatings and can serve as a design tool for future advanced coating systems.

CHAPTER 1. BACKGROUND AND LITERATURE REVIEW

1.1 Thermal Barrier Coatings

The development of gas turbine engines relates to a great variety of engineering disciplines including turbine design, combustion, and cutting-edge materials. The application of thermal barrier coatings (TBCs) on turbine components has dramatically increased the operation temperature and lifetime of the alloy components in gas turbine engine [1]. The engine efficiency of gas turbines is increased due to the increase of operation temperature [2]. TBCs were initially introduced to the gas-turbine industry in the mid-70s [3]. Nowadays, TBCs are widely used in aeronautics, astronautics, motor industry, and heat power stations. They are extensively applied in high-temperature components of gas turbines to protect the surface of metallic parts, such as combustor wall, rotating blades, stationary guide vanes, blade outer air seals, and afterburners in the tail section of jet engines and so on, because, in general, superalloy materials used as substrate of high-temperature components have a temperature allowance below 1100 °C [4–7]. TBCs are multi-layered coating systems deposited on the turbine components, especially the turbine blade, which can thermally insulate them and protect them against the hot and corrosive gas stream [1,6,8].

The typical structure of the TBCs includes four layers: (1) superalloy substrate, (2) bond coat, (3) thermally grown oxide (TGO), and (4) ceramic top coat. The bond coat consists of an MCrAlN intermetallic alloy with a thickness of 100 - 300 μm, wherein the M is an element selected from nickel, cobalt, iron and their mixture, and the N is an element selected from yttrium, zirconium, hafnium, ytterbium and mixture thereof [9]. Typically, it can be deposited directly on the substrate using various techniques, such as air plasma spraying (APS), high velocity oxygen-fuel (HVOF) spraying, vacuum plasma spraying, low-pressure plasma spraying and diffusion deposition method [10–13]. In high-temperature operation conditions, the bond coat is inevitably oxidized and a TGO layer is formed at the interface between the bond and the top coats with a thickness of 1 – 10 μm. The main composition of TGO is α-alumina (α-Al_2O_3), which can work as a good oxygen diffusion barrier to protect the bond coat and substrate from further oxidation. On the other hand, the growth of the TGO layer can lead to TBC failure [14]. The ceramic top coat is one or multiple low thermal conductivity ceramic layers with a typical thickness of 100 - 600 μm, which is deposited by the APS or electron-beam physical vapor deposition (EB-PVD) methods [5, 8]. The criteria for TBCs material selection include high melting point, low thermal conductivity, high CTEs, good thermal and chemical stability, no phase change, low sintering activity, good erosion resistance and good foreign objective damage (FOD) or calciummagnesiumalumino-silicate (CMAS) resistance [15].

Currently, the state-of-the-art TBCs are 7 – 8 wt % yttria (Y_2O_3) stabilized zirconia (ZrO_2) (8YSZ). The 8YSZ has a metastable tetragonal phase (t'), and Y_2O_3 is used to stabilize the ZrO_2 structure. The 8YSZ has a relatively high melting point (2680 °C) [15], relatively low thermal conductivity about 2.0 - 2.3 W/m/K around 1000 °C for a fully dense status (0.9 - 1.2 W/m/K for 10 - 15 % porosity) [16, 17], a relatively high CTEs (11×10^{-6} K^{-1} at 1273 K) [15], and good thermal and chemical stability [18]. However, the maximum surface temperature that can be employed as TBCs of 8YSZ is limited to 1200 °C for long-time operation. At temperatures above 1200 °C, there are two important degradation mechanisms in 8YSZ. The first mechanism is that the t phase of YSZ will decompose to two equilibriums tetragonal (t) and cubic (c) phases. During the cooling process, the t phase will transform to the monoclinic (m) phase, accompany with ~4 % volume expansion. Another mechanism is the sintering of coating, which will change the microstructure as well as the mechanical and thermal properties. These phase and microstructure changes as well as the thermal and mechanical properties changes will finally lead to high thermal induced stress and shorten the coating's lifetime [15]. However, some approaches can be chosen to enhance TBCs' performance: 1) find a new the feedstock powder with a higher sintering resistance or no phase change, 2) control the porosity of TBCs [19]. In addition, increase the thickness of top coat can reduce the substrate temperature, although the performance of TBC still keeps same.

Lanthanum zirconate ($La_2Zr_2O_7$, LZ) is a typical pyrochlore structure ceramic material. The general chemical formula of the pyrochlore structure is $A_2B_2O_7$. The A element in $A_2B_2O_7$ generally is a rare earth or an element with an inert single pair of electrons, and the B element typically is a transition metal or a post-transition metal with a variable oxidation state [10, 20]. Compared to the 8YSZ, the LZ has many advantages for the application of TBCs: (1) no phase transformation from room temperature to its melting temperature, (2) considerably high sintering resistance, (3) a very low thermal conductivity (1.5 - 1.8 W/m/K at 1000 °C for a fully dense material), (4) the LZ has a lower oxygen ion diffusivity, which protects the bond coat and the substrate from oxidation [15]. The principle drawback of the LZ is its small CTE, which does not match the high CTE of the bond coat.

In this introduction chapter, the fabrication technique, physical, thermal and mechanical properties of the LZ coating are summarized, and the advantages and disadvantages of LZ for TBC application are described by comparison of YSZ coating. At the last, the modeling techniques with respect to the LZ coating properties and the coating failure mechanism are also reviewed.

1.2 Fabrication and Characterization of LZ Powder

1.2.1 Powder Fabrication

There are several ways to fabricate the LZ powder, which can be used in thermal spray process, including solid state reaction method, co-precipitation method and the sol-gel method, etc. [15, 21–23].

The LZ powder can be synthesized by the solid state reaction method from a mixture of the lanthanum oxide (La_2O_3, 99.9 %) and ZrO_2 (99 %) powders at high temperatures (T=1773 K) under an argon atmosphere for 10 hrs [21, 22]. The pure

La_2O_3 is typically prepared by dissolving $La_2(CO_3)_38H_2O$ in nitric acid and subsequently producing a precipitate by an addition of NH_3. The precipitate is dried in air and then heated in oxygen at 1173 K to remove the nitrogen-containing fragments. The resulting La_2O_3 is heated at 1473 K to remove any absorbed water [21]. The LZ powder is the spherical or ellipsoidal shape with a porous microstructure on the surface. The theoretical chemical composition of LZ powder coating is La 48.6 wt%, Zr 31.9 wt%, O 19.5 wt%, which is equivalent to the 1:2 molar ratios of La_2O_3 and ZrO_2 [18].

In the co-precipitation method, an aqueous solution of lanthanum nitrate hexahydrate ($La(NO_3)_36H_2O$) and zirconium oxychloride ($ZrOCl_28H_2O$) with a diluted NH_3 solution is used to prepare LZ powder [15]. During this preparation process, the $La(NO_3)_36H_2O$ and $ZrOCl_28H_2O$ is dissolved in a distilled water in equimolar amounts. The liquid mixtures are slowly added under stirring to an ammonium hydrate solution with pH 12.5. The resulting precipitate is filtered, washed with distilled water, and then dried at 120 °C overnight. The remaining solid is then calcined at 900 °C for 5 hrs.

The sol-gel method is another way to synthesize nanostructured powders, which have high sintering ability for the $A_2Zr_2O_7$ (A=La, Nd, Sm) system [23]. Tang et al. fabricated LZ fibers by a sol-gel combined electrospinning method [24]. $LaCl_37H_2O$ (9 mmol) was dissolved in the zirconium acetate solution in an equimolar ratio, and 0.4 g silica sol (SiO_2, 22%, pH=3.2) was added with magnetic stirring for 6 hrs. The transparent sol was added to absolute ethanol (8.0 ml) with Polyvinylpyrrolidone (PVP, 0.4g). The sol was transferred into a syringe and 20 kV power was supplied between the syringe tip and a stainless steel collector. The LZ gel fiber was fabricated on the collector under the electrostatic force, after the dry and calcination in high temperatures.

In addition to the aforementioned three commonly used methods, other methods also can fabricate LZ powders. Tong et al. prepared the LZ nano-powder using the stearic acid combustion method [25]. $La(NO_3)_3nH_2O$ and $Zr(NO_3)_49H_2O$ were used as the precursors, and stearic acid ($C_{17}H_{35}COOH$) was used as the solvent and dispersant. The mixed solution was ignited in the air, and the obtained powder was calcined at a series of increasing temperatures ranging from 600 - 900 °C for 5 hrs in the air.

1.2.2 Crystal Structure

The LZ is a typical ZrO_2-Ln_2O_3 (Ln is lanthanide elements, Ln= La → Gd) system, which has a pyrochlore structure with space group $Fd3\bar{m}$ [26]. Although the compounds $Ln_2Zr_2O_7$ (Ln=La → Gd) are stable at room temperatures, an order-disorder transition occurs at high temperature (>1500 °C), namely the compounds transfer from pyrochlore to defect fluorite structure, with the only exception of LZ (actually $Ln_2Zr_2O_7$, Ln=Tb → Lu adopt the defect fluorite structure) [20]. The transition temperature depends on the radius of Ln ions (La, no transition; Nd, 2300 °C, Sm 2000 °C, and Gd 1530 °C) [27].

X-ray diffraction is widely used to identify the crystal structures. Figure 1.1 shows the X-ray diffraction patterns of several $Ln_2Zr_2O_7$ materials at room temperature [23]. Two peaks indexed (331) and (511) shown in the LZ pattern originate from the pyrochlore structure, and are also observed in $Nd_2Zr_2O_7$, $Sm_2Zr_2O_7$, and $Gd_2Zr_2O_7$ patterns. Other peaks are commonly observed for the pyrochlore and defect fluorite structures [23].

The $Ln_2Zr_2O_7$ pyrochlore crystal is a cubic structure in space group $Fd3\bar{m}$ (origin choice 2) with four crystallographically independent atom sites (rear earth ion Ln, in 16d at (1/2, 1/2, 1/2) , Zr in 16c at (0, 0, 0), O1 in 48f at (x, 1/8, 1/8) and O2 in 8b at (3/8, 3/8, 3/8). The structure type can be considered as an ordered defect fluorite structure with the trivalent rare earth Ln^3+ and quadrivalent Zr^4+ cations forming an ordered, face-centered cubic eutectic cation array. Oxygen ions are located in 7/8 of the tetrahedral interstices: O1 in an off-center position within the Ln_2Zr_2 tetrahedral, O2 in the Zr tetrahedral [28]. The x values of O1

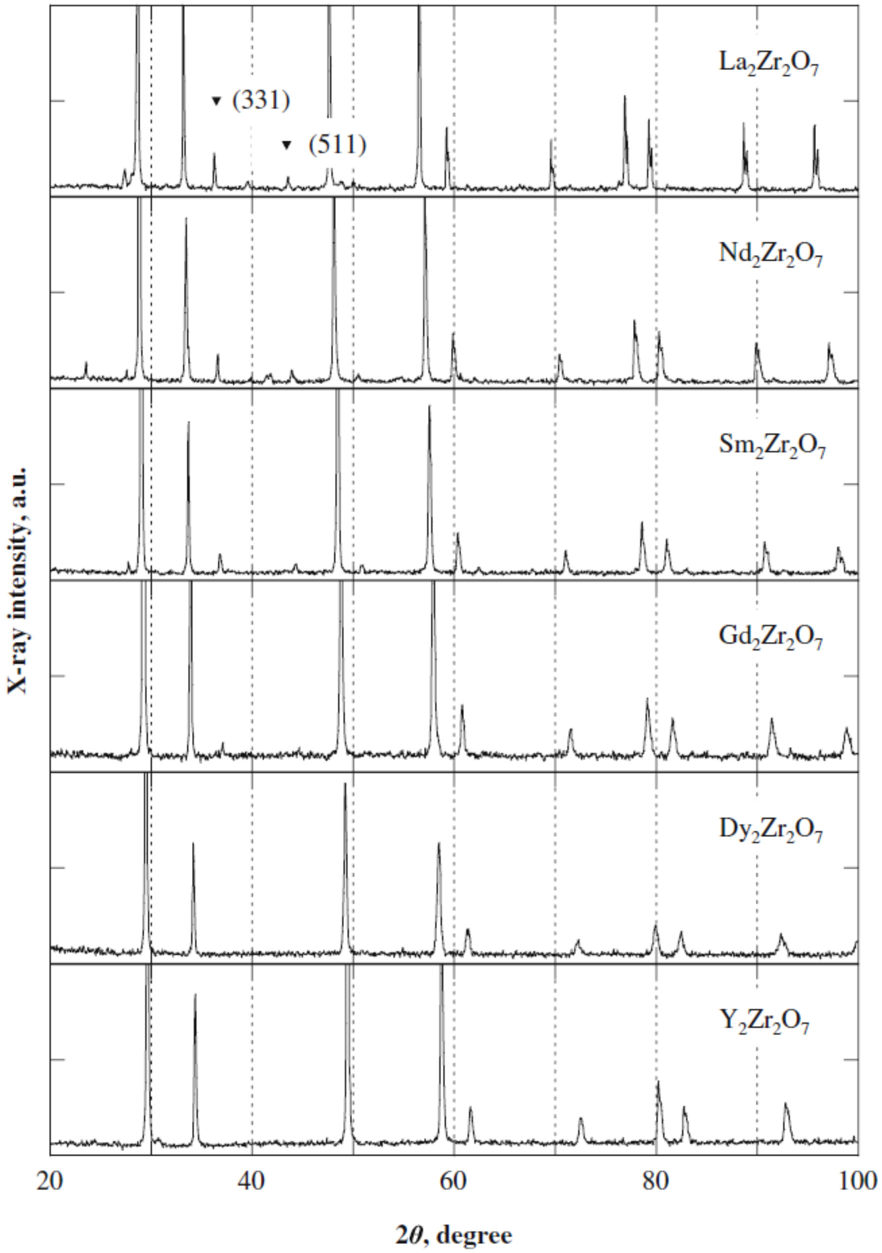

Figure 1.1. X-ray diffraction patterns of $Ln_2Zr_2O_7$ [23].

can be varied from 0.3125 to 0.375. The x values 0.3125 and 0.375 correspond to the regular octahedral oxygen environment around the Zr^4+ ion and regular cubic oxygen environment around Ln^3+ respectively. Tabira et al. determined the x value of LZ using systematic row wide-angle convergent beam electron diffraction (CBED) techniques [28]. The results showed that the x value varied systematically with the rare earth ion radius, the larger radius corresponding to the larger x value. The experimental result of x value in LZ is 0.333, according to Tabiras work [28].

The lattice parameter of a conventional cubic LZ cell can be calculated using XRD results based on Braggs Law [29]. Shimamura et al. reported that the lattice parameters of $Ln_2Zr_2O_7$ pyrochlores increased with the ionic radius of Ln, as shown in Figure 1.2 [23]. The lattice parameter of LZ is 10.8 Å in Shimamuras experiments, and 10.802 Å in Tabiras work [28].

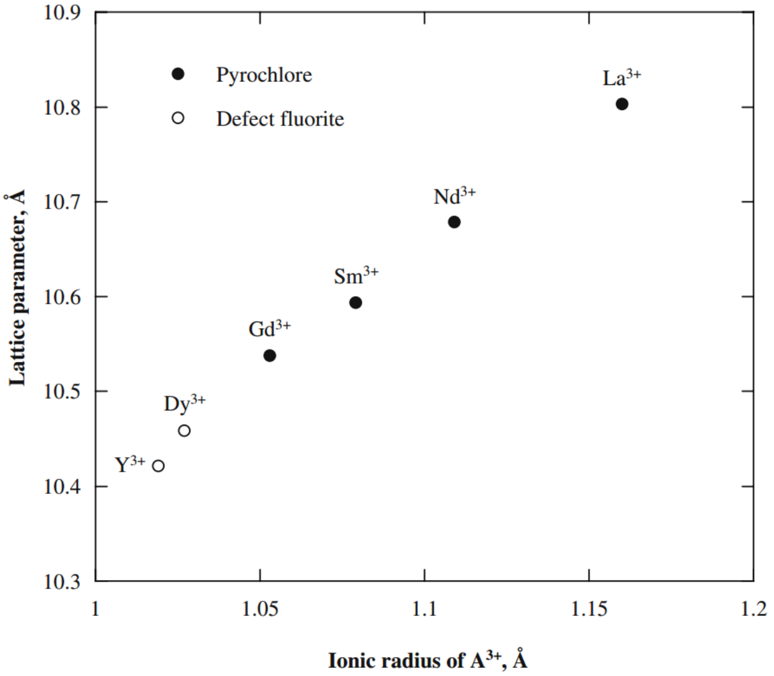

Figure 1.2. Lattice parameters of $Ln_2Zr_2O_7$ as a function of ionic radius of Ln. Solid and open symbols stand for pyrochlore and defect fluorite structures, respectively [23].

As discussed from the XRD pattern in Figure 1.1, the LZ has a cubic phase at room temperature. As shown in the $ZrO_2 - La_2O_3$ phase diagram of Figure 1.3, the LZ has no phase transformation from room temperature to its melting point [30–32]. When the molar ratio of ZrO_2 and La_2O_3 reaches 2:1, which corresponds to 33.3 %

La_2O_3, only a single LZ cubic phase is available from room temperature to its melting point.

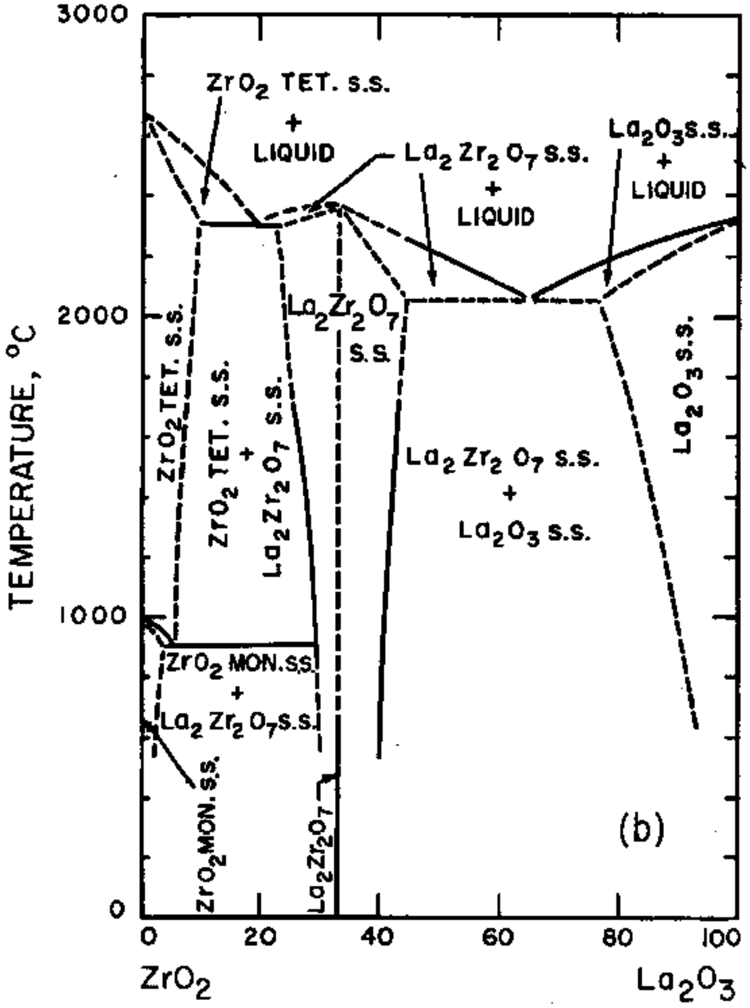

Figure 1.3. Phase diagram of ZrO_2 and La_2O_3 in mole percentage [30–32].

1.3 LZ Coating Deposition and Physical Properties

1.3.1 LZ Coating Deposition Techniques

APS is the most widely used thermal spray technique for LZ deposition. Plasma normally consists of neutral atoms, positive ions, and free electrons. Plasma is produced by transferring energy into the gas until the energy level is large enough to ionize the gas, allowing the electrons and ions to move independently of one another. As a result, plasma is often called the fourth state of matter. The plasma state is achieved when the current can be sustained under an electric field and the free electron can move through the ionized gas [10]. The plasma temperature in the core of the heating gas exceeds 20 000 °C, which depends on the gas properties. During the APS process, feedstock powders are carried by some noble gasses, such as argon and nitrogen, to the APS torch. The thermal plasma can be generated using electric arcs. Natural air can be used as the source of the plasma gas for the LZ spray. The essential APS parameters include current, carrier air flow rate, primary air flow rate, spray distance, powder feed rate, substrate tangential speed, etc. [33].

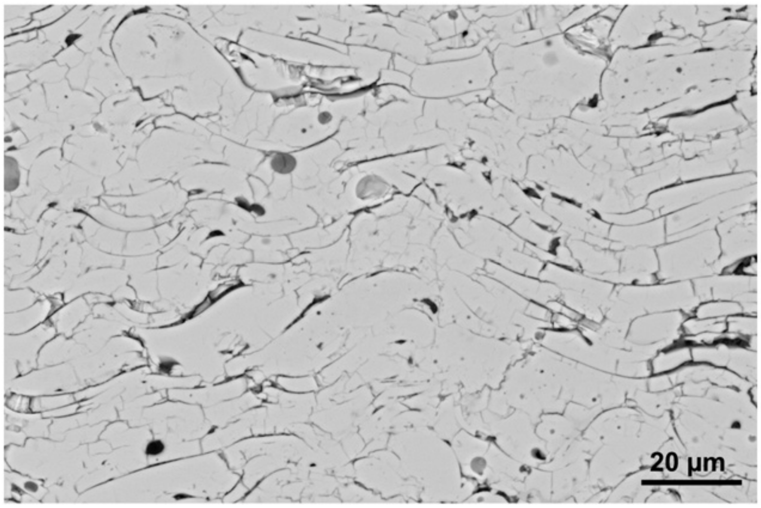

Figure 1.4. Cross-sectional microstructure of APS sprayed LZ coating [33].

As shown in Figure 1.4, the APS sprayed LZ has many amorphous pores and cracks, which is well known as the "splat" grain [33]. The thermal conductivity of the APS deposited coating is lower than the EB-PVD deposited one, due to its splat grain morphology. The porosity of the LZ coating can be easily controlled by changing the spray parameters, which results in changing the thermal and mechanical properties.

Another commonly used deposition technology is EB-PVD. The term PVD denotes those vacuum deposition processes where the coating material is evaporated by various mechanisms (resistant heating, high-energy ionized gas bombardment, or electron gun) under vacuum, and the vapor phase is transported to the substrate, forming a coating [34]. The main EB-PVD deposition parameters include vacuum pressure, substrate distance, power supply, average substrate temperature (1223 ± 25 K, 950 ± 25 °C) and substrate rotate speed, etc. [35,36]. As shown in Figure 1.5, the EB-PVD deposited LZ coating microstructure has a fine columnar microstructure that results in a higher strain tolerance [37]. Typically, the EB-PVD deposited coating has a higher thermal conductivity than APS sprayed coatings in the same porosity level. Because the splat boundaries of APS deposited coating act as scattering centers perpendicular to the direction of heat flux, which weaken the heat transfer. However, the columnar grain boundaries in EB-PVD deposited coating are parallel to the direction of heat flux. As a result, the EB-PVD deposited coating has a good performance and considerably longer operating lifetimes [12].

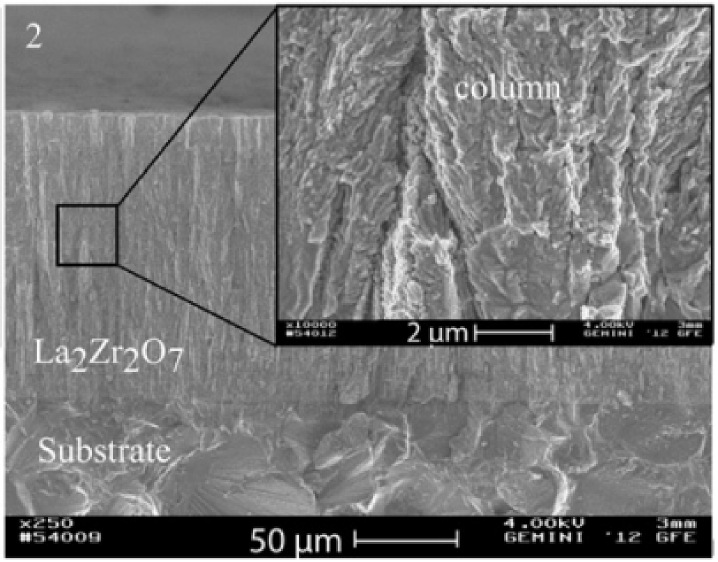

Figure 1.5. Cross-sectional microstructure of EB-PVD deposited LZ coating [37].

However, the main disadvantages of EB-PVD technique are its low deposition rate, high investment costs, high thermal conductivity, and vapor pressure requirements.

In addition to the two methods mentioned above, there are other techniques to deposit LZ coatings, such as suspension plasma spray (SPS) and spray pyrolysis [12, 38, 39].

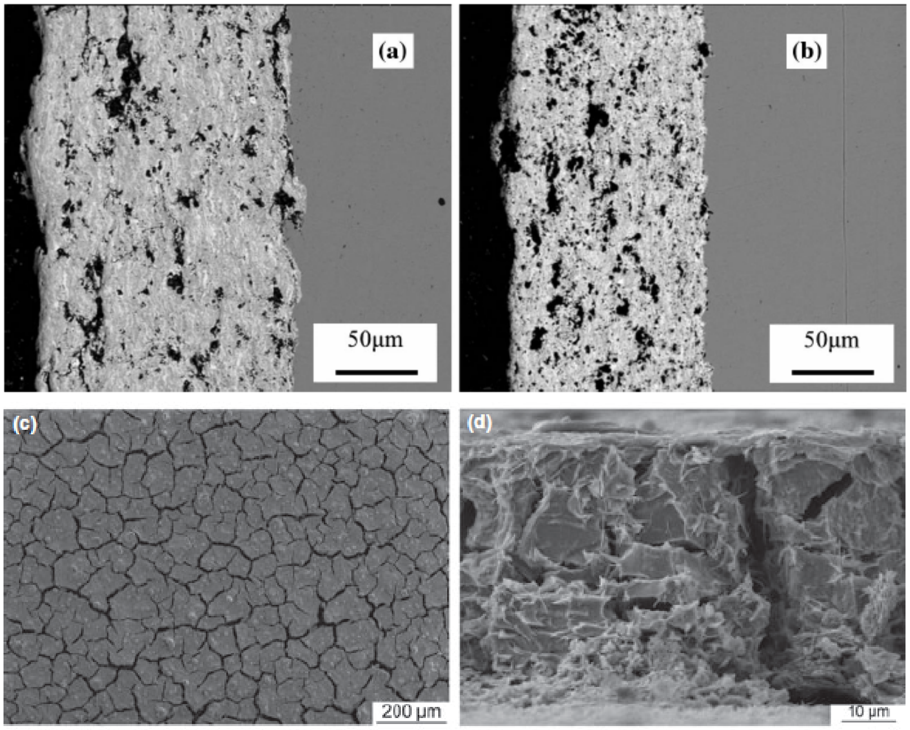

Figure 1.6. Cross-sectional microstructure of LZ coatings (a) SPS deposited with standoff 40 mm, (b) SPS deposited with standoff 50 mm, (c) surface view, and (d) cross section view of spray pyrolysis deposited LZ coatings [38, 39].

Wang et al. deposited a LZ coating using the SPS method [38]. The suspension of 30 wt.% nano-LZ particles in (99.5 %) ethanol was produced. Meanwhile, an electrostatic dispersant of 1 wt.% polyethylene glycol (PEG 1000) was added to the suspension. The suspension was injected into the plasma spray jet and the LZ coating was deposited. The main deposition parameters are standoff distance of the substrate and the concentration of the suspension feedstock. A liquid solution was used as a feedstock material instead of powder, which provide the possibility of tailoring the coating composition easily and facilitating the doped, multilayered and graded coatings [39]. As shown in Figure 1.6a and Figure 1.6b, many pores and cracks were spotted in the microstructure of SPS deposited coatings [38]. Weber et al. fabricated the LZ coating using the spray pyrolysis method [39]. Zirconyl oxynitrate hydrate ($ZrO(NO_3)_2{\cdot}xH_2O$) and lanthanum nitrate hexahydrate ($La(NO_3)_3{\cdot}6H_2O$) were dissolved in deionized water and further mixed in a molar ratio of 1:1 of La to Zr. The precursor solution was sprayed at the flow rate of 1 ml/min at 240 °C. The deposited coatings were dried at 500 – 600 °C after the deposition process. As shown in Figure 1.6a and Figure 1.6b, a lot of cracks were observed in the coating layer [39].

1.3.2 Coating Density and Porosity Measurements

The theoretical density of LZ material can be calculated using the molecular weight and the number of formula units per elementary cell [40]. Lehmann et al. calculated the theoretical density of LZ material as 6050 kg/m^3 [40]

The porous LZ coating density can be measured following the ASTM standard B328-96, which is based on the Archimedes' principle [41]. Free standing samples, which were peeled off from the substrate without the bond coat, were used in the coating density measurements. Engine oil was used to seal the pores on the sample surface by dipping the sample with the oil, so the volume of the sample can be measured by Archimedes' principle. Density (D, g/cm^3) of the sample can be calculated by [41]:

$$D = \frac{A}{(B - C + E)} D_w \tag{1.1}$$

where A is the mass of oil-free specimen in the air, B is mass of oil-impregnated specimen, C is mass of oil-impregnated specimen and wire in water, E is the mass of wire in water, D_w is density of water at specific immersion temperature.

The porosity of the coating (φ) can be measured by the ratio of coating density to the theoretical density (D_t), which can be expressed by:

$$\varphi = (1 - \frac{D}{D_t}) \times 100\% \tag{1.2}$$

The porosity of the LZ coating varies with the deposition parameters, such as deposition power, powder feed rate and substrate standoff distance. For the APS deposited coating, the higher the power used in the torch, and the larger the powder feed ratio and the shorter standoff distance used in the deposition process, the denser the coating will be. The commercial APS deposited coating shows a porosity of 15 - 25 %. However, it is important to tailor the porosity of the LZ coating in a range of 8 - 19 % to acquire good thermal and mechanical properties [42].

1.3.3 Sintering Behavior

Sintering in the porous ceramic coating is the process by which the coating will be densified by the reduction in surface energy associated with the excess surface area of the pores and cracks [1]. Sintering of the porous TBCs normally occurs at elevated temperature. When the sintering occurs, the densification process inevitably increases the elastic modulus and thereby decreases the strain compliance of the coating. Meanwhile the thermal conductivity of the coating increases due to the decrease of the porosity [1].

Many experimental approaches can be used to describe the sintering behavior: 1) record the dimension change of the coating sample using a high-temperature dilatometer, 2) detect the porosity distribution change using mercury porosimetry, 3) measure the relative density of the coating during the sintering process, 4) monitor the thermal conductivity increases during a long time heating period at various temperatures [15,43,44]. Vassen et al. investigated the sintering behavior of APS deposited LZ coating at temperatures as high as 1650 °C using the high-temperature dilatometer and the mercury porosimetry [15,43]. The higher porosity the coating had, the higher sintering rate it had. The coating with high porosity level (20 %) densified strongly during the annealing process at 1250 °C [43]. Vassen et al. indicated that decrease porosity might lead to a better thermomechanical behavior [15]. Zhu investigated the sintering behavior by continuously monitoring the thermal conductivity [44]. Zhu found that the LZ coating showed significant thermal conductivity increase (from 0.55 W/m/K to 0.95 W/m/K in 20 hrs.) at 1575 °C, suggesting the coating was undergoing substantial sintering. Nair et al. systematically studied the sintering of the LZ coating [45]. They found that the major mechanism of the sintering process in the temperature range of 8001100 °C is surface diffusion. The sintering above 1100 °C is mainly because of grain boundary diffusion combined with the surface diffusion. The contribution from surface diffusion becomes negligible as the sintering temperature increases.

In general, the sintering resistance of LZ coating is higher than that of YSZ coating, and also $BaZrO_3$ and $SiZrO_3$ coatings [15, 43]. The low-sintering activity of the LZ is beneficial for TBC applications.

1.3.4 Crack and Pore Morphology

The crack and pore morphology of TBC is a crucial parameter affecting the thermal and mechanical properties of the coatings. The cracks can be categorized as the horizontal, vertical, and spherical forms. Zhang et al. studied the crack morphology of the APS deposited LZ coating using a quantitative imaging analysis method [46]. It was found that the cracks were primarily horizontal in the top and middle regions of the cross section area, while vertical cracks became dominant in the bottom region. In addition, the calculated porosities showed a nonuniformity in the cross section area.

Weber et al. indicated that vertical crack is beneficial in TBC application due to enhanced thermomechanical compliance [8, 47]. The LZ-based TBCs were deposited using the spray pyrolysis method, and the vertical cracks were introduced by decomposing the dried coating layer at 575 °C, as shown in Figure 1.6d. Moreover, the multilayer coating with vertical cracks was fabricated by the successive deposition and decomposition of multiple thin layers. The heat conduction is slowed in this multilayer coating due to the generated cracks, and the thermal durability can be increased due to the increased thermo-mechanical compliance [47].

1.4 Mechanical Properties of LZ-based Coating

1.4.1 Elastic Modulus

Elastic moduli include Young' s modulus (E), bulk modulus (K), shear modulus (G) and Poisson' s ratio (ν). These elastic moduli can be measured by a depth-sensing micro- and nanoindentation technique or an ultrasound pulse-echo method [15, 23]. In the micro-indentation technique, E can be obtained from the unloading slope by adopting Sneddon' s flat-ended cylindrical punch model [15]. Shimamura et al. studied the moduli for a series of $Ln_2Zr_2O_7$ material using ultrasound pulse-echo measurement [23]. Shimamura found that the elastic moduli (except for Poisson' s ratio) strongly depend on the atomic radius of rare earth elements for the lanthanide zirconate pyrochlore $Ln_2Zr_2O_7$. The larger atomic radius corresponds to larger E, K, and G values. La has larger atomic radius than Nd, Sm and Gd, so LZ has larger elastic modulus than $Nd_2Zr_2O_7$, $Sm_2Zr_2O_7$ and $Gd_2Zr_2O_7$ [23].

Many researchers successfully measured the elastic moduli of the LZ powder and coating, as summarized in Table 1.1. The sample used in Vassen' s work was prepared by pressing the LZ powders at 1350 – 1400 °C. In this thesis, the Youngs modulus of APS deposited LZ coating with porosity of 7.53 % were measured (detailed discussion in 2.2) [48]. Xu et al. investigated the E of EB-PVD deposited LZ coating [49]. Shimamura et al. measured the LZ powder using the ultrasound pulse-echo method [23]. Girolamo et al. tested the APS deposited LZ coating, which was exposed at 1350 °C for 50 h [33].

The Young' s modulus of the hot pressed LZ sample are about 15 % lower than that of the hot pressed 8YSZ, which is 210 ± 10 GPa. The low Young' s moduli of LZ are advantageous for reducing thermal stresses, which might compensate CTE mismatch in coatings [15].

Table 1.1. Mechanical properties of LZ coating vs. YSZ coating.

Properties	**LZ**	**YSZ**
Young' s modulus	175±11 GPa (densified powder, Vassen [15]) 156±10 GPa (coating, Zhang [48]) 153 GPa (coating, Xu [49]) 280 GPa (powder, Shimamura [23]) 141 GPa (porous coating, Girolamo [33])	210±10 GPa (densified powder, Vassen [15])
Bulk modulus	216 GPa (Shimamura [23])	-
Shear modulus	109 GPa (Shimamura [23])	-
Poisson' s ratio	0.28 (Shimamura [23])	-
Vicker' s hardness	5.51±0.25 GPa (coating, Zhang [48]) 8.83 GPa (coating, Xu [49])	-
Microindentation hardness	9.9±0.4 GPa (densified powder, Vassen [15])	13±1 GPa (Vassen [15])
Nanoindentation hardness	8.8±2.1 GPa (coating, Zhang [48])	-
Fracture toughness	1.1±0.2 MPa·m$^{1/2}$ (densified powder [15]) 1.84 MPa·m$^{1/2}$ (coating, Xu [49]) 0.9 MPa·m$^{1/2}$ (densified powder, Jiang [50])	2.0–3.3 MPa·m$^{1/2}$ (Beshish [51])

1.4.2 Hardness and Fracture Toughness

The hardness test can be classified into three categories according to the length scale applied in the measurement: macroindentation hardness, microindentation hardness and nanoindentation hardness. The measured hardness results of LZ are listed in Table 1.1. The sample used in each researchers work is the same as aforementioned in section 1.4.1. The hardness of LZ varies significantly due to the sample density change. The hardness increases with increasing coating density.

Fracture toughness is a material property which describes the ability of fracture resistance to maintain cracks in the material without elongation of cracks. The definition of fracture toughness is that if a sample has a crack in loading, the stress intensity factor increases with increasing load until the unstable crack propagation occurs at a critical value of K_I [52]. This critical value is fracture toughness (K_{IC}). The standard measurement method of fracture toughness is the four-point bending test of the bulk sample. Another alternative technique is the indentation method, which is widely used to evaluate the fracture toughness of ceramic and coating systems [53]. The fracture toughness can be estimated from the indentation test, and the relationship between fracture toughness and hardness can be expressed by the following equation [52]:

$$K_{IC} = 0.16\sqrt{\frac{E}{H}} \cdot \frac{P}{c^{1.5}} \tag{1.3}$$

where E is the elastic modulus, H is the hardness, P is the applied load, and c is the sum of the crack length and one-half of the indenter imprint diagonal. The fracture toughness of LZ powders and coatings summarized in Table 1.1.

Hot pressed 8YSZ has higher hardness and fracture toughness than LZ (microindentation hardness of densified 8YSZ is 13±1, fracture toughness of densified 8YSZ is 2.0 – 3.3 MPa·$m^{1/2}$) [15, 51]. The low fracture toughness is the major disadvantage of LZ, which leads to a severe limit on its application as a TBC material.

To improve the fracture toughness of LZ material, a composite or multilayer LZ coating can be used. Jiang et al. studied the microstructure and mechanical properties of LZ/$Zr_{0.92}Y_{0.08}O_{1.96}$ composite ceramics, which were prepared by spark plasma sintering at 1450 °C. The results revealed that the composite ceramics had a higher fracture toughness than single phase LZ [50]. Jiang et al. also showed that the fracture toughness of composite LZ and 4YSZ coatings increased with increasing the content of 4YSZ. The fracture toughness reached to a value of 1.8±0.1 MPa·$m^{1/2}$ for

50 % 4YSZ plus 50 % LZ composite coating, which is about two times of that of single phase LZ coating.

In this thesis, we compared single LZ and double-layer LZ/8YSZ coatings [54]. The results showed that the double-layer coating composed of LZ plus porous 8YSZ substantially improved the durability in thermal cycling tests, suggesting the bi-layer design is a feasible solution to improve the fracture toughness in LZ-based coatings.

1.5 Thermal Properties of LZ-Based Coating

1.5.1 Melting Point and Specific Heat Capacity

The high melting point is an important criterion for TBC material, which is good for the thermal stability during the high-temperature operation environment. Thermal analysis is the commonly used method to detect the melting point, which is performed in sealed tungsten crucibles, and the sample temperature is monitored by a spectro-pyrometer. In addition, high-temperature X-ray diffraction experiments (the Advanced Photon Source, Argonne National Laboratory) can also be used to determine the melting temperature by monitoring the pyrochlore (111) peaks [55,56]. As shown in Table 1.2, the experimentally measured melting point of the LZ is about 2523 - 2573 K (2250 - 2300 °C), which is lower than that of YSZ (2953 K, 2680 °C) [15,43,55]. Although the melting point of LZ is lower than that of YSZ, it is still high sufficient for most TBC applications.

Differential scanning calorimetry (DSC) is the most widely used technique to precisely measure the specific heat capacity (C_p). Several researchers investigated the specific heat capacity of LZ in different conditions, as shown in Figure 1.7 [15,21,22, 33]. The samples tested in Vassen' s work were the densified LZ powder using hot pressing technique at the temperature around 1350 – 1400 °C. LZ samples in powder form were used in Bolech and Sedmidubsky' s work. In Girolamo' s work, the specific heat of the LZ coating with a porosity of 11 % was measured. The specific heat of 8YSZ is ~0.55 – 0.65 J/g/K in the temperature range of 300 – 1200 °C, which is larger than that of the LZ [57]. For the TBC materials, small C_p values are preferred to reduce thermal diffusivity.

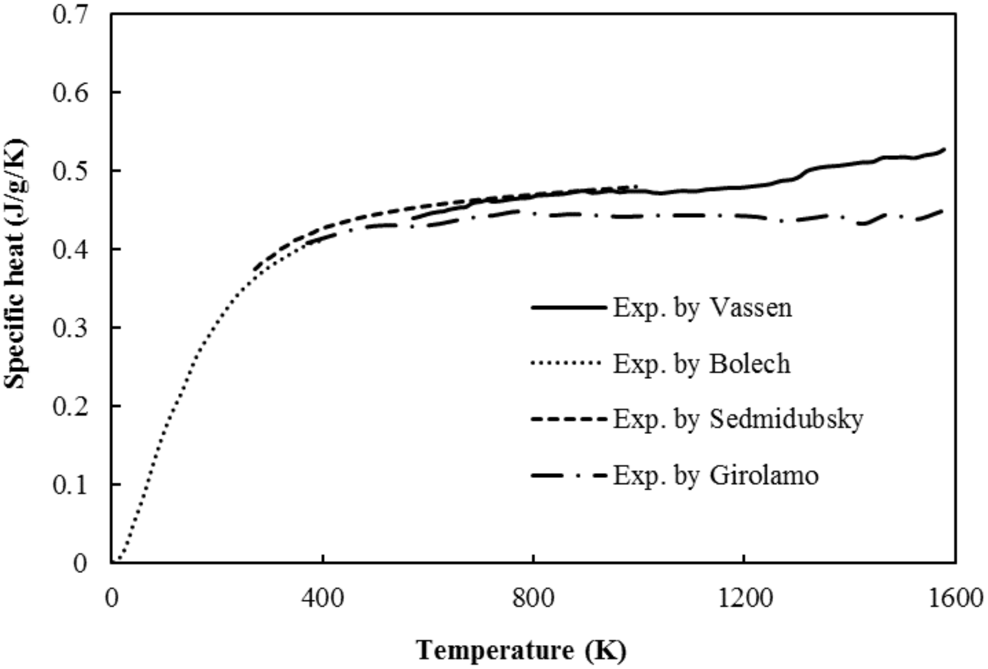

Figure 1.7. Specific heat capacity (C_p) of LZ in the temperature range from 0 – 1600 K. [15,21,22,33].

1.5.2 Thermal Conductivity

For TBC materials, thermal conductivity is the most important material property. Thermal conductivity is a measurement of heat flux in a temperature gradient according to Fourier' s law, which provides the fundamental theory for heat conduction analysis [60].

$$\kappa = \frac{\dot{q}}{dT/dx} \tag{1.4}$$

Table 1.2. Thermal properties of LZ coating vs. YSZ coating.

Properties	**LZ**	**YSZ**
Melting point	2523-2573 K (Vassen [15], Hong [55])	2953 K (Vassen [15])
Specific heat capacity	0.48 J/g/K (1200 K, Vassen [15]) 0.41 J/g/K (400 K, Bolech [21]) 0.42 J/g/K (400 K, Sedmidubsky [22]) 0.44 J/g/K (1200 K, Girolamo [33])	0.65 J/g/K (at 1200 K, Khor [57])
Thermal conductivity	1.55 W/m/K (dense, 1273 K, Vassen [15]) 2.15 W/m/K (dense, 1273 K, Zhu [44]) 0.68 W/m/K (porous, 1173 K, this work [54]) 0.87 W/m/K (EB-PVD, 1273 K, Bobzin [37])	2.25 W/m/K (dense [15]) 0.88 W/m/K (porous [54])
Coefficients of thermal expansion	9.45×10^{-6} /K (273-1473 K, Chen [58]) 9-10×10^{-6} /K (400-1600 K, this work, [54]) 9.0-9.7×10^{-6} /K (400-1600 K, Zhang [59]) 7.6-9.1×10^{-6} /K (400-1400 K, Lehmann [40])	11×10^{-6} /K (dense,1273 K Vassen [15])

Later, Debye used the phonon gasses analogy to explain the heat conduction process and derived an expression for thermal conductivity, which shows that thermal conductivity is related to the phonon mean free path (Λ) [61, 62].

$$\kappa = \frac{c_v \nu_s \Lambda}{3} \tag{1.5}$$

where c_v is the specific heat capacity (about constant volume) and ν_s is the speed of sound. As a result, the thermal conductivity is related to the amount of energy that is carried by a particle, the phonon travel speed, and the distance the phonon travels before scattering [53]. The phonon scattering effect would decrease the thermal conductivity, and the point defect (such as oxygen vacancies) would substantially increase the phonon scattering, so the $Ln_2Zr_2O_7$ pyrochlore structure and doped pyrochlore can have a lower thermal conductivity than that of fluorite structure materials.

The most widely used experimental method to measure thermal conductivity is the laser-flash method, which was first proposed by Parker in 1961 [63]. Thermal conductivity can be determined using thermal diffusivity (D_{th}), specific heat capacity (c_p) and density (ρ), which can be independently measured experimentally. During the experiment process, the front surface of the sample is irradiated by a high-energy laser pulse (usually duration time less than 1ms). The temperature at the back surface of the sample is monitored by an infrared detector [53]. The thermal diffusivity (D_{th}) can be determined by the bottom surface temperature and time curves using Parker' s theory [63]:

$$D_{th} = \frac{1.38L^2}{\pi^2 t_{0.5}} \tag{1.6}$$

where L is the sample thickness, and $t_{0.5}$ is the time required for the bottom surface to reach half of the maximum temperature rise. The measurement error of the standard flash method is less than 5 %. Subsequently, the thermal conductivity (κ) of the LZ coating with given density can be determined according to the following equation [15]:

$$\kappa = D_{th}\rho c_p \tag{1.7}$$

Vassen et al. measured the thermal conductivity of LZ samples using the laser-flash method, in which samples were prepared by hot pressing in the temperature range of 1350 - 1400 °C [15, 40]. The density of the hot pressed sample was greater than 95 %. The thermal conductivity that Vessen measured was ~1.5 – 2.0 W/m/K in the temperature range of 200 – 1400 °C. Zhu et al. did similar studies for the hot pressed disk-shape samples using the spray-dried LZ powders [44, 64]. The measured thermal conductivities of the densified LZ were 2 - 4 W/m/K, which were larger than Vessen' s results, in the temperature range of 200 - 1400 °C. The thermal conductivity is very sensitive to porosity level. A low porosity leads to a high thermal conductivity. The high thermal conductivity in Zhu' s work may be due to the coating' s lower porosity than that in Vassen' s work. In this thesis, the thermal conductivities of

APS deposited LZ coating with a porosity of 11.54 % were measured using the laser-flash method (detailed discussion is in section 2.3) [54]. The measured average thermal conductivity of the porous LZ was ~0.59 - 0.68 W/m/K in the temperature range of 297 – 1172 K (24 - 899 °C). Chen et al. also measured the thermal conductivity of APS deposited LZ coating with a lower porosity [58]. Bobzin et al. investigated the thermal conductivity of mixed 7 wt.% YSZ and LZ layers deposited by the EB-PVD method [37]. All of the experimental data are compiled in Figure 1.8 [15,37,44,54,58].

As shown in Figure 1.8, the thermal conductivities of the LZ coating decrease with the increase of temperature till 1200 K due to lattice scattering, and the conductivities increase again above 1200 K due to radiation contribution. The conductivities also depend on coating porosity. In Vassen and Zhu' s works, the porosities of the LZ samples were very low so the thermal conductivities were much larger than those of the porous coatings in this thesis, Bobzin and Chen' s research [15, 37, 44, 58].

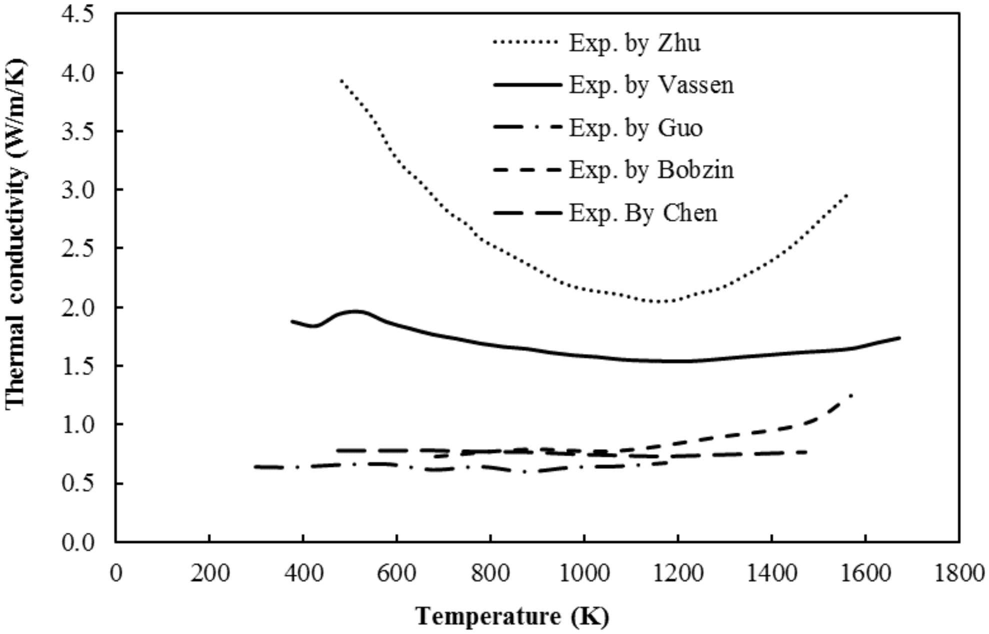

Figure 1.8. Thermal conducitivity of LZ in the temperature range of 273 - 1700 K [15, 37, 44, 54, 58].

In addition to porosity, doped LZ materials were developed to further reduce the thermal conductivity value and improve other thermal and mechanical properties, which enhance the thermal cycling performance. Lanthanide elements are an available option of dopants because they form a similar pyrochlore structure with ZrO_2. Lehmann et al. showed that the thermal conductivities of the Nd, Eu, Gd and Dy doped LZ (30 % of La^{3+} was substituted) were lower than that of pure LZ below 1000 °C [40]. Consequently, Lehmann indicated that the thermal conductivity was affected by the atomic mass and radius of the substituted and substituting atoms. Bansal et al. suggested that Gd and Yb can replace the La^{3+} cation to form new pyrochlore structure materials such as $La_{1.7}Yb_{0.3}Zr_2O_7$, $La_{1.7}Gd_{0.3}Zr_2O_7$ and $La_{1.7}Gd_{0.15}Yb_{0.15}Zr_2O_7$ [64]. The Gd and Yb doped LZ showed a lower thermal conductivity, a better high-temperature stability up to 1650 °C (3000 °F) and a better sintering resistance than LZ. In addition, Yb, Ce, Y, In and Sc were reported as dopants for both La^{3+} and Zr^{4+} site [53, 65]. Xiang et al. indicated that $(La_{0.7}Yb_{0.3})_2(Zr_{0.7}Ce_{0.3})_2O_7$ and $(La_{0.2}Yb_{0.8})_2(Zr_{0.7}Ce_{0.3})_2O_7$ had lower thermal conductivities than LZ [65]. Wang found that $(La_{1-x1}Y_{x1})_2(Zr_{1-x2}Y_{x2})_2O_7$, $(La_{1-x1}In_{x2})_2(Zr_{1-x2}In_{x2})_2O_7$ and $(La_{1-x1}Sc_{x1})_2(Zr_{1-x2}Sc_{x2})_2O_7$ had the potential to acquire lower thermal conductivity than LZ [53].

The low thermal conductivity is the prime advantage of the LZ coating over the YSZ coating. Vassen et al. compared the thermal conductivity of hot pressed YSZ and LZ samples [15]. Vassen indicated that high dense LZ samples' thermal conductivities were 30 – 35 % lower than YSZ at 800 – 1000 °C, in the similar porosity level. Bobzin et al.' s work showed that the thermal conductivity of EB-PVD deposited 7YSZ was about 25 – 40 % larger than the EB-PVD deposited LZ coating [37]. However, the thermal conductivity of APS deposited LZ coating was not investigated. In chapter 2 and 4, the thermal conductivity of APS deposited LZ-based TBC coating will be systematically studied using experimental and modeling methods.

1.5.3 Coefficient of Thermal Expansion

TBC is a multiple layer coating system including alloy, intermetallic bond coat, TGO layer and ceramic top coat, therefore the volume change in the thermal cycling process is different due to the different CTEs in each layer. Thermally induced residual stress generated among TBC layers due to CTE mismatch becomes a primary cause of failure [5]. Since the CTE values of superalloy substrate and bond coat are usually about 15×10^{-6} and 14×10^{-6} /K, respectively, at 1000 °C [5, 9], which are much larger than the typical ceramic top coat. As a result, large CTEs are preferred for the ceramic top coat to reduce CTE mismatch. Additionally, due to large thickness of substrate, its CTE influence may be more important than bond coat.

The most widely used approach to measure CTEs is the dilatometry method. The linear CTE value can be obtained from the measurements of the temperature-dependent length change of the measured sample using a high-temperature dilatometer. The bar-shaped sample is used in the measurement. The specimen is heated at a constant heating rate (normally 5 °C/min) and the temperature and length value are continuously monitored. The linear CTE can be calculated by [66]:

$$\alpha_l = \frac{1}{L} \cdot \frac{dL}{dT} \tag{1.8}$$

where L is the original length at initial testing temperature, dL represents the unit length change between each scan step, and dT is the unit temperature change between each scan step.

Many researchers measured the CTE of LZ using the dilatometer, as summarized in Figure 1.9 and Table 1.2 [40, 54, 58, 59]. Chen et al. investigated the CTE of both bulk LZ material and APS deposited LZ coating using the dilatometer, and the results showed a similar trend [58]. The apparent CTE value of the LZ coating was about 9.45×10^{-6} °C^{-1} in the temperature range of 0 – 1200 °C. In this thesis, dilatometry method was used to measure the CTE of LZ. The average porosity of the APS deposited LZ coating in this measurement was 11.54 % (detailed discussion is in section 2.3) [54]. Zhang et al. determined the CTE value of LZ powders by the variation of lattice parameters during the heating process [59]. The lattice parameters came from the XRD analysis at different temperatures. Lehmann, using a dilatometer, investigated the CTE of hot pressed LZ samples with density between 69 % and 93 % of the theoretical value [40].

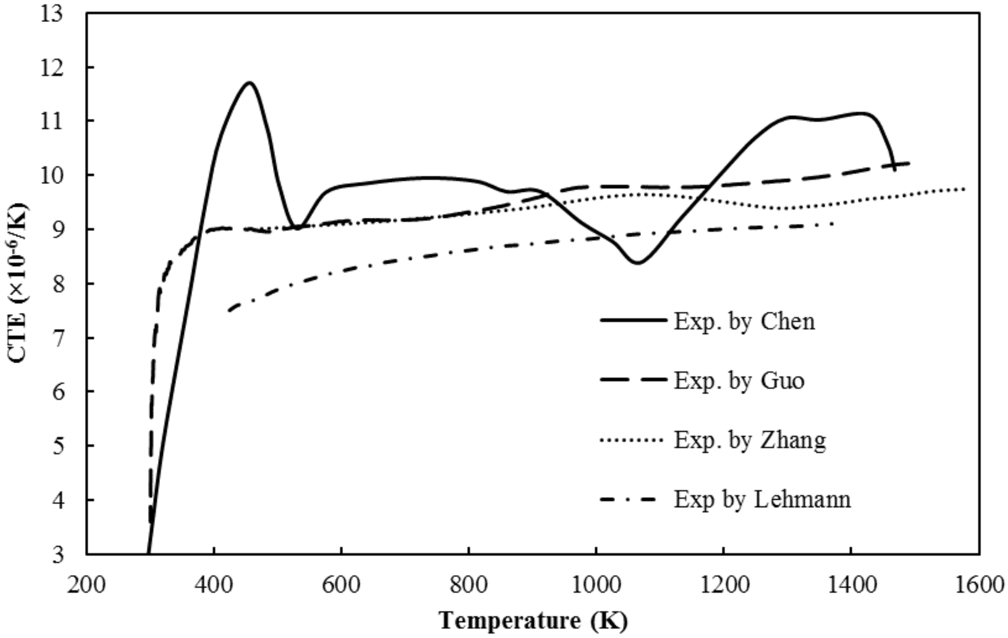

Figure 1.9. CTEs of LZ in the temperature range of 273 - 1600 K. [40, 54, 58, 59].

The CTE of pure LZ is lower than that of YSZ (11×10^{-6} /K at 1000 °C) [15]. As a result, the CTE difference between the LZ top coat and the bond coat in LZ-based TBC system is larger than that between the YSZ top coat and the bond coat in YSZ TBCs. This is a disadvantage for LZ in TBC application because this may lead to a large volume change during the thermal cycling process, which generates higher thermal and residual stress. However, CTE value of the LZ-based coating can be increased by doping with some rare earth element dopants. For example, Xiang et al. indicated that the CTE of $(La_{0.7}Yb_{0.3})_2(Zr_{0.7}Ce_{0.3})_2O_7$ and $(La_{0.2}Yb_{0.8})_2(Zr_{0.7}Ce_{0.3})_2O_7$ were higher in the high-temperature range (above 400 °C) than that of pure LZ [65].

Meanwhile, Cao and Zhang suggested that using Ce (5 - 20 %) to dope into LZ to increase the CTE value [59, 67].

1.6 Thermomechanical Durability of LZ-Based Coating

1.6.1 Thermal Cycling Test

Thermal cycling tests are applied to simulate the operation environment of TBCs in gas turbines. Thermal cycling tests can be sorted into two broad categories based on temperature gradient during thermal process [68]. (1) A constant temperature distribution in the sample without a gradient in TBC samples. When heating/cooling rates are low, such as the furnace cycling test (FCT), the sample is slowly heated in a furnace, which creates a high-temperature isothermal environment for the entire TBC system, and then it is cooled by the compressed gas or ambient air cooling out of the furnace [69]. (2) The thermal cycling tests with a temperature gradient across the sample due to fast heating/cooling, such as the jet engine thermal shock (JETS) test, laser rig and flame rig [68]. In the JETS test, a typical cycle consists of a 20 s heating process, a 20 s forced nitrogen gas cooling and a 40 s dwell cooling in ambient air environment. The front surface temperature can reach 1400 °C. The failure criterion in the JETS tests is more than 20 % spallation of the TBC sample. Since the back side of the sample is not heated, a thermal gradient is generated in the TBC samples during the JETS test. The temperature gradient in the JETS over the whole sample depends on the thickness of the coating system, coating composition, porosity, and microstructure of the coating [69].

Although the maximum temperature and the heating and cooling duration time vary in different thermal cycling tests, large thermal stress and strain mismatch generated due to the CTE mismatch between the top and bond coats are the principal reason for the failure of LZ coatings. To obtain a long thermal cycling lifetime, the LZ coating needs to accommodate the thermal strain associated with thermal cycling [1].

In addition, oxidation of bond coat and low K_{IC} of LZ are additional factors for the spallation of the LZ coating [54, 70].

Many researchers have conducted thermal cycling tests of LZ in different testing conditions. Because the TBC is a complicated system, the thermal cycling results vary due to different cycling test parameters, coating porosities, coating microstructures, multilayer coating architectures, and coating compositions, etc. Vassen et al. conducted thermal cycling test with a large temperature gradient across the sample [15, 43, 71]. The APS deposited LZ coating with single-layer coatings and the APS double-layer coatings with YSZ plus LZ top coat were used in these tests. These TBC systems were tested in the surface temperature range of 1200 - 1450 °C. The heating and cooling time periods were 5 min and 2 min. The results indicated that the single-layer coating had a rather poor thermal cycling performance. The double-layer system showed a similar to or slightly better performance than that of YSZ coatings at temperatures below 1300 °C, suggesting the double-layer coating with YSZ is an effective way to improve the lifetime of TBC in thermal cycling tests [71]. Meanwhile, Cao et al. also showed that the single-layer LZ coating had a short thermal cycling lifetime, but the double-layer LZ coating with La_2O_3-ZrO_2-CeO_2 composite sublayer can greatly improve the lifetime [72]. However, the more layers that the TBC coating has, the more artificial defects might be generated during the deposition process. To reduce artificial defects, the composition, thickness and porosity in the double-layer coatings need to be properly tailored.

Bobzin et al. investigated the thermal cycling performance of EB-PVD deposited LZ and 7YSZ coatings using the FCT test [70]. The samples were heated to 1050 °C for about 30 min, then cooled to 35 °C in compressed air for 5 min. Delamination of the LZ coating occurred at 1856 cycles, which showed a better performance than 7YSZ coating (1380 cycles). The alumina scale was observed in Bobzin' s thermal cycle experiments, which was evidence of bond coat oxidation. Bobzin suggested that the main reason of the failure was a combined effect of oxidation of the bond coat and CTE mismatch. In this thesis, we conducted JETS test for single-layer LZ coating and double-layer coating composed of LZ and 8YSZ deposited by APS with different porosities [54]. The front surfaces of the TBC samples were heated to 1232 °C for 20 s, cooled by compressed N_2 gas for 20 s and followed by ambient cooling for 40 s. The front and back side temperatures were monitored during the test by pyrometers to analyze the cross-sectional temperature gradient. The initial spallation time of the TBC can be pinpointed by the temperature difference between the front and back side surfaces. Our results showed that the single-layer porous 8YSZ coating had better JETS performance than the single-layer porous LZ coating. Additionally, the thermal durability of LZ-based coating can be improved by introducing a porous 8YSZ buffer layer between the top and bond coat [54].

1.6.2 Erosion Test

Erosion is regarded as a secondary cause of failure of TBCs by deteriorating the coating through progressive removal of the coating material due to the mechanical interaction between the coating surface and the impinging solid particles [73]. The erosion tests by solid particle impingement were standardized by ASTM G76-13 [74]. Typically, the Al_2O_3 medium with the particle size of 50 μm is used as the abrasive particles, and the abrasive particles are accelerated by the high-velocity carrier gas through a particle-gas supply system. Finally, the abrasive particles are impacted on the surface of the coating at a specific impinging angle. The average erosion rate (mg/g or g/kg) is used to evaluate the erosion resistance performance, which is determined by the slope of TBC mass loss (mg) versus the mass (g) of erodent. Many variables like velocity, working distance, impact angle, abrasive particles properties, coating hardness and mechanical properties of coating (H and K_{IC}) affect the erosion results.

Ramachandran et al. studied the erosion of APS deposited YSZ and LZ coatings with different coating porosity, abrasive particles' velocity, and impact angle [75]. They found that the porosity level is the most predominant factor affecting the erosion rate of the coatings. High porosity in the coating increased erosion rate. The erosion rate increased with the increasing of the abrasive particles' velocity.

One method of improving erosion test performance is microstructure modification. For instance, the columnar microstructure of EB-PVD deposited coating typically provides the improvement of erosive resistance compared to the "splat" grain microstructure of APS deposited coating [73]. In addition, the aging of the APS coating decreases the erosion rate and therefore enhances the erosion performance. However, the aging of the EB-PVD coating results in a significant increase of erosion rate due to the sintering of columns [73].

1.7 Simulation Methodology

1.7.1 Density Functional Theory

Material is a collection of bonded atoms, and chemical reactions can be expressed by interactions between electrons, which can be described by the Schr$\ddot{o}$dinger equation. As a result, almost all the material properties, including the chemical, mechanical, electrical, magnetic, optical, thermal, etc., can be predicted from the atomic number and mass of the atomic species by solving the Schr$\ddot{o}$dinger equation. First principles calculation is actually a series methods to solve the Schr$\ddot{o}$dinger equation.

Density function theory (DFT) was proposed as an alternate approach to solve the Schr$\ddot{o}$dinger equation. The DFT interprets the theory of electronic structure by electron density distribution n(r) rather than the many-electron wave function [76]. The Kohn-Sham equation is applied in DFT to describe the density distribution, shown in Equation (1.9) [77–80].

$$[-\frac{h^2}{2m}\nabla^2 + V(r) + V_H(r) + V_{xC}(r)] \cdot \Psi_{nk}(r) = \varepsilon_{nk}\Psi_{nk}(r) \tag{1.9}$$

where m is electron mass, h is Planck's constant, Ψ_{nk}(r) is electron wave function, r is the coordinate of electron, V(r) is a potential energy that defines the interaction between an electron and the correlated atomic nuclei, V$_H$(r) is Hartree potential which defines the Coulomb repulsion between electrons, V_{XC}(r) is functional derivative of the exchange-correlation potential. V_H and V_{XC} can be expressed as the following equations.

$$V_H(r) = e^2 \int \frac{n(r')}{|r - r'|} d^3r' \tag{1.10}$$

$$V_{XC}(r) = \frac{\delta E_{XC}(r)}{\delta n(r)} \tag{1.11}$$

$$n(r) = \sum_{nk}^{\#\ of\ e} |\Psi_{nk}(r)|^2 \tag{1.12}$$

where n(r) is electron density.

Kohn-Sham equation is typically used for self-consistent-field electronic structure calculations of the ground-state properties of atoms, molecules, and solids. In this equation, only the exchange-correlation potential as a function of electron densities need to be approximated. The most successful approaches to describe the electron density are (1) local density approximation (LDA), and (2) Generalized gradient approximation (GGA). The LDA approach uses a slow varied and localized spin density to make the approximation. The exchange-correlation energy can be expressed as the following equation using the LDA approach [81].

$$E_{XC}^{LDA}(n\uparrow, n\downarrow) = \int d^3rn\varepsilon_{XC}^{unif}(n\uparrow, n\downarrow) \tag{1.13}$$

On the other hand, the exchange-correlation energy can be expressed as the following equation using the GGA approach [82, 83].

$$E_{XC}^{GGA}(n\uparrow, n\downarrow) = \int d^3rf(n\uparrow, n\downarrow, \nabla n\uparrow, \nabla n\downarrow) \tag{1.14}$$

To obtain the system energy of the atomic model, the Kohn-Sham equation is treated using the iterative algorithm: (1) assign a reasonable initial electron density n_0(r), (2) solve Kohn-Sham equations to find the single particle wave function Ψ(r), (3) calculate the election density from single particle wave function using n_{ks}(r)=2$\sum_i \Psi_i^*(r)\Psi_i(r)$, (4) compare the calculated electron density with the one used in previous step, if the difference between the two is smaller than the error tolerance, then can be regarded as the ground state electron density [80]. The ground state energy of the system can be computed by substituting the ground electron density into the Kohn-Sham equation. Since this iterative process requires enormous computational effort, supercomputer and numerical method codes become imperative tools to solve these problems. In this thesis, most of the DFT calculations are performed by Vienna Ab initio Simulation Package (VASP) and Cambridge Serial Total Energy Package (CASTEP) [84–88]. The VASP uses the plane-wave pseudopotential to specify the interaction between ions and electrons, the projector-augmented wave (PAW) and ultrasoft pseudopotential are the most widely used pseudopotentials [89, 90]. In CASTEP, CA-PZ (Ceperley, Alder, Perdew and Zunger) functional is used in this work as an LDA functional [91, 92]. For both the VASP and the CASTEP, the most common functionals of GGA approach are PBE (Perdew, Burke, Ernzerhof) and PW91 (Perdew et al) [81, 83]. The election density and the total system energy computed by DFT method are in the ground energy state, which is the lowest energy state of the electron and at 0 K in most cases. To calculated the properties in higher temperature, large scale model and further simplifications need to be introduced.

1.7.2 Molecular Dynamics Method

In molecular dynamics (MD) method, the successive structured system is generated by an ensemble of particles, whose trajectories follow Newton's law of motion [93]. The trajectories specifies the positions and velocities of the particles in the system as a function of time, which can be obtained by solving the differential equation based on Newton's second law (F=ma):

$$\frac{d^2x_i}{dt^2} = \frac{F_{x_i}}{m_i} \tag{1.15}$$

where m_i is the atomic mass, x_i is the coordinate of the atom, and F_{xi} is the force on the atom. To describe the interatomic interactions in the actual system, the forces on each atom are changed whenever the position of atoms changes. As a result, the continuous force field is used to realize this regime [93].

The MD particle trajectories are generated using the finite difference techniques with continuous force field models. This algorithm assumes that the position, velocity, accelerations can be approximated using Taylor series expansion:

$$r(t+\delta t) = r(t) + \delta t v(t) + \frac{1}{2}\delta t^2 a(t) + \frac{1}{6}\delta t^3 b(t) + ... \tag{1.16}$$

$$v(t+\delta t) = v(t) + \delta t a(t) + \frac{1}{2}\delta t^2 b(t) + ... \tag{1.17}$$

$$a(t+\delta t) = a(t) + \delta t b(t) + ... \tag{1.18}$$

where t is the time, δt is the finite time step between two consecutive positions, r is the position, v is the velocity (the first derivative of position with respect to time), a is the acceleration (the second derivative of position), b is the third derivative, and so on [93]. To describe the actual atomic motion, δt should be at least one order of magnitude smaller that the fastest motion in the atomic system. Since the vibrational frequencies and optical phonon frequencies are in the time period of ~10 fs and ~100 fs in a typical molecular system respectively, the typical time step used in the MD calculations is in an order of fs [94]. Among all the time integration algorithms, the Verlet algorithm is the most widely used method for integrating the motion equations in the MD calculations [95]. In Verlet algorithm, the new position at t+δt is calculated from the position and acceleration at t and the position at t-δt, which can be derived following equations:

$$r(t+\delta t) = r(t) + \delta t v(t) + \frac{1}{2}\delta t^2 a(t) + ... \tag{1.19}$$

$$r(t-\delta t) = r(t) - \delta t v(t) + \frac{1}{2}\delta t^2 a(t) - ... \tag{1.20}$$

Add Equation (1.19) and Equation (1.20) gives the position equation at t+δt [93].

$$r(t+\delta t) = 2r(t) - r(t-\delta t) + \delta t^2 a(t) \tag{1.21}$$

In addition to Verlet algorithm, several variations are developed such as the leap-frog algorithm and velocity Verlet algorithm [96, 97].

In the MD calculation, the atom is described as a rigid body, without considering electrons explicitly. With this simplification, the complicated quantum parameters leave only the particle wavelength, which is comparable with the interatomic distance. Therefore, the atomic dynamics can be predicted using the semi-empirical potentials, which specifies the force field with the atomic configuration [98]. The potentials for a specific systems are developed by fitting the potential functions to the experimental data or the DFT-calculated data, such as equilibrium lattice parameters, adhesion energy, defects formation energy, surface energy, elastic modulus, etc. The most widely used potentials include pairwise potentials (Lennard-Jones, Buckingham, Morse, etc.), charged pairwise potentials (Coulombic, point-dipole), many body potentials (embedded atom method (EAM), charge-optimized many body potential (COMB), Tersoff , etc.), reactive-force-field potential (ReaxFF) [98–100].

The necessary steps to perform an MD simulation in a microcanonical ensemble include: (1) establish an initial model with reasonable atomic construction, and the initial velocities may be assigned to the system, (2) find a suitable potential for the system, hence the force on each atom can be calculated by differentiating the potential function, (3) set the boundary condition and equilibrate the system by energy minimization, (4) perform the simulation in a suitable constant ensemble (NVE, NVT, NPT etc.) [93].

1.8 Research Objectives

The primary goal of this work is to design a novel robust LZ based on TBC system suitable for application beyond 1200 °C. There is no systematic characterization of the physical, thermal and mechanical properties of LZ TBC coatings in previous work. Most of the existing researches about thermal and mechanical properties of LZ were characterized using the fully dense hot pressed powders or the EB-PVD deposited coatings, whose properties are extremely different with the APS deposited coating. In this thesis, the physical, thermal and mechanical properties of APS deposited LZ coatings are systematically investigated, and thermomechanical durability of APS deposited LZ coating are also studied. To improve the durability of the APS deposited

LZ-based coating, two schemes are performed to design and fabricate the TBC coating: (1) multiple layered coating, and (2) LZ/8YSZ composite coating. Different architecture and composition ratio are used to construct the LZ-based coatings.

On the other hand, the thermal and mechanical properties of the pure LZ can hardly be measured using experiments way due to the porous characteristic of the LZ powders. However, theoretical modeling method can be an alternative way to obtain the properties of single crystal pure LZ materials. Since there is a lack of comprehensive theoretical understanding of the LZ material, so in this thesis some basic thermal and mechanical properties are investigated using DFT, MD, and finite element method modeling.

In addition, from the thermomechanical durability analysis, most of the thermal cycling failures occur at the interface between the top coat and the bond coat. The stress-strain behaviors at the interface are responsible for the failure of the TBC in thermal cycling test. To better understand the thermal cycling failure mechanism, the mechanical properties of the interface between top and bond coat are investigated using the DFT calculations. Since the main composition of the YSZ is ZrO_2 (8YSZ contains about 92 wt% ZrO_2), and the LZ is also synthesized from ZrO_2 (66.6 wt%) and La_2O_3, the interface tensile and shear simulations are performed using ZrO_2/Ni interface models with different Ni thickness.

1.9 Thesis Outline

In this chapter, the background of TBC research, literature review, and the research objective of LZ-based TBC are presented.

Chapter 2 will describe the experimental research of APS deposited LZ-based TBC. After characterizing the basic physical properties of the LZ powder, several layered architectures of the LZ and 8YSZ TBCs are designed and deposited using APS technique. Mechanical, thermal properties and thermomechanical durability of the layered LZ-based TBC are studied. To further improve the thermal durability of

LZ-based TBC, the LZ/8YSZ composite TBC are proposed and the corresponding thermal durability experiments are performed. The delamination mechanism of the LZ-based TBC is analyzed, and the fracture toughness and the stress status at the interface and in the LZ layer are the primary reason of the failure.

Chapter 3 will discuss the DFT and MD modeling work on mechanical properties of single crystal LZ. The single crystal LZ unit cell is optimized by energy minimization. Nanoscale tensile and shear simulations are performed on the single crystal LZ using DFT and MD calculations, respectively. Young's modulus of the single crystal LZ is calculated using two approaches: the stress-strain curve analysis in large deformation and the elastic constant approximation in small deformation. The LZ has anisotropic elastic properties, and the charge transfer analyses are performed to explain this phenomenon.

Chapter 4 will elaborate the simulation work about the thermal properties of the single crystal LZ and the LZ coating. Based on the optimized single crystal LZ in Chapter 3, the specific heat of the LZ is calculated using DFT method. The thermal conductivity of the single crystal LZ is calculated using a reverse non-equilibrium molecular dynamics (RNEMD) method, which based on Muller-Plathe algorithm. The thermal conductivity of porous LZ coating can be calculated by plugging the MD results into the image-based finite element model.

Chapter 5 will focus on the stress status at the interface between the top coat and bond coat. The tensile and shear stress-strain simulation are performed on the ZrO_2 and Ni interface DFT models, and corresponding elastic modulus, ultimate strength, and toughness are calculated. Charge density and Bader charge analyses are analyzed to explain the mechanical properties trend.

Chapter 6 will summarize the entire dissertation and suggest the future study about LZ-based TBC.

CHAPTER 2. EXPERIMENTAL STUDY OF LZ COATINGS

2.1 Powder Fabrication and Characterization

2.1.1 Powder Fabrication Process

The criteria of the fabrication of LZ feedstock powders are (1) spherical shaped powder, (2) uniform and fine particle size, (3) homogeneous composition, (4) high purity, and (5) low fabrication cost. The requirement of the shape and size distribution in powder is because the powder flow capability is very important for the feedstock in a thermal spray process. The spherical shaped powder and its uniform particle size are critical for the smooth flow of powders through the feedstock-feeding pipe of the thermal spray facility. Homogeneous composition and higher purity can enhance the phase stability and corrosion resistance, which is available to improve the coating lifetime.

In general, three preparation methods are used in the laboratory: (1) a solid state reaction [49, 101], (2) a nitric acid dissolution method [102] and (3) a sol-gel technique [91, 103, 104]. Comparing these methods, the solid state reaction method is good for large scale fabrication in industry. Because one objective of this research is to develop a TBC material that is applicable to the massive manufacture, all of the LZ powders used in this thesis were fabricated using solid state. The raw materials for the LZ fabrication include La_2O_3 and ZrO_2. The raw materials were milled into small particles as the first step. Then La_2O_3 and ZrO_2 powders were mixed together using a V-shaped powder blender. After that, water and binder material were pumped in to the mixed raw materials, and all the materials were made into a slurry cake. After that, the slurry cake was dried in 150 °C for several hours. Finally, the mixed raw materials were filled into an alumina case and sintered in the furnace at 1650 °C. The LZ material was synthesized during the high-temperature calcination process.

To satisfy the size requirement of the thermal spray equipment, the powder needs to be filtered several times using screeners with a specific mesh size and atomized using a high-pressure atomization device.

2.1.2 LZ Powder Characterizations

The size of LZ powder was limited to a particular dimension range because uniform particle size can provide a good flow capability in the feedstock system for an APS torch. The LZ Powder size was measured by a Microtrac standard range particle analyzer (Microtrac, s3500, Pennsylvania, USA). The particle analyzer statistically analyzed the particle size using three precisely placed red laser diodes to accurately characterize particles. The column in Figure 2.1 shows the distribution percentage of the LZ particle size, and the curve in Figure 2.1 depicts the accumulative distribution percentage. The distribution percentage of particles shows that the average powder size of LZ powder was about 65 μm, which satisfied the powder size requirement of the APS equipment.

The chemical composition of the LZ powders was investigated by weight percentage using inductively coupled plasma techniques (ICP) and inductively coupled plasma mass spectrometry (ICP-MS) methods in NSL Analytical test laboratory. Table 2.1 shows the tested chemical composition of LZ. The measured chemical composition ratio of LZ powders is very close to the theoretical weight ratio of ZrO_2 and La_2O_3 in LZ (43% : 57%), suggesting this solid state reaction approach is able to fabricate the LZ coating in a good quality.

X-ray diffraction (XRD) testing of LZ powder was performed using laboratory XRD equipment with a wavelength of 1.54 Å. The XRD scan speed is 4 degrees per minute and the scan increment is 0.02 degrees per step. As shown in Figure 2.2, the XRD pattern of the LZ powder synthesized by solid state reaction (red curve) matched very well to the standard XRD pattern card of LZ (pdf card #73-0444, green lines). In addition, it can be concluded from the XRD pattern that LZ is a

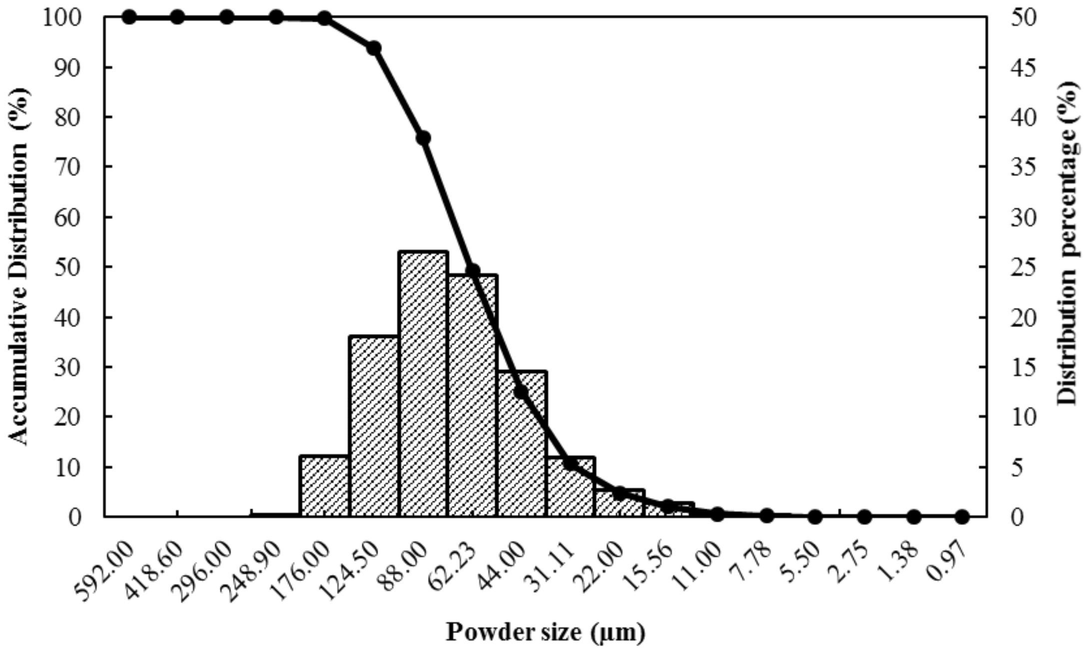

Figure 2.1. Powder size analysis results.

Table 2.1. Chemical composition of LZ powders.

Chemistry	**Test method**	**Weight percentage**
Lanthanum Oxide	ICP	57.0
Zirconium Oxide	ICP	41.6
Aluminum Oxide	ICP	< 0.1
Silicon Dioxide	ICP	0.7
Ferric Oxide	ICP-MS	0.1
Hafnium Oxide	ICP	0.1
Other Oxides Total	ICP-MS	~0.4

cubic phase with space group Fd3$\bar{m}$. The powder shows slim peak widths, indicating relatively big crystalline sizes or higher crystalline disorder in the LZ powders.

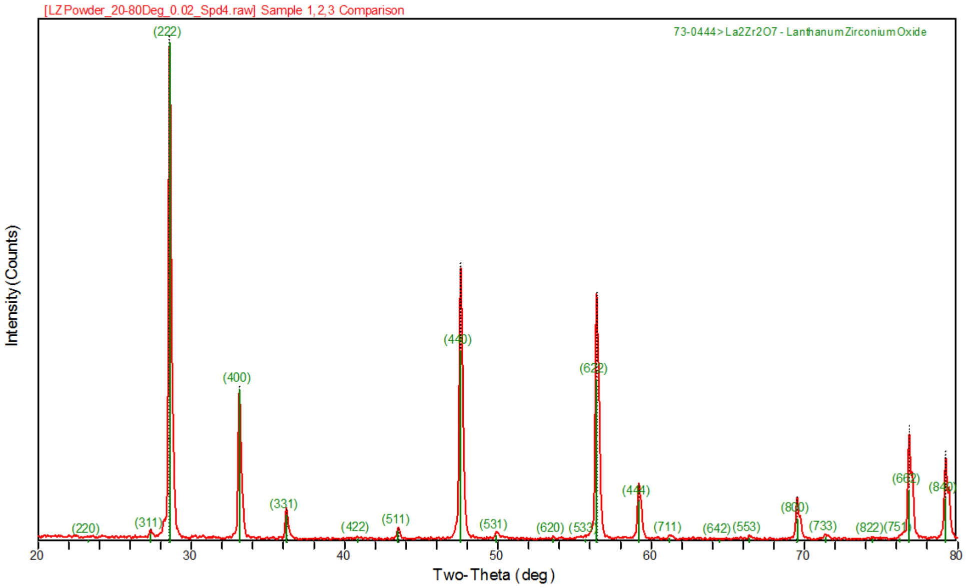

Figure 2.2. X-ray diffraction data of LZ powders.

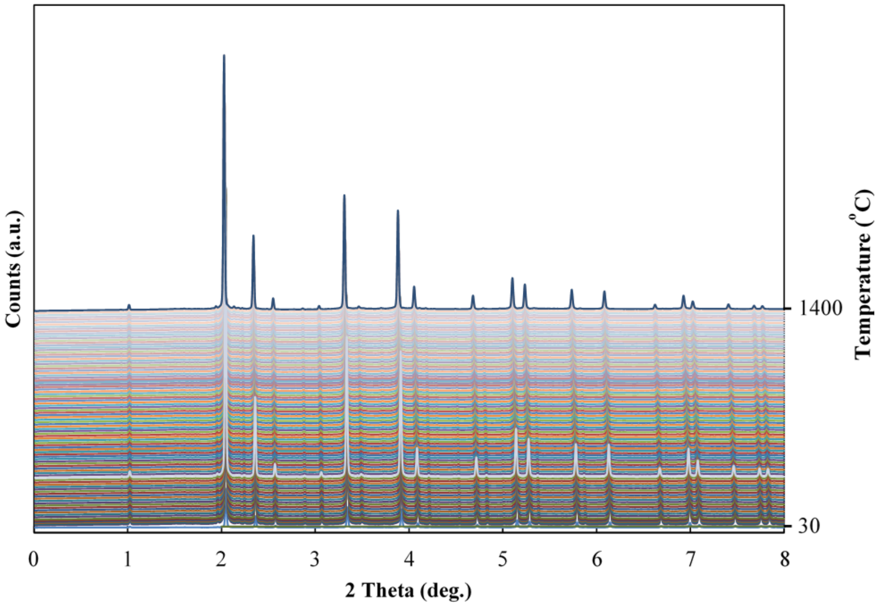

Figure 2.3. High energy XRD as a function of temperature.

In addition, phase stability of the LZ from room temperature to 1673K (1400 °C) has been studied using synchrotron X-ray diffraction (XRD) at Argonne National

Laboratory, as shown in Figure 2.3 [46, 48, 105]. The synchrotron XRD curves of LZ powder show very similar patterns from 30 °C to 1400 °C, indicating that there was no phase change during this continuous heating and cooling process.

The scanning electron microscope (SEM) images of LZ powders, which can be directly used as the feedstock powders in the thermal spray equipment, are shown in Figure 2.4. The powder images show spherical or ellipse shapes with uniform particle size. Even in a single powder, the LZ powder is still porous with a lot of holes and pores in the powder particle.

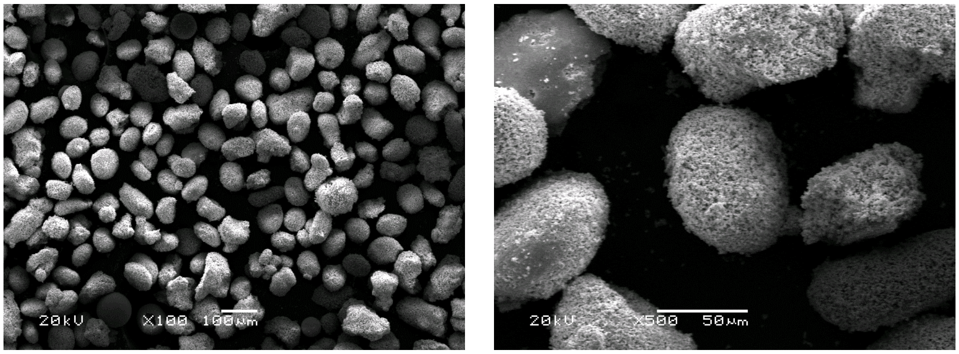

(a) X100 (b) X500

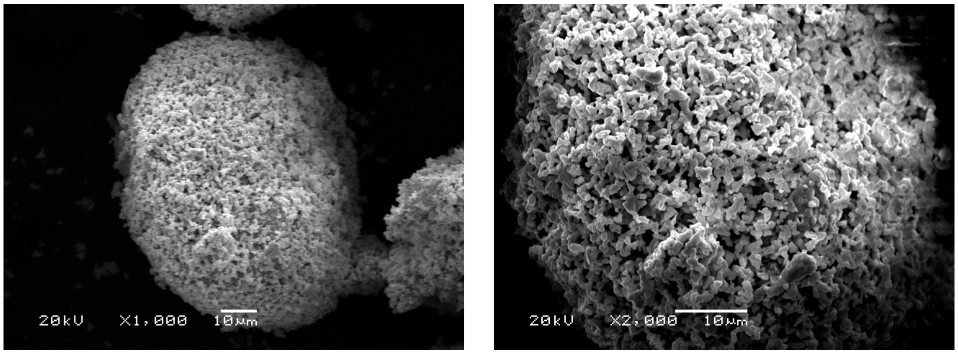

(c) X1000 (d) X2000

Figure 2.4. SEM images of LZ powders under different magnification.

To further detect the LZ crystal morphology, the transmission electron microscopy (TEM) image of milled LZ coating powders is shown in Figure 2.5, which exhibits the polycrystalline morphology in nanoscale.

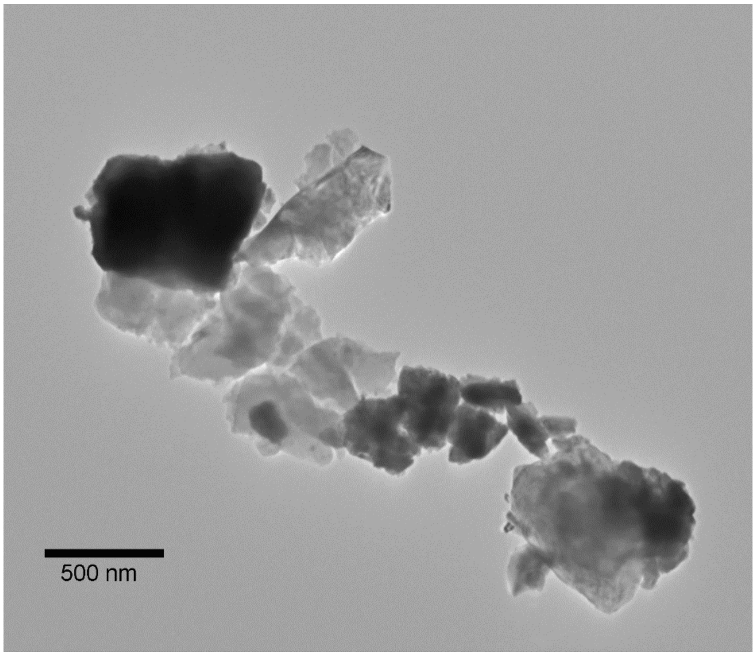

Figure 2.5. TEM image of LZ coating powder.

2.2 Mechanical Properties and Stability of Layered LZ Coating

2.2.1 Single (SCL) and Double Ceramic Layer (DCL) LZ Coating Preparation

All LZ coatings were deposited using the the air plasma spray (APS) technique using a Praxair patented plasma spray torch. Haynes 188 superalloy (Haynes International, Kokomo, IN, USA) was used as the standard substrate material. NiCrAlY powder, Ni-211 (Praxair Surface Technologies, Indianapolis, IN, with a chemistry Ni 61.5 wt%, Cr 21.12 wt%, Al 9.94wt%, Y 1.02wt% [9]) was selected as the standard bond coat feedstock in this work. The bond coat thickness was in the range of 180–230 μm. Ceramic LZ or 8YSZ top coats were deposited above the bond coat using the APS technique. The thicknesses of the top coats used in this thesis range from 300 to 600 μm. In order to deposit the top coat with designated porosity, all of the APS parameters were properly tailored. Dense and porous 8YSZ TBC systems were also deposited as a reference sample on the same bond coat and substrate using the same deposition technique and similar deposition parameters. AMPERIT 825.001

and AMPERIT 827.006 powders (HC Starck, Munich, Germany) were selected to produce the dense and porous 8YSZ.

Four kinds of shapes were applied as substrate. 10 mm cubic bulk substrates were used to produce the free-standing samples, which were deposited directly on smooth substrates without any bond coats, so that the top coats can be easily peeled off from the cubic substrates. Round button HS 188 substrates with a diameter of 1 inch (25.4 mm) were used in the bond strength tensile tests. Tensile bar samples (200×20 mm) were used in thermal gradient mechanical fatigue (TGMF) tests. Rectangular panel (50.8×25.4 mm) samples were used in erosion tests.

Single ceramic layer (SCL) LZ coating samples deposited in the first batch were aimed to investigate the physical, mechanical and thermal properties of the LZ coating. The SCL samples were coated using the same powder feed ratio, deposition speed, and plasma current for single layer coating. The only differences among sample 1 to sample 5 are the standoff distances, which are the distances from the spray torch to the sample surface. The deposition standoff and physical parameters of SCL LZ coatings in the first batch are listed in Table 2.2.

Table 2.2. Physical properties of SCL LZ coatings deposited in the 1^{st} batch.

Sample number	**Standoff distance (mm)**	**Density (g/cm^3)**	**Top coat thickness (μm)**	**Porosity** (%)
1	165.1	5.2587	445	11.36
2	177.8	5.2584	422	12.36
3	190.5	5.2917	389	11.81
4	203.2	5.2614	373	12.31
5	215.9	5.0089	325	16.52

Double layer TBCs deposited in the second batch include both 8YSZ and LZ layers. Both coating layers were sprayed using the APS method in the second batch.

Two different types of double-layer TBC samples were deposited: LZ coating on a porous 8YSZ layer and LZ coating on a dense 8YSZ layer. Additionally, two types of single-layer TBC samples, single-layer LZ and single-layer porous 8YSZ, were produced for comparison purposes. All prepared TBC samples are listed in Table 2.3.

Table 2.3. List of SCL and DCL LZ/8YSZ layered TBCs deposited in the 2^{nd} batch.

Sample number	**Bond coat**	**Top coats**	**Top coat thickness (μm)**	**Porosity (%)**
6	NiCrAlY	SCL LZ	424	11.54
7	NiCrAlY	DCL Porous 8YSZ + LZ	138 + 305	15.95/11.54
8	NiCrAlY	DCL Dense 8YSZ + LZ	140 + 292	7.24/11.54
9	NiCrAlY	SCL porous 8YSZ	452	15.95

Both SCL and DCL TBCs systems and the free-standing samples were used to observe the cross-sectional microstructure. All of the samples were sectioned and mounted by the cold-mounting method with epoxy and hardener. A significant benefit gained by using cold-mount materials is that the epoxy can impregnate and fill surface-connected pores, which can provide a strong support to the porous sample [10]. The microstructures of the complete TBCs system samples were observed using an optical microscope, and the free standing samples were examined by a scanning electron microscope (SEM; JEOL, JSM–5610, Japan).

The optical images of cross-sectional microstructures of the as-prepared TBC specimens are shown in Figure 2.6. The LZ thermal barrier coatings were deposited above the bond coat (white layer). LZ with different thicknesses and porosities can be well deposited on the bond coat without delamination or cracking at the interface. Figure 2.6 illustrates that all LZ top coats have lots of pores, but without large cracks. The coating thickness decreased from sample 1 to sample 5, while porosity increased

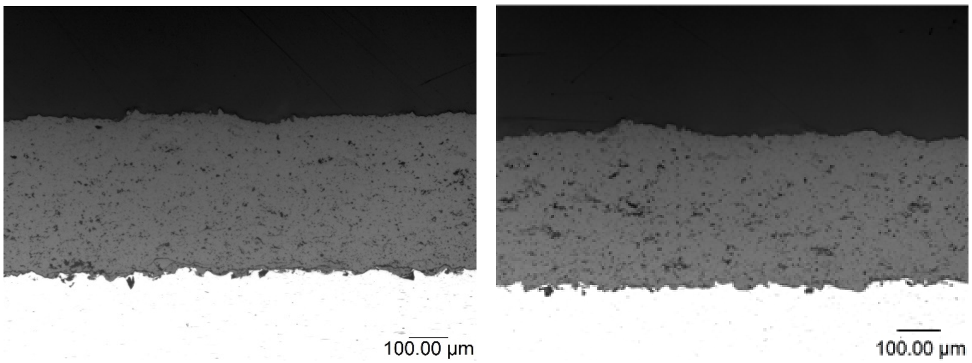

(a) Sample 1 (b) Sample 2

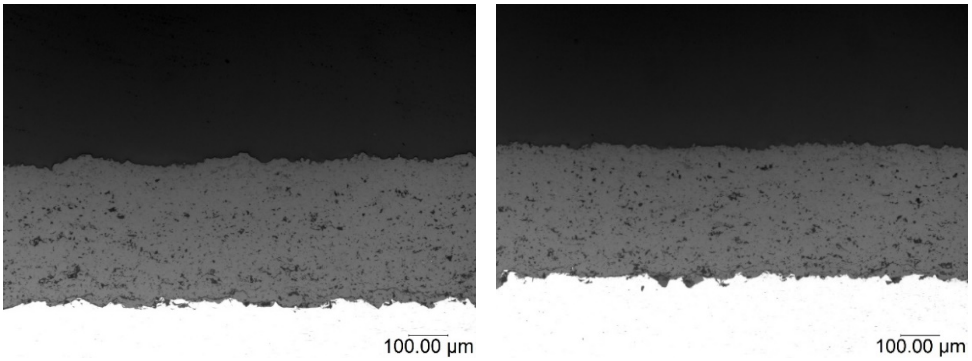

(c) Sample 3 (d) Sample 4

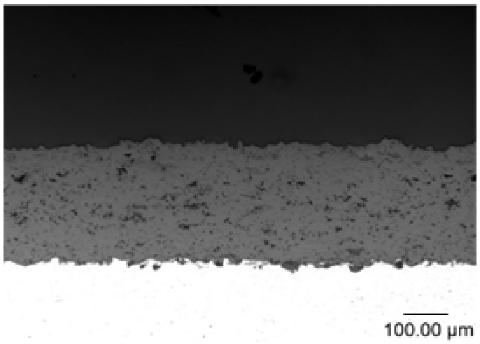

(e) Sample 5

Figure 2.6. Optical microscope images of SCL LZ samples.

from sample 1 to sample 5. Relatively larger defects such as pores and unmelted particles were increased from sample 1 to sample 5.

Figure 2.7 shows the SEM images of SCL LZ free-standing samples. It illustrates the detailed microstructure for samples of various porosity. The microstructures show

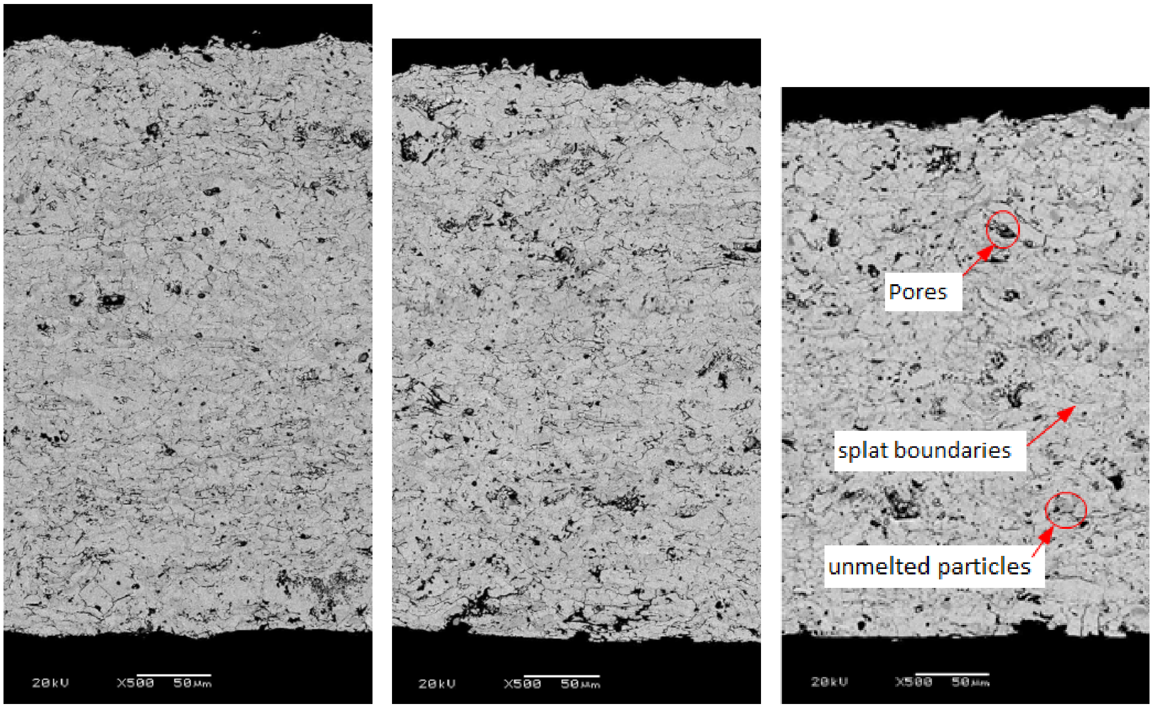

(a) Sample 1 (b) Sample 2 (c) Sample 3

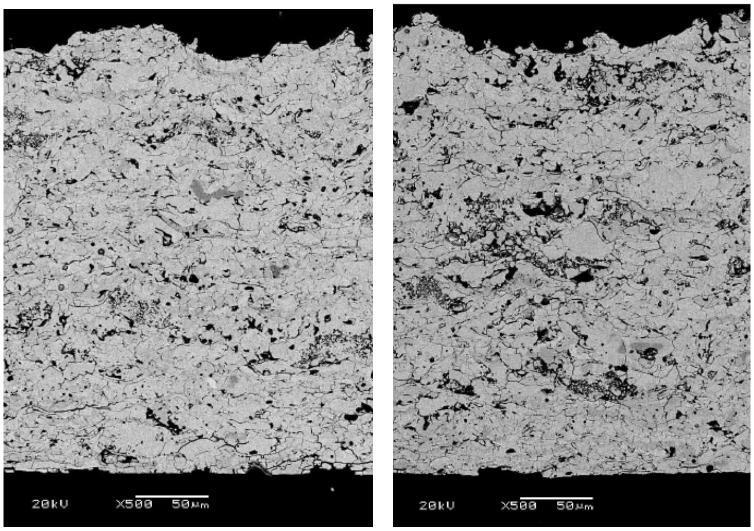

(d) Sample 4 (e) Sample 5

Figure 2.7. SEM images of LZ cross section microstructures.

a lot of intrinsic defects, such as pores, unmelted particles and splat boundaries in the coat preparation process. In Figure 2.6(e) sample 5 shows obviously higher porosity than sample 1 – sample 4. Different pores in various morphologies can be spotted, and some of the unmelted feedstock powders can also be found in SEM microstructure images. In general, the microstructures in Figure 2.6 and Figure 2.7 indicated that the amount and dimension of the defects are proportional to the porosity measurements shown in Table 2.2. As the standoff distance increases, the defects in the microstructure increase. So, the coatings with relatively accurate porosity can be achieved using the proper standoff distance.

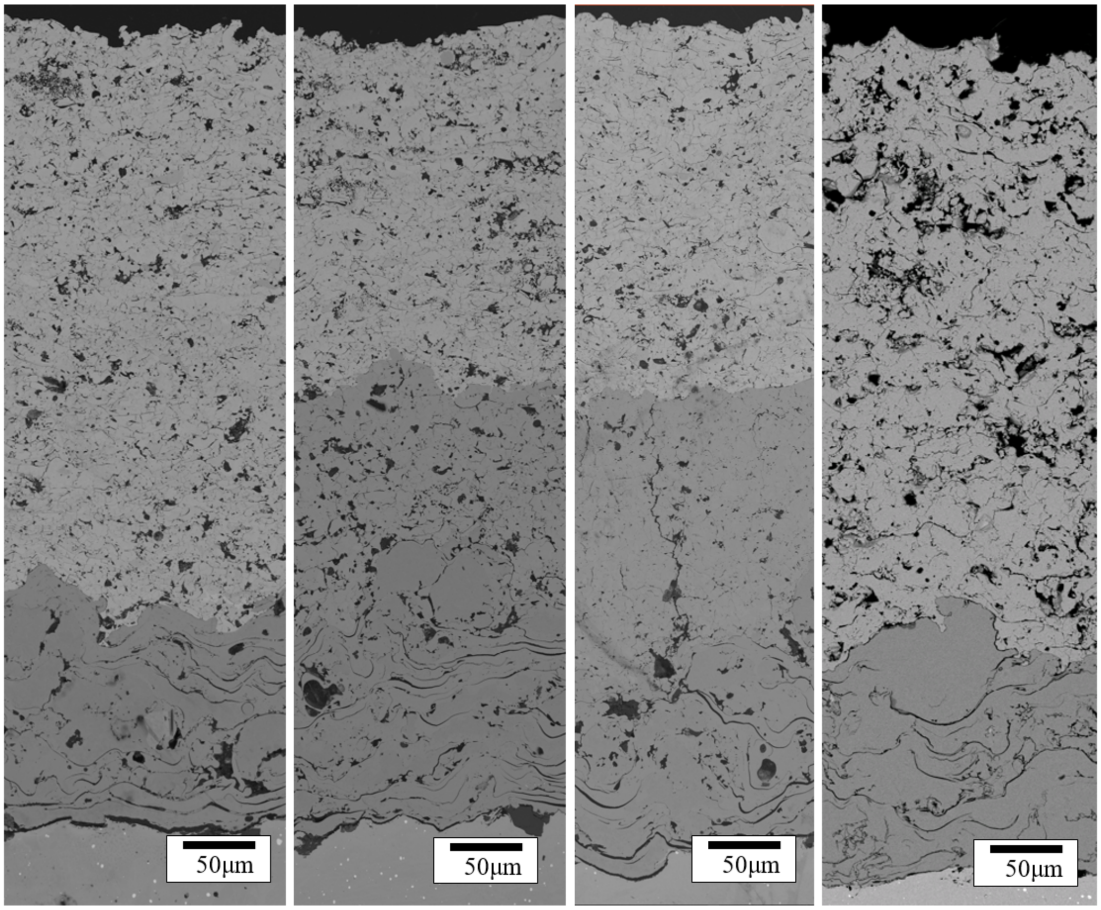

(a) Sample 6 (b) Sample 7 (c)Sample 8 (d)Sample 9

Figure 2.8. Microstructure of as-sprayed SCL and DCL samples.

That the pores constituted a large portion of total porosity can be clearly illustrated from the microstructure as shown in Figure 2.7. The distribution and the size of the pores are not uniform in all samples. The porosity has a large influence on thermal and mechanical properties. With a large number of pores and cracks in TBCs, the mechanical properties will have a severe change.

The microstructure images of as-sprayed DCL and SCL LZ/8YSZ layered coating are shown in Figure 2.8. All of the coating shows a sound status without delamination. There is no TGO at the interface between the top coat and bond coat, suggesting the bond coat is not oxidized yet. Scattered pores and cracks are obvious in the porous LZ and 8YSZ layer, and vertical cracks are generated in the dense 8YSZ layers, which is good for the coating durability performance [106].

2.2.2 Diffusion Investigation at the Interface

Energy-dispersive X-ray spectroscopy (EDS) experiments were performed on sample 8 to detect the diffusion characteristic between the LZ and the 8YSZ layers in the bilayer TBC system. Before the EDS test, sample 8 was heat-treated at the temperature of 1080 °C for about 4 hours. Both Zr and La elements were tracked through a cross-sectional line in the sample. The relative proportion of Zr and La as a function of distance at the interface area is shown in Figure 2.9. There is no obvious diffusion of Zr and La elements between two layers. Since almost no diffusion occurred at the interface, the adhesion strength between the LZ and the 8YSZ layers primarily came from the mechanical binding such as friction and hook. As a result, the interface roughness is very important to the bond capacity of the layered coatings. Since there is no chemical interaction between the LZ and the 8YSZ coatings, the thermal and mechanical properties of LZ-based TBC are recognized as the primary factors to improve the operation performance and understand the mechanism of delamination.

2.2.3 Porosity Measurement

The density measurement for the LZ top coat was conducted using 432 μm thick free standing coatings that peeled off from the 10 mm cubic substrate. The

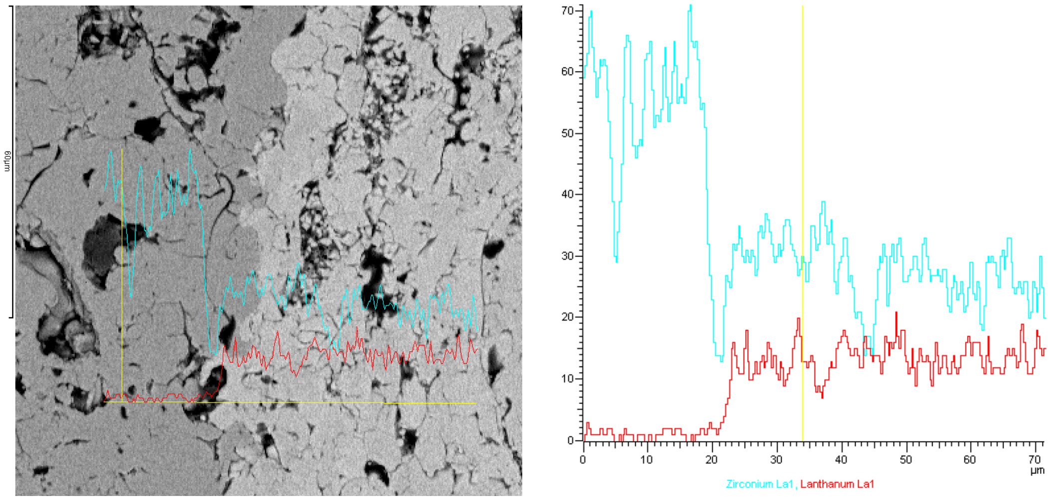

(a) (b)

Figure 2.9. EDS analysis at the interface between LZ and 8YSZ layers on sample 8.

density was measured following the ASTM standard B328-94, which is based on Archimedes' principle. The measurement apparatus includes an analytical balance (Mettler AE240, Switzerland) and a density determination kit (Denver Instrument, density kit, Arvada, Colorado).

The porosities and densities of the as-sprayed SCL samples deposited in the first batch are summarized in Table 2.2. The porosities range from 11.81 % to 16.52 %. The porosity values obtained here are calculated using the theoretical density of LZ 6.05 g/cm^3 [40]. Typically, the commercial APS 8YSZ coatings have a porosity of 10-20 % [5]. Since the mechanical properties of LZ will drop severely, it is important that the porosity can be restricted from 10% to 15% by controlling the APS parameters. Table 2.2 shows that when the standoff distance increases, the porosity increases as well.

The porosities of the second batch SCL and DCL LZ/8YSZ layered coatings are listed in Table 2.3. The free standing LZ top coat of sample 6 was used to measure the porosity and density of all the LZ coat layers because the densities of the LZ coat layers among sample 6, 7 and 8 are the same. The measured average densities and porosities of the LZ layer in samples 6, 7 and 8 were 5.35g/cm^3 and 11.54 %, respectively. Porosities in the dense and porous 8YSZ layers were 7.24 % and 15.95 %, respectively.

2.2.4 Hardness and Young's Modulus

The whole TBCs system samples (include top coat, bond coat, and substrate) were used to evaluate the mechanical properties. Vickers indentation experiments were applied on the cross-sectional mounted samples of the TBC system so that the hardness of each layer could be measured individually. The hardness values of the top coats were determined using a Vickers hardness tester (Mitutoyo Corp., HM114, Japan) with a Vickers tip for a load of 10 N and a nanoindenter (MTS, nanoindenter XP, Minnesota).

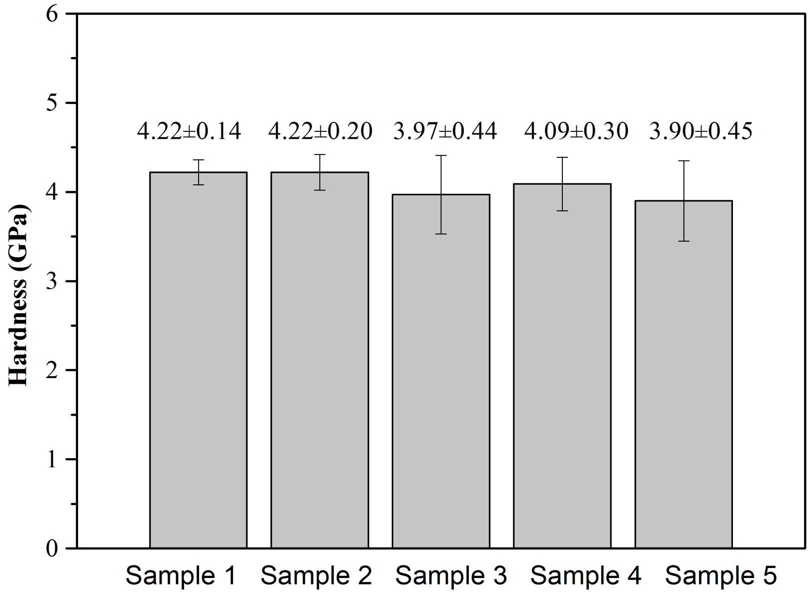

Figure 2.10. Vickers hardness of SCL LZ coatings sprayed in first batch.

The Vickers hardness results of SCL LZ samples that sprayed in the first batch were summarized in Figure 2.10. The hardness values in porous TBCs are not as easily and clearly defined as those in dense material since the "splat" boundaries and pores would influence the indentation measurement results. As a result, the data in Figure 2.10 show some variations.

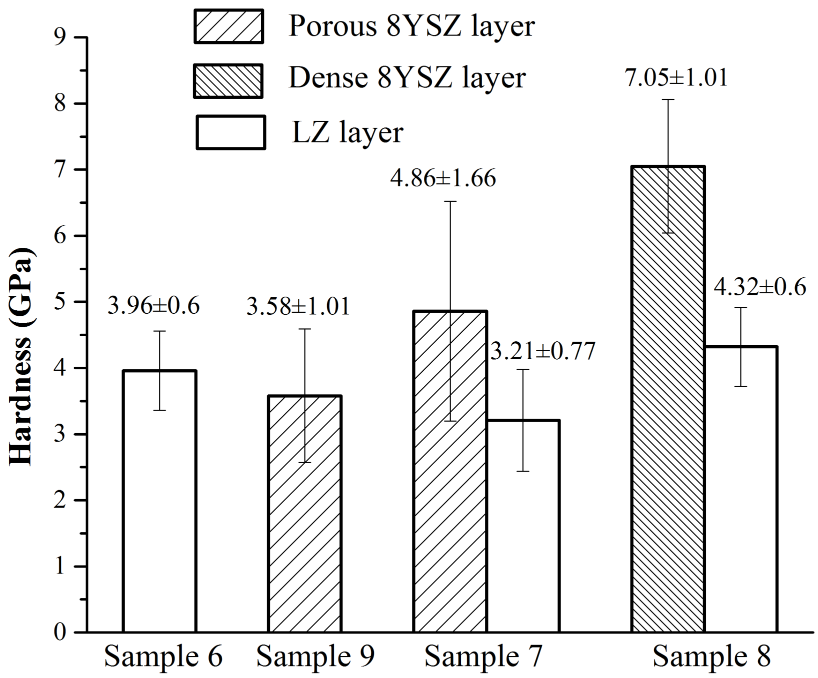

Figure 2.11. Vickers hardness in different layers of DCL TBC samples.

The hardness of sample 5 is the lowest, which is consistent with its low density and high porosity. Figure 2.10 shows the trend that the hardness will decrease as the porosities increase. Figure 2.11 shows the hardness results of the SCL and DCL LZ/8YSZ layered coatings, which were sprayed in the second batch. The hardness values of porous 8YSZ coats were similar to the LZ coats, as shown in Figure 2.11. The tiny difference might be due to the difference of porosity between these two coating layers. The hardness values of dense 8YSZ coats were much higher than that of other coats, due to the low porosity of the other coats. As a result, the hardness of the TBC coating is related to the porosity and the material species.

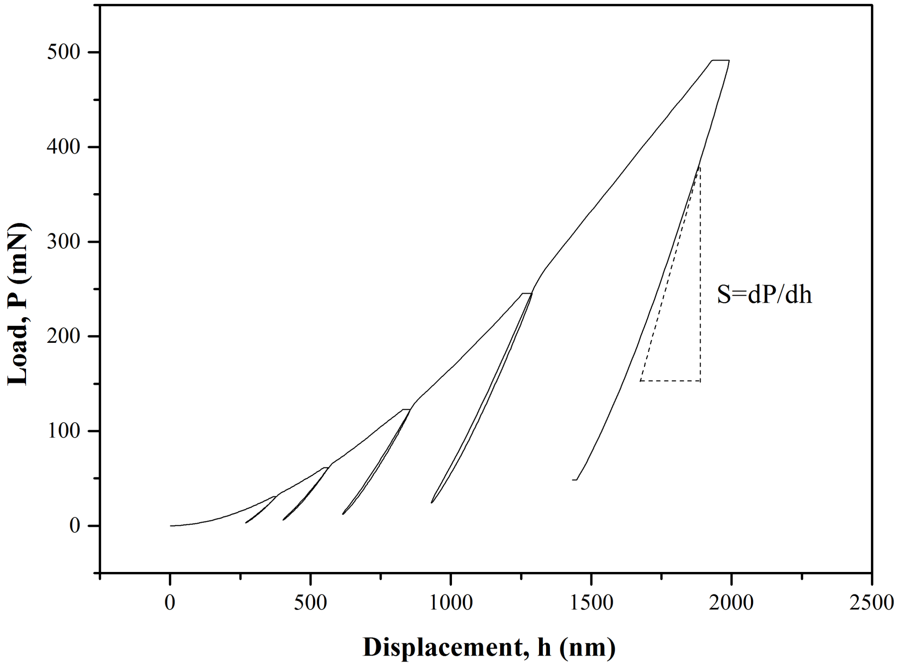

Figure 2.12. Nanoindentation load curve of sample 3, S represents the unloading stiffness.

The nanoindenter measures the hardness and Young's modulus by continuously monitoring the displacement of the indenter by a capacitance gauge as the load is applied. The nanoindentation hardness was performed using the calibrated shape of the diamond [107]. Nanoindentation employs the Berkovitch diamond indenter. There are two testing modes that can be applied in the nanoindentation tests: the depth control mode and the load control mode. In this study, the load control mode was employed. A sample load-displacement curve is shown Figure 2.12. In order to reach the predesignated 500 mN, five consecutive indentation movements were conducted at the same position. The hardness values can be obtained from each indentation. But when the indenter displacement was small, there are quite a lot of errors due to artificial effects in the experiments, such as surface roughness and contact angle. The accuracy can be improved with the increasing the displacement. As a result of that, the value obtained from the last curve was regarded as the true result in this study.

The nanoindentation hardness results of LZ coating sprayed in the first batch are summarized in Figure 2.13. The nanoindentation hardness normally has a higher value than the Vickers hardness because localized indentations, where pores can be avoided, were used. However, the variations of nanoindentation hardness were larger than Vickers hardness because of the complex microstructure in various indentation sites. These results indicate that nanoindentation hardness decreases as the porosity increases because the existence of the pores, splat boundaries, and cracks severely reduce the continuity of the coating, which causes the hardness decrease.

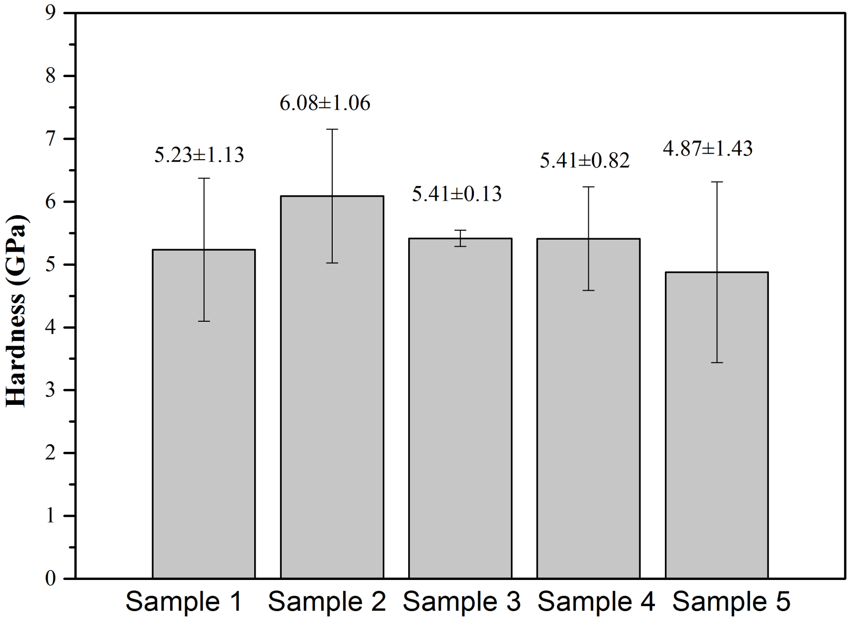

Figure 2.13. Nanoindentation hardness.

Young's modulus results were calculated from the slope of unloading parts in the load and displacement curve of nanoindentation measurements, as shown in Figure 2.12. During unloading, it is assumed that only the elastic displacements are recovered. Because of the elastic nature of the unloading curve, the elastic modulus can be analyzed. Figure 2.14 shows the calculated Young's modulus values. Sample 5 has a lower Young's modulus than sample 2,3 and 4. Comparing microstructure and porosity data, Young's modulus in LZ coating decreased as the porosity increased.

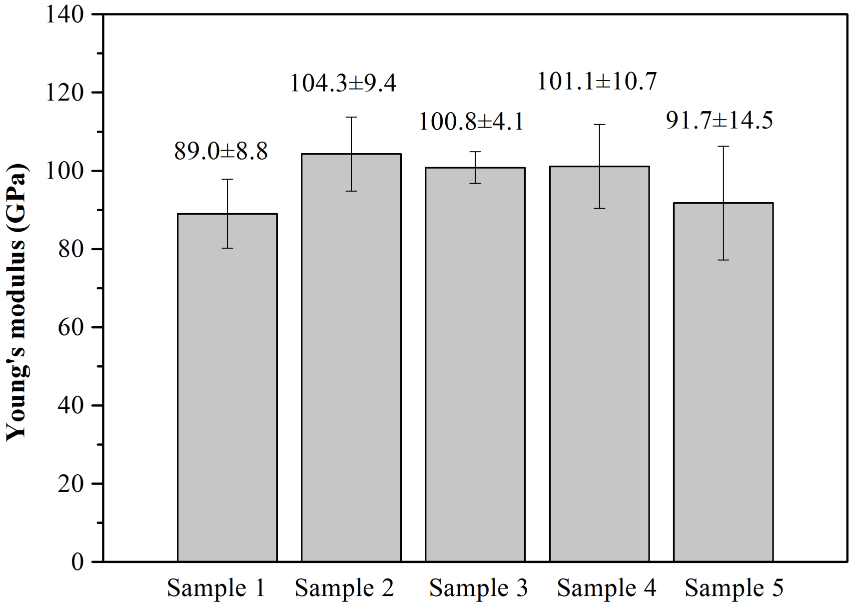

Figure 2.14. Young's modulus of SCL LZ TBC measured by nanoindentation.

The correlation between Young's modulus and nanoindentation hardness is investigated. In order to calculate Young's modulus, three important quantities must be measured in the load curve: the maximum load, P_{max}, the maximum displacement, h_{max}, and the elastic unloading stiffness, $S=dP_{max}/dh_{max}$, which is defined as the slope of the upper portion of the unloading curve during the initial stages of unloading as shown in Figure 2.12. The relationship between hardness (H) and Young's modulus (E) can be expressed by the following equation [108]:

$$\frac{P}{S^2} = \frac{\pi}{(2\beta)^2}\frac{H}{E^2} \tag{2.1}$$

where β is the correction factor and $\beta = 1.0226$ for the Berkovich diamond indenter [108]; P is the load force, and S is the stiffness. Figure 2.15 shows the correlation

relation of P/S^2 and H/E^2. The experiment results are shown by round dots. The theoretic P/S^2 value is calculated from Equation (2.1). The experiment's value is distributed around the theoretical line. As a result, P/S^2 and H/E^2 can be expressed as a linear relation.

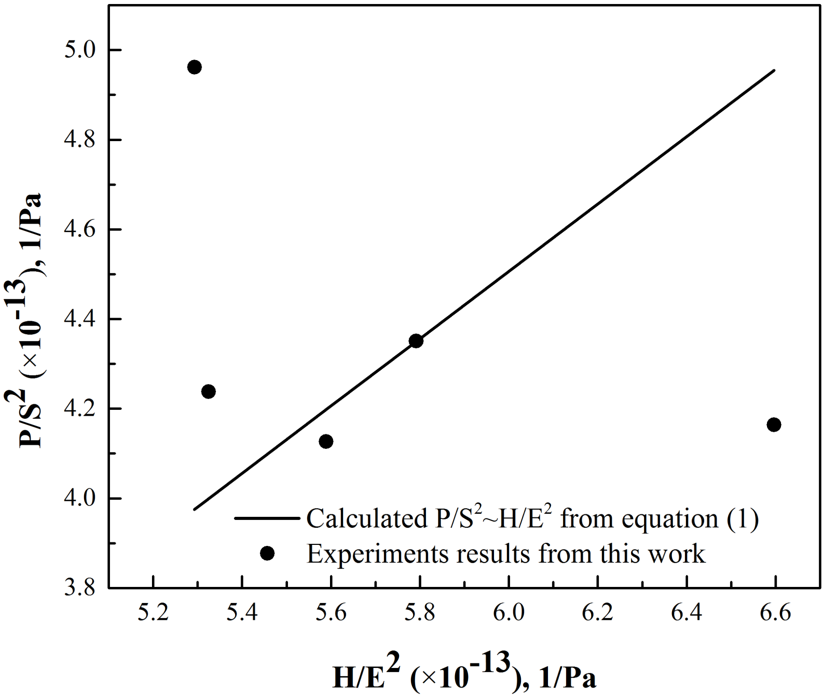

Figure 2.15. Nanoindentation P/S^2 and H/E^2 relations.

2.2.5 Bond Strength Between the LZ Coat and Bond Coat

Sufficient adhesion bond strength between the coating layers and bond coat is an important property for the TBC systems because the durability and integrity of the coating depend on the adhesion bond strength. Bond strength experiments were performed in this study to investigate the adhesion bond strength following ASTM C633. Epoxy (FM 1000 adhesive film) was used to glue the TBC's top coats to two cylinders. This bonding agent is capable of bonding the coating to the loading fixture with a tensile strength, which is at least larger than the minimum required adhesion strength of the coating. In addition, this FM 1000 has sufficient viscous not to penetrate through the coating. The adhesion or cohesion bond strength can be calculated by dividing the maximum load by the coating area.

Only the SCL LZ and 8YSZ coating samples (sample 6 and sample 9) were investigated in the bond strength test. Because the adhesion bond strength will be affected by various interfaces and layers in multiple layer coats, it is hard to determine the adhesion bond strength at a specific interface for the DCL.

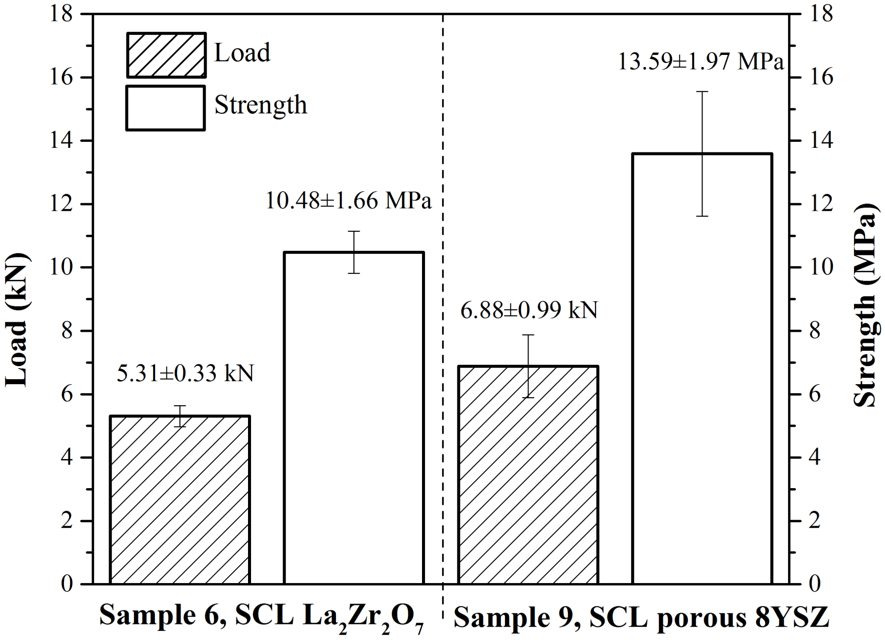

Figure 2.16. Load and bond strength results of bond strength tensile test.

As shown in Figure 2.16, the SCL 8YSZ sample can resist a higher load, so it has a higher adhesion bond strength than the SCL LZ coating. When the tensile stress is lower than the adhesion bond strength, the TBCs were intact. Local fracture occurs when the tensile and shear stresses in the coating layer equal the adhesion bond strength. There are typically two explanations for the failure mechanism: (1) the residual stress enhances the defects inside the ceramic layer, which will lead to the delamination, and (2) the increasing tensile and shear stresses enhances the tendency of cracking [109].

The LZ coats have lower fracture toughness than 8YSZ coats (2.2 – 3.3 MPa·m$^{1/2}$ for YSZ and 1.1 ± 0.2 MPa·m$^{1/2}$ for LZ), which means LZ coats are easy to break [15, 50, 51]. As a result, the SCL LZ coating sample had a lower adhesion bond strength than SCL porous 8YSZ in this work.

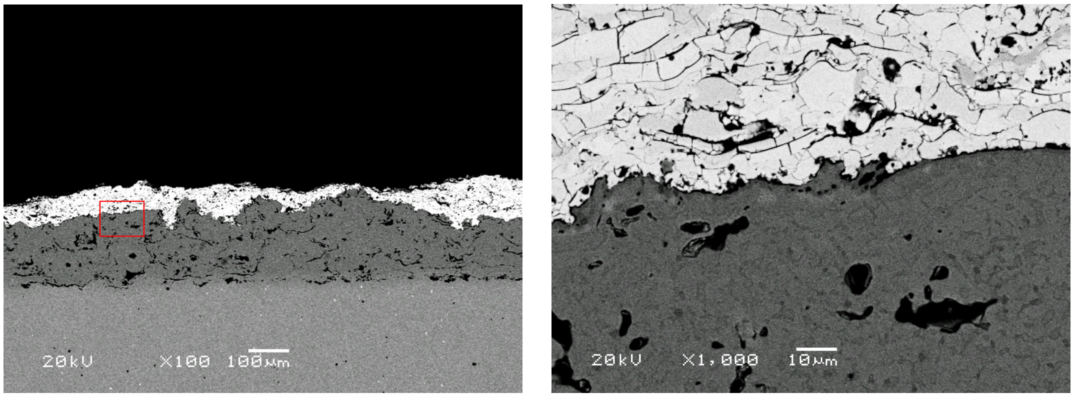

(a) Sample 6, x100 (b) Sample 6, x1000

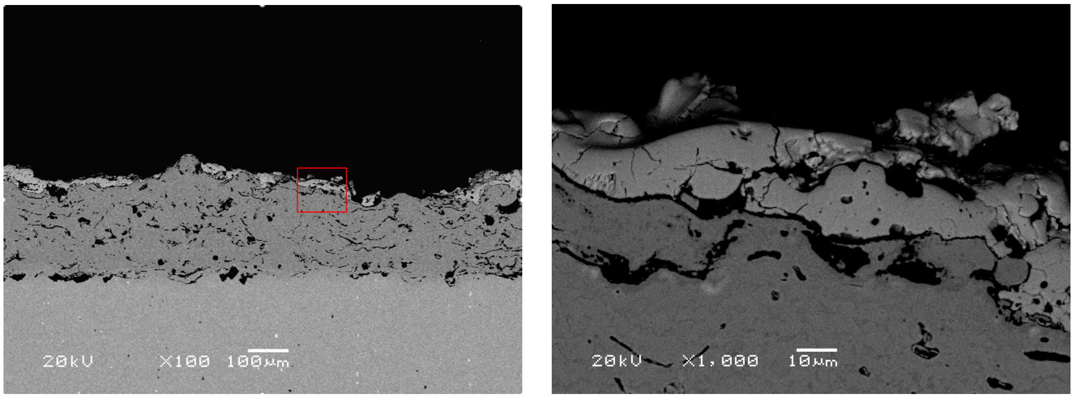

(c) Sample 9, x100 (d) Sample 9, x1000

Figure 2.17. SEM images at the interface of SCL LZ and 8YSZ coating in different magnification levels.

Figure 2.17 shows the cross sectional SEM images of the TBC systems after the bond strength tests. There is almost no TGO layer at the interface between the top and bond coat, so the TGO layer is not the main reason of spallation. The spallation occurs predominantly near the interface between the top coat and the bond coat, although the spallation does not occur exactly at the interface. Although the porosity of LZ and 8YSZ are similar, the LZ coat samples have scattered "splats" grains. The microstructure shows the net-shape cracks inside the LZ layer. The cracks are easy to propagate in grain boundaries. However, in the remnant 8YSZ layer, it shows fewer grain boundaries but much larger pores than the LZ layer. As a result, there are fewer initial crack resources in the 8YSZ layer, and its grains are connected better than the LZ layer.

Since the sprayed coating samples are cooled in ambient environment from the elevated deposition temperature. Thermal residual stress is originated in the TBC layers, due to the different coefficient of thermal expansion in each TBC layers. The residual stress is generated mainly from the strain mismatch among the coating layers and the substrate when the TBC systems are cooled from the high temperature to the room temperature. When the coatings are cooled from the high temperature, the volume of substrate shrinks more than that of the coatings due to the higher coefficient of thermal expansion. Considering the displace compatibility, compression stress is applied in the ceramic coating layers and tension stress is applied in the substrate. To calculate the residual stress in multiple layer coatings, the interface between the substrate and the bond coat is defined as the origin plane, where z=0. The distance from the ith layer to the substrate is defined as h$_i$ [110–112]. The thermal residual stress in the substrate and ith coating layer, which relates to the misfit strain ε_i and the bending curvature K, can be expressed by [110, 112]:

$$\sigma_s = E_s[\varepsilon_s + K(Z + \delta)] \qquad (-ts \leq z \leq 0) \tag{2.2}$$

$$\sigma_i = E_i[\varepsilon_i + K(Z + \delta)] \qquad (1 \leq i \leq n, h_{i-1} \leq z \leq h_i) \tag{2.3}$$

where E$_s$ and E$_i$ are Young's modulus of substrate and i$_{th}$ coating layer. δ is the distance from the bending axis, where the bending strain is zero. ε_i, ε_s, K and δ can be expressed by the following equations [113].

$$\varepsilon_s = -\sum_{i=1}^{n} \frac{E_i t_i}{E_s t_s} \Delta\alpha\Delta T \tag{2.4}$$

$$\varepsilon_i = \Delta\alpha\Delta T + \sum_{k=1}^{n} \frac{E_k t_k}{E_s t_s}(\alpha_k - \alpha_i)\Delta T \tag{2.5}$$

$$\delta = \frac{t_s}{2} - \sum_{i=1}^{n} \frac{E_i t_i}{E_s t_s}(2h_{i-1} + t_i) \tag{2.6}$$

$$K = -\sum_{i=1}^{n} \frac{6E_i t_i \Delta\alpha\Delta T}{E_s {t_s}^2} \tag{2.7}$$

where α is the coefficient of thermal expansion (CTE), k is the ceramic coating layers range from 1 to n, t_i is the thickness of i^{th} layer.

The thermal residual stress curves calculated by Equation (2.2)–(2.7) and the Townsend model are shown in Figure 2.18 [111]. The compressive residual stress difference at the interface of the SCL LZ coat is about 3 GPa larger than that of the SCL porous 8YSZ at Δ T= 400 K.

Because of the large residual stress difference, there are more defects, such as grain boundaries and pores, at the interface between the top coat and the bond coat in the SCL LZ TBCs than that in the SCL 8YSZ TBCs, as shown in Figure 2.17(b) and 2.17(d). Since there are more distributed grain boundaries in the LZ layer than in the 8YSZ layer, so the LZ ceramic layer is easy to break. In addition, the LZ layer is much weaker than the bond coat due to its low fracture toughness and scattered boundaries [50], so the delamination occurs in the LZ coating layer instead of at the interface. The magnitude of residual stress in the SCL LZ TBCs is larger than that in the SCL 8YSZ TBCs. The bond strength in the LZ sample is lower than that of 8YSZ sample, which means that the spallation occurs easier in LZ coating than in 8YSZ coating. As a result, the delamination is due to the lower fracture toughness of LZ and higher residual stress in the LZ coating layer.

2.2.6 Erosion Test

The Erosion resistance tests are performed according to the ASTM G76-13 standard. Alumina sand with a particle size of 50 μm is applied as the erosive material, and 600 g sand is used for each sample. The speed of sand stream is 6 g/s, and the

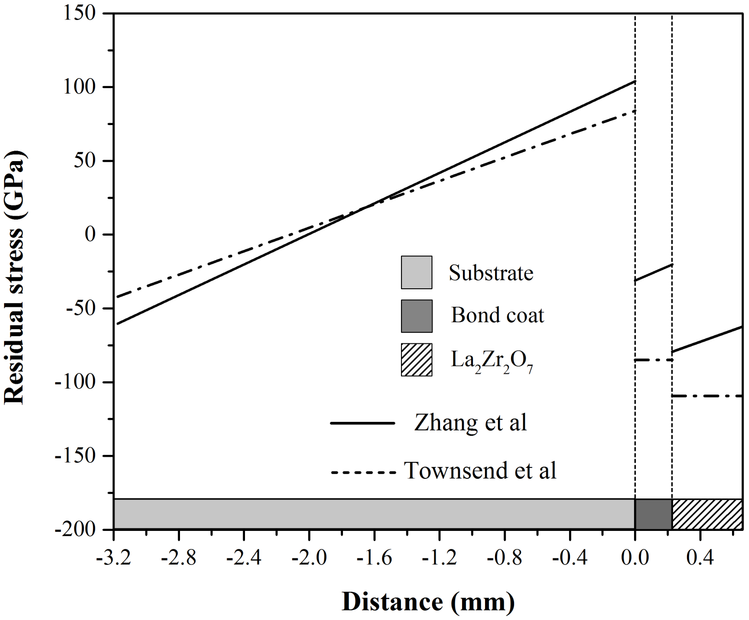

(a) Residual stress distribution in Sample 6

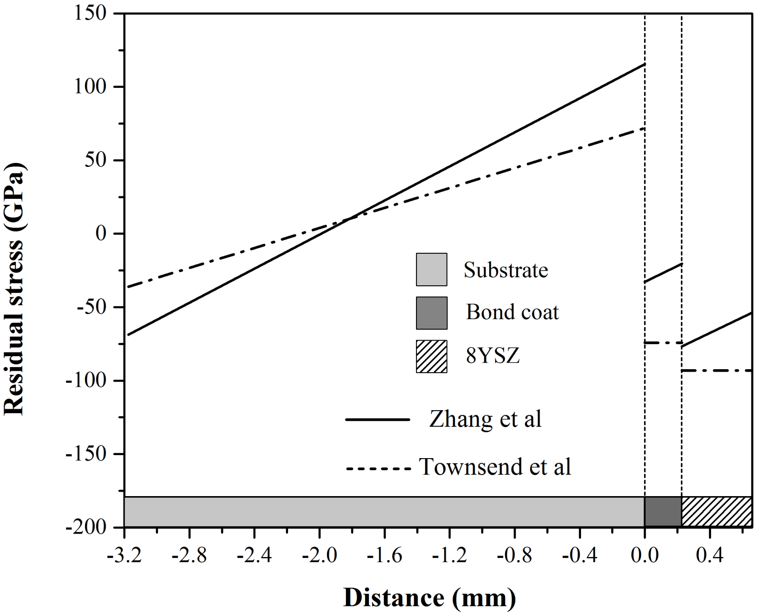

(b) Residual stress distribution in Sample 9

Figure 2.18. Residual stress distribution as a function of thickness at ΔT=400 K.

impingement angle is 20 °. The erosion rate (μg/g) is used to evaluate the erosion resistant performance in this experiment, which is calculated by dividing the removed TBC weight (μg) by the erosive material weight (g).

Figure 2.19 summarizes the erosion rate values of the four TBC samples. The SCL porous 8YSZ coating sample has the lowest erosion rates, which is about only half of the other sample's erosion rate. The erosion rates of the LZ coating layers in all samples are much higher than that of the 8YSZ layer. However, the DCL dense 8YSZ + LZ has relatively lower erosion rates than other LZ-based coatings.

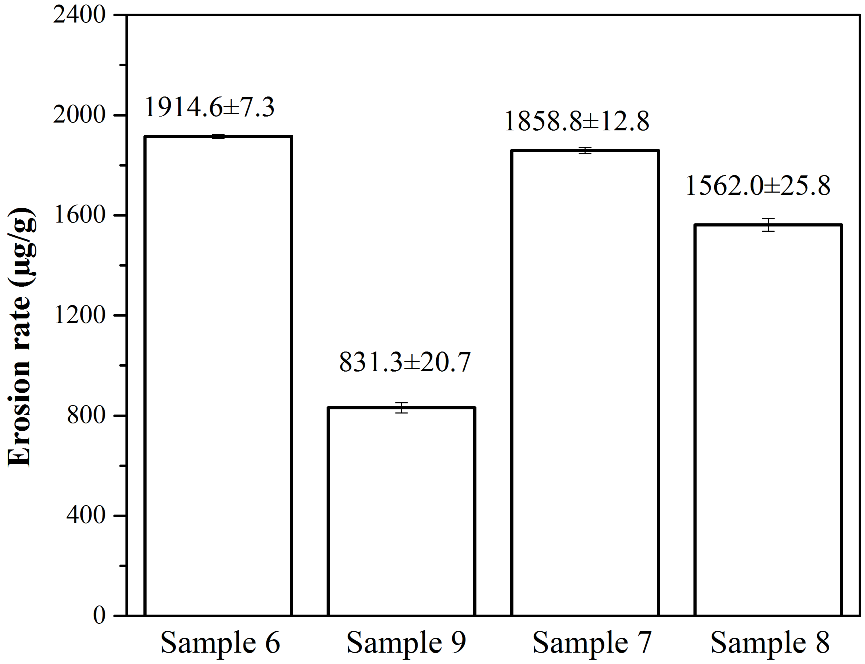

Figure 2.19. Erosion rate.

Figure 2.20 shows the optical images of TBC samples after the erosion tests. Although the SCL 8YSZ sample has lower erosion rate, the center of this coating sample is penetrated, as shown in Figure 2.20(d). The substrate of sample 9 is exposed, so this small hole can lead to lethal failure of the entire coating system. Similarly, the bond coats of both sample 6 and 7 are penetrated, as shown in Figure 2.20(a) and Figure 2.20(b). Figure 2.20(b) shows three concentric ellipses, they represent LZ, porous 8YSZ, the bond coat and substrate respectively from outside to inside. The dark solid ellipse area in Figure 2.20(c) is the dense 8YSZ layer, which is not penetrated. However, all the LZ top coat layer and part of the 8YSZ layer are removed in this ellipse region.

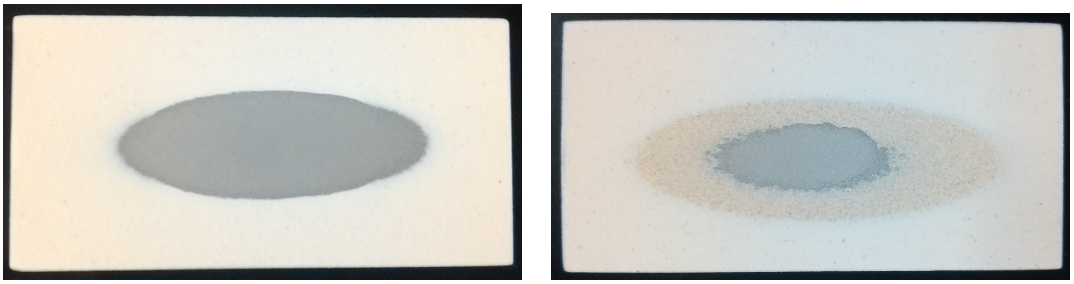

(a) Sample 6 (b) Sample 7

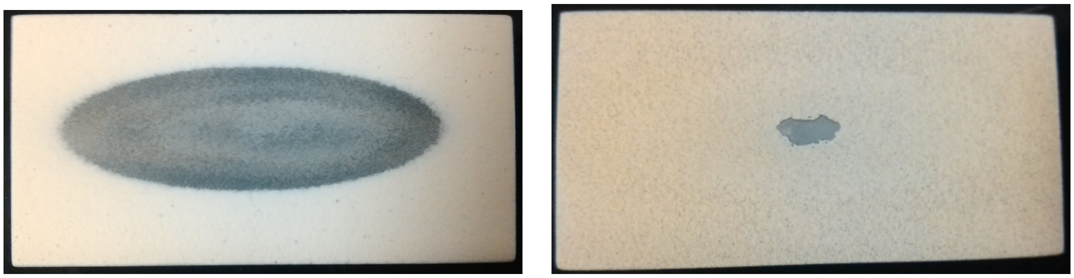

(c) Sample 8 (d) Sample 9

Figure 2.20. Optical images of erosion test.

The cross-sectional SEM images of the erosion samples are shown in Figure 2.21. As shown in Figure 2.21(a), the removed part is very large in the SCL LZ coating layer, but both two edges are still connected with the substrate. As shown in Figure 2.21(b), both the two top coat layers of the DCL porous 8YSZ + LZ coating are removed in the center. There are more porous 8YSZ layers left than the LZ layer. However, the interface between each layer in sample 7 is connected in a good shape. As shown in Figure 2.21(c) although there is a great loss in the LZ layer, the dense 8YSZ layer is almost intact. The interface between the dense 8YSZ layer and the substrate is also intact. As shown in Figure 2.21(d), although the erosion hole is relatively small, the porous 8YSZ top coat in this cross-sectional image is detached from the substrate.

(a) Sample 6

(b) Sample 7

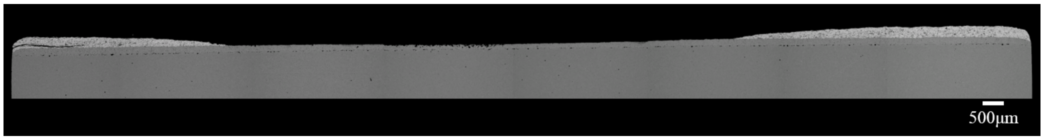

(c) Sample 8

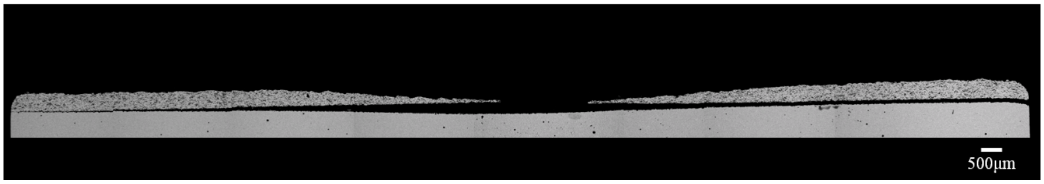

(d) Sample 9

Figure 2.21. Across section SEM images of the erosion samples.

The SEM images at the edge of the erosion areas are shown in Figure 2.22. As shown in Figure 2.22(a) and Figure 2.22(d), both SCL porous 8YSZ and SCL LZ layers are delaminated from the substrate at the interface area. However, the double layer coatings have sound interfaces, as shown in Figure 2.22(b) and Figure 2.22(c).

The 8YSZ coating shows better erosion resistant performance than the LZ coating because the fracture toughness of the 8YSZ is higher than that of the LZ. In addition, the hardness of the dense 8YSZ layers is higher than the other TBC layers, so the erosion rate of the dense 8YSZ layer is the lowest.

Erosion model of brittle material, such as the top coat in TBC, can be described using the indentation theory of the abrasive particle, which relates to the Young's modulus (E) and the fracture toughness (K_{IC}) of the brittle material and the erosion

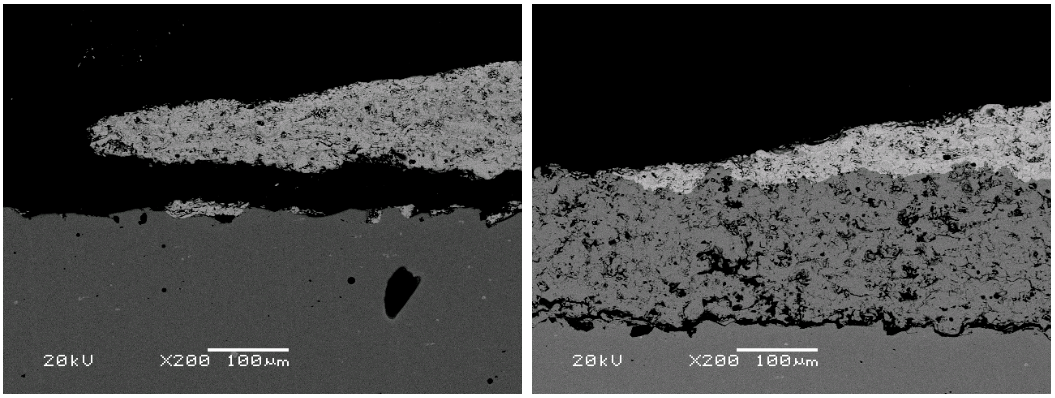

(a) Sample 6 (b) Sample 7

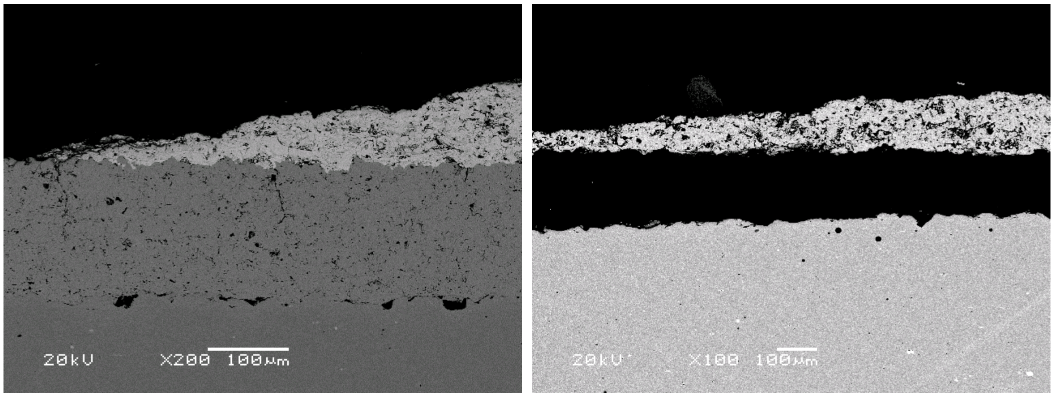

(c) Sample 8 (d) Sample 9

Figure 2.22. SEM images at the edge of the erosion area.

conditions, such as impact velocity and abrasive particle size [114–117]. The erosion model describes a threshold condition when the impinging particles initiate a crack in a specific target material. The critical velocity is applied to express the threshold condition to initiate the crack. Wellman proposed a critical velocity model, which is expressed by the following equation [118].

$$V_{critical} = 105\frac{E^{3/4}K_{IC}^{3}}{H^{13/4}\rho^{1/2}R^{3/2}} \tag{2.8}$$

where E is Young's modulus, H is hardness, K$_{IC}$ is fracture toughness, ρ is the density of the abrasive particles and R is the particle radius. As the LZ has a lower K$_{IC}$ than the 8YSZ, lower erosion resistance of the LZ in the erosion test is expected [119].

The calculated critical erosion velocities for each sample are shown in Figure 2.23. The critical velocities of the LZ coating layers are much less than that of the 8YSZ coating layers, so the erosion rate of the SCL LZ TBCs is larger than of the SCL 8YSZ TBCs. Compare sample 7 (DCL porous 8YSZ+ LZ) with sample 8 (DCL dense 8YSZ+ LZ), the critical velocity of top layer LZ in samples 8 is larger than that of sample 7, so sample 8 has lower erosion rate than sample 7.

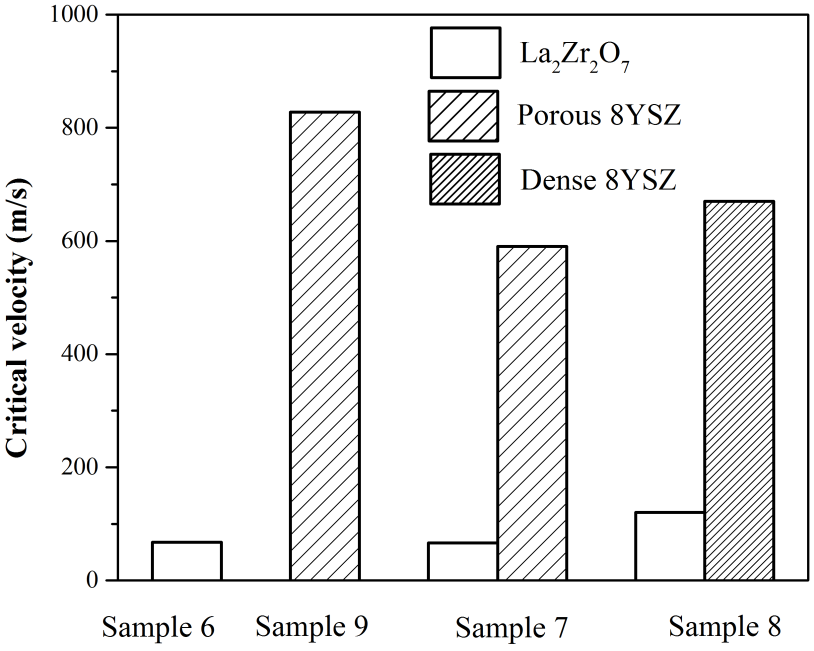

Figure 2.23. Critical erosion velocity.

Figure 2.24 shows the reciprocal value of critical velocity as a function of erosion rate. The scattered point can be fitted into a linear line, whose function is y=9.56e^{-6}x-0.00739.

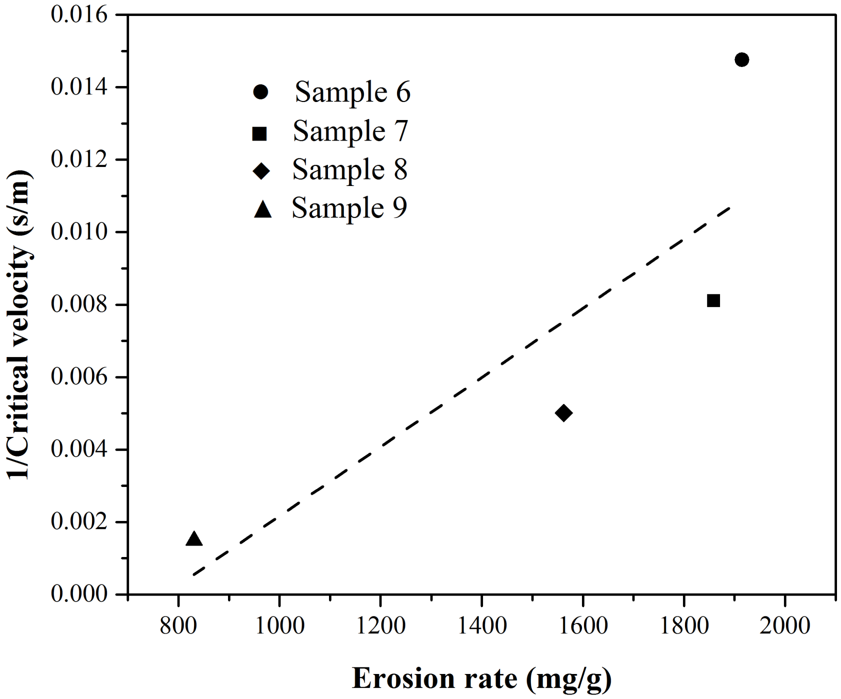

Figure 2.24. Relationship between critical erosion velocity and erosion rate.

2.3 Thermal Properties and Stability of Layered LZ Coating

2.3.1 Thermal Conductivity

For the TBC materials, the most important material property is thermal conductivity. There are several experimental methods to measure the thermal conductivity. The most widely used one is the flash method, which is first proposed by Parker et al. [63]. Three thermal properties - thermal diffusivity, specific heat capacity, and thermal conductivity - can be deduced simultaneously using one sample [63]. The flash method is designated as a standard method to measure thermal diffusivity, which is described in ASTM E1461-11 standard. The measurement error of the flash method is less than 5 % [120].

In this work, the thermal conductivities were calculated from thermal diffusivity D_{th}(t), specific heat capacity C_p(t) (from literature [15]) and density ρ(t). It can be expressed by the follow equation [40]:

$$\kappa = D_{th}(t) \cdot C_p(t) \cdot \rho(t) \tag{2.9}$$

where thermal diffusivity D_{th}(t) were measured by a laser flash diffusivity systems (TA instrument DLF1200, Delaware, USA).

The thermal conductivity curves of the as-sprayed SCL LZ coating and the SCL porous 8YSZ coating (sample 6 and sample 9) are plotted in Figure 2.25. Three thermal conductivity measurements were conducted for the LZ coatings at each temperature setting (297 K, 377K, 477K, 579K, 676K, 776 K, 874 K, 974 K, 1072K and 1172 K). The measured average thermal conductivity of the LZ is about 0.59 – 0.68 W/m/K in the temperature range of 297 to 1172 K (24 – 899 °C), which is about 25 % lower than that of the porous 8YSZ (0.84 – 0.87 W/m/K) in the same temperature range. The thickness of the porous LZ top coat varies from 450 to 550 μm. The density of the sprayed LZ coating is 5.35 g/cm^3, and the corresponding porosity is 11.54 %. The porosity is essential for reducing thermal conductivity and maintaining the resistance to fracture, erosion and foreign object damage [44]

2.3.2 Coefficient of Thermal Expansion

The thermal expansion coefficient (CTE, sample size 5 mm in width, 25 mm in length and 0.43 mm in thickness) were measured by using a BAEHR dilatometer DIL 802 (now belonging to TA instrument, Delaware) at temperatures ranging from room temperature to 1673 K (1400 °C).

The CTE values measured on sample 6 (SCL LZ coating) and sample 9 (SCL porous 8YSZ coating) in this study are shown in Figure 2.26. CTE values of the LZ change very little when the temperature is above 400 K. The CTE values of the LZ are about 9–10×10^{-6} K^{-1} from 400 K (127 °C) to 1600 K (1327 °C), which are very close to the reported literature data [40,59,121]. Although the porosity of 8YSZ

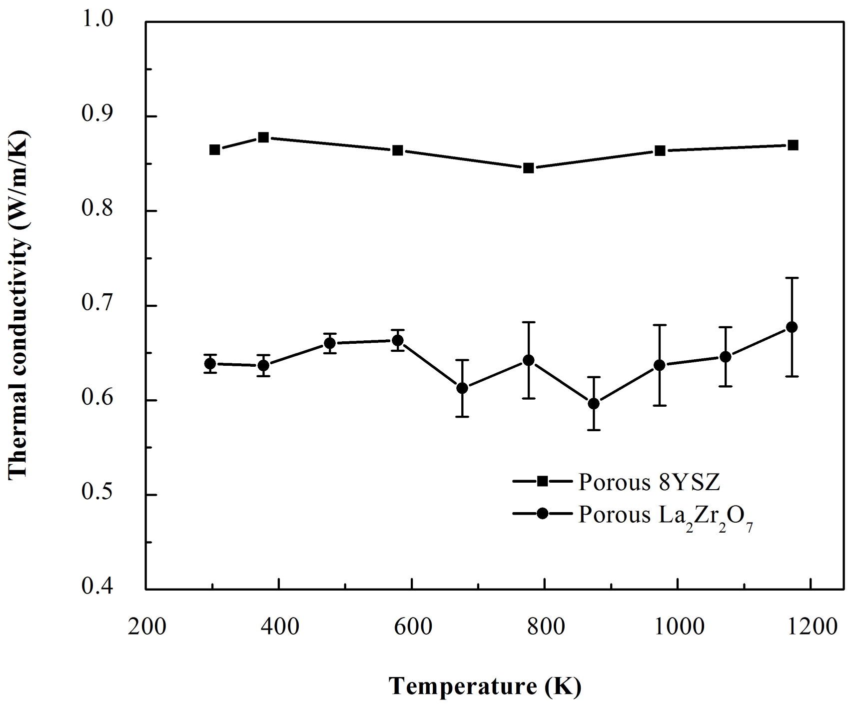

Figure 2.25. Thermal conductivity of sample 6 and sample 9 as a function of temperature. The curves are a guide to the eye.

coating is higher than that of the LZ coating, the CTE values of the LZ are about 10 % lower than those of the porous 8YSZ, which are 10–11×10^{-6} K^{-1} in the same temperature range [67,122]. This indicates that the LZ coating has a lower CTE than the 8YSZ coating in the same porosity level. Due to the CTE difference between the 8YSZ and the LZ, a thermal mismatch is generated at the interface between the 8YSZ layer and the LZ layer during the thermal shock and thermal cycling tests. As the NiCrAlY bond coat has much higher CTEs (about 15×10^{-6} K^{-1} at 1273 K) than the 8YSZ [9], a larger thermal mismatch between the bond coat and the LZ top coat is expected during thermal shock and thermal cycling tests.

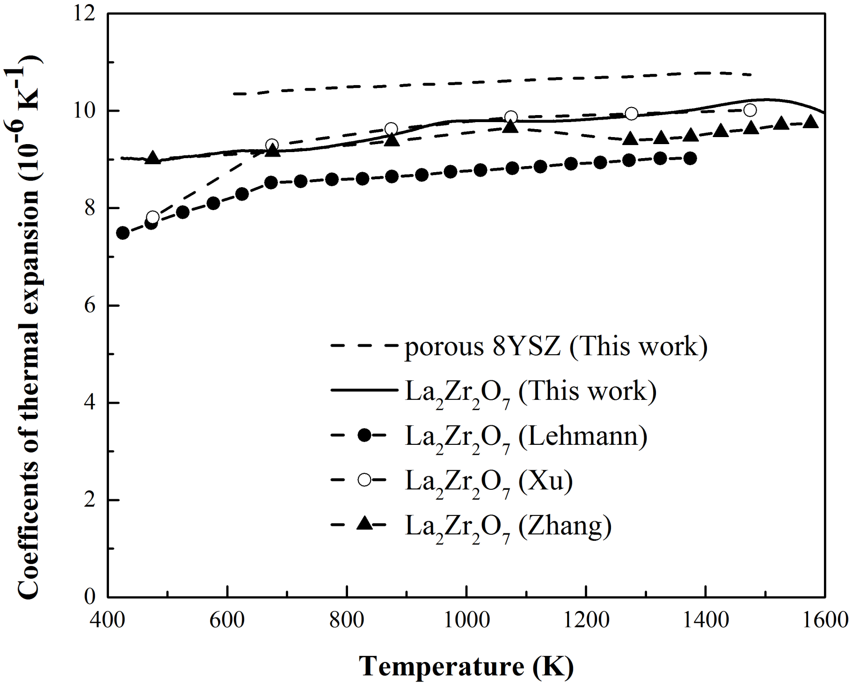

Figure 2.26. CTE curves of LZ and 8YSZ as a function of temperature.

2.3.3 Heat Treatment Test

Furnace heat treatment tests were conducted on sample 6, 7, 8 and 9 with round button substrate in a diameter of 25.4 mm (1 inch) at 1353 K (1080 °C) for 4 hrs in an argon atmosphere.

The optical images of the TBC samples before and after the furnace heat treatment are summarized in Figure 2.27. After furnace heat treatment for 4 hrs, the sample 6 (SCL LZ coating, Figure 2.27(a)) and sample 8 (the DCL with the dense 8YSZ and LZ layers, Figure 2.27(c)) were completely delaminated. One of the main reasons for the failure is the CTE differences among the bond coat, the 8YSZ layer, and the LZ layer. In the isothermal heating process, the volume change due to the thermal expansion mismatch between the bond coat and the LZ layer leads to high thermal residual stresses, which initiates cracks in ceramic top coats, as shown in the calculated residual stress distribution in Figure 2.31. Additionally, the fracture toughness of LZ is ∼1.1 MPa·m$^{1/2}$, which is much lower than that of 8YSZ (2.0 MPa·m$^{1/2}$) [15,51]. As a result, the cracks tend to be extended inside the LZ coating layer in the early stage of heat treatment. The failure ultimately occurs in the LZ coating layer due to its low fracture toughness and the CTE mismatch between the bond coat and the LZ layer or between the LZ and the 8YSZ layers. In contrast with the finding for sample 8 (Figure 2.27(c)), the sample 7 (DCL with the porous 8YSZ and LZ layers) is partially cracked on the edge, which only takes up about 10% of the coated area, as shown in Figure 2.27(b). As the porosity of the porous 8YSZ coating is more than two times higher than that of the dense 8YSZ coating, the porous 8YSZ coating has greater compliance to accommodate the volume mismatch caused by the CTE differences, so the double-layer top coat of the sample 7 survives in the heat treatment test. On the other hand, the low compatibility of the dense 8YSZ coating in sample 8 lead to its complete failure in the heat treatment. As shown in Figure 2.27(d), the sample 9 (SCL porous 8YSZ coating) is in good condition after heat treatment for 4 hrs, suggesting the porous 8YSZ layer has good adhesion in TBC systems.

Figure 2.28 shows the SEM images of the cross-sectional view of TBC microstructure after heat treatment for 4 hrs. Except for sample 9 (Figure 2.28d), delamination in all of the samples occurs in the LZ layer (The SEM microstructure image of sample 7 was taken at the delaminated area). Therefore, CTE difference is not the only reason for delamination of the single-layer LZ coating. The occurrence of cracks is also related to fracture toughness [123]. The Delamination can easily occurs in the single-layer LZ coating due to the low fracture toughness of the LZ. The Failure in the LZ coating is likely caused by a combination of its low fracture toughness and high stresses created by CTE mismatch. Levi et al. proposed that the elastic energy played a critical role in TBC systems to determine the lifetime of coating [124].When the elastic energy reaches the critical value, delamination occurs. The elastic energy is determined by the coating thickness, Young's modulus, and CTE [124]. The cause of delamination in sample 8 is similar to the SCL LZ coating, namely a combined effect of both CTE difference and low fracture toughness of LZ.

(a) Sample 6 (b) Sample 7

(c) Sample 8 (d) Sample 9

Figure 2.27. Optical images of the TBC samples after furnace heat treatment.

In addition, the heat treatments were also performed on TGMF dog-bone samples at 1353 K (1080 °C) for 4 hrs. However, the TGMF tensile bar samples show a better performance than the aforementioned round button samples. Only the SCL LZ TGMF sample is delaminated. The SCL 8YSZ and the DCL coatings are in a good condition after 4 hrs heat treatment. The delamination of single-layer LZ coating is primarily due to the week fracture toughness of the LZ coating. The volume change due to the discrepancy of thermal expansion coefficient between bond coat and LZ coat leads to high thermal stress. The failure ultimately occurs due to

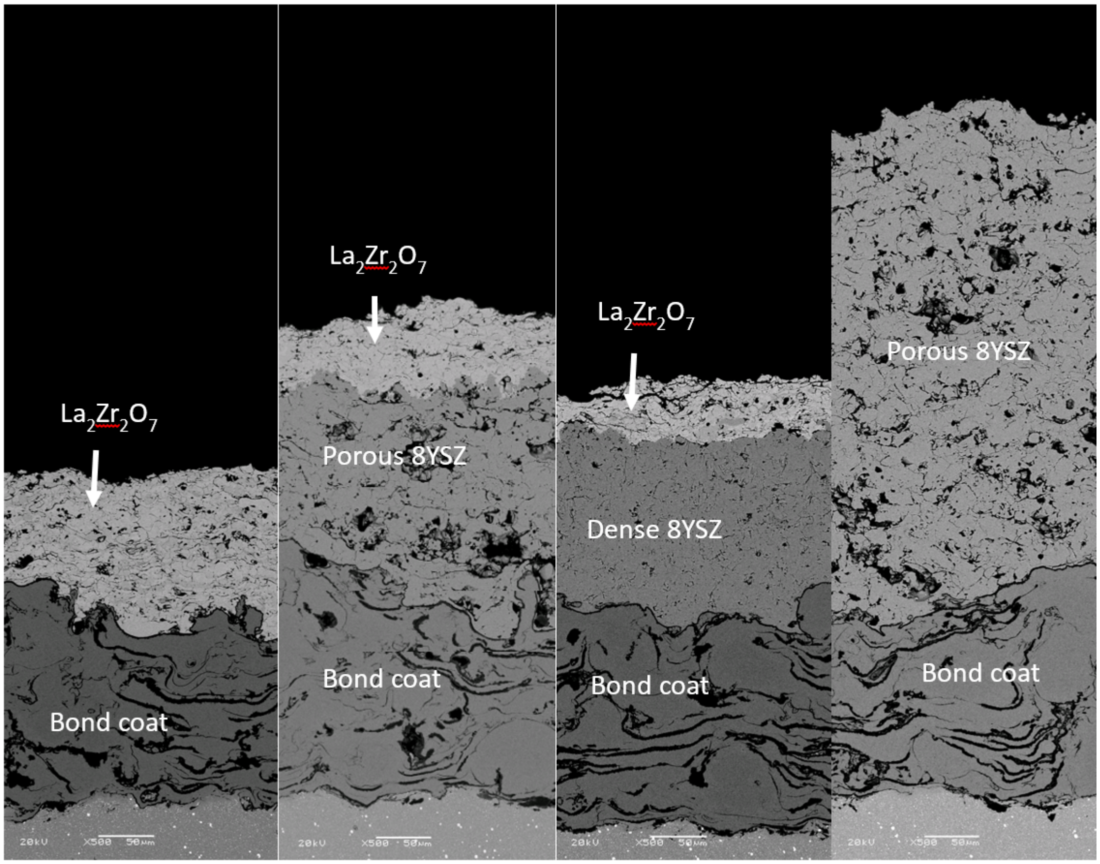

(a) Sample 6 (b) Sample 7 (c)Sample 8 (d)Sample 9

Figure 2.28. SEM images of the cross-sectional view of the TBC samples after furnace heat treatment: (a) fully delaminated SCL LZ coating, (b) edge delaninated DCL coating with porous 8YSZ and LZ, (c) fully delaminated DCL with dense 8YSZ and LZ, and (d) SCL porous 8YSZ coating.

the large residual stress in the thermally grown oxide through its roles in amplifying the imperfections near the interface [125].

2.3.4 Furnace cycling Test

The FCT experiments were conducted on sample 6, 7, 8 and 9 between high temperature 1366 K (1093 °C) and room temperature. In each cycle, samples were heated at 1366 K for 50 minutes and then cooled by compressed air for 10 minutes. It is recognized as a failure when more than 20 % surface area of top coat is delaminated.

All LZ coats layers were delaminated in the first 20 cycles in the FCT experiments. However, no significant delamination occurred in SCL porous 8YSZ coating after 2000 cycles. Because the coefficient of thermal expansion (CTE) of LZ (9–10$\times10^{-6}$ /K) is much lower than that of 8YSZ (10–11$\times10^{-6}$ /K), and bond coats have even higher CTE (about 15$\times10^{-6}$/K). The CTE difference between LZ and bond coat is larger than that between 8YSZ and bond coat, which leads to higher thermal stresses in LZ layers [40, 71]. In addition, the fracture toughness of LZ is about half of that of YSZ, as summarized in Table 1.1. The low fracture toughness means the resistance for the crack propagation in LZ material is very weak, so the crack is more easily to propagated in LZ than in YSZ. The failure mechanism for the LZ coating is associated with the large residual stress at the interface due to the large CTE difference and the low fracture toughness of LZ.

2.3.5 Jet Engine Thermal Shock Test

The JETS tests were conducted to investigate the thermal shock and thermal cycling performance. During JETS tests, the TBC samples were heated to 1505 K (1232 °C) at the center for 20 seconds, and then were cooled by compressed N2 gas for 20 seconds, followed by ambient cooling for 40 seconds. The heating and cooling cycles were repeated until the TBC samples failed. The failure criterion in the JETS tests was more than 20 % spallation of the TBC surface [69]. For each type of coats, at least 3 samples were tested in the JETS tests. Both the front and back side temperatures were measured during the test through two-color pyrometers to investigate the temperature gradient across sample thickness. The TBC samples were sectioned and polished according to the ASTM standard E1920-30 to examine their microstructures using a scanning electron microscope (SEM, JEOL Model JSM-5610, Japan).

The number of cycles-to-failure and final top coat status after the JETS tests are summarized in Table 2.4. During the JETS tests, the single-layer LZ coating was completely delaminated within 25 cycles, and the double-layer coating with the dense 8YSZ and the LZ was completely delaminated in about 885 cycles. Delamination happened near the interface between the dense 8YSZ layer and the LZ layer in the double-layer coating. However, the double-layer coating with the porous 8YSZ and LZ was only partially delaminated at edges after 2000 cycles and the cracked edge area took up about 20% of the total area of the top coat. In the remaining area, the top coat of LZ was still bonded with the porous 8YSZ layer. The double-layer coating with the porous 8YSZ and LZ had a better performance than other LZ-based coatings. The single-layer porous 8YSZ coating was intact after 2000 cycles.

Table 2.4. Summary of the number of cycles and final status in JETS tests.

	#6, SCL LZ	**#7, porous 8YSZ + LZ**	**#8, dense 8YSZ + LZ**	**#9, SCL porous 8YSZ**
Number of cycles before delamination	25	>2000	885	>2000
Failure status	Complete delaminated	Edge crack	Complete delaminated	Intact

The optical images of the TBC samples after the JETS tests are given in Figure 2.29. The single-layer LZ coating sample is shown in Figure 2.29(a), in which the LZ top coat was completely delaminated from the bond coat. Only the bond coat remained. The double-layer coating with the dense 8YSZ and LZ is shown in Figure 2.29(c). In this figure, the delaminated LZ coating fragments were laid on the top surface, although it already detached from the dense 8YSZ layer. The bright area is the dense 8YSZ layer, and the dark gray region is the LZ layer. After the JETS tests, only the dense 8YSZ layer was left on the substrate. The LZ top coat was totally lost during the JETS tests. Delamination occurred between the 8YSZ and LZ layers. The single-layer porous 8YSZ coating is shown in Figure 2.29(d). The 8YSZ top coat was almost intact after 2000 cycles, suggesting good thermal shock resistance. The three black marks on the edge of the samples in Figure 2.29(a) and Figure 2.29(d) were caused by sample holding clips. The double-layer coating with the porous 8YSZ and LZ is shown in Figure 2.29(b). The coating survived after the JETS tests with cracks on the edge of LZ top coat. The double-layer coating with the porous 8YSZ and LZ showed a considerably better performance than the single-layer LZ coating and the double-layer coating with the dense 8YSZ and LZ. Heating and cooling cycles led to the thermal residual stresses in TBC systems. The residual stress levels are proportional to the distance from the interface, as shown in Figure 2.31 [15]. For the double-layer coating with the porous 8YSZ and the LZ, the stress level at the interface between the 8YSZ and LZ layers was less than that at the interface between the 8YSZ and the bond coat.

The temperature differences between the front and back surfaces of the samples during the JETS tests are shown in Figure 2.30. Figure 2.30(a) shows the temperature difference in the cycle range from 0 to 2000, and Figure 2.30(b) is in the cycle range from 0 to 50. As shown in Figure 2.30(a), the curve of double-layer coating with the dense 8YSZ and LZ showed a sudden temperature change between 660 – 885 cycles, which is an evidence of delamination. However, the double-layer coating with the porous 8YSZ and LZ, including the single-layer porous 8YSZ coating, did not show a large temperature change, suggesting that the double-layer coating with the porous 8YSZ and LZ had a similar performance in the JETS tests as that of 8YSZ. However, the double-layer coating with the porous 8YSZ and LZ showed smaller temperature drops (56 K on average) than the single-layer 8YSZ coating, although thermal conductivity of the as-sprayed single-layer 8YSZ coating is higher than that of the single layer LZ coating. In the JETS tests, the temperature drops of the single-layer and double-layer coatings are not simply related to the thermal conductivities of

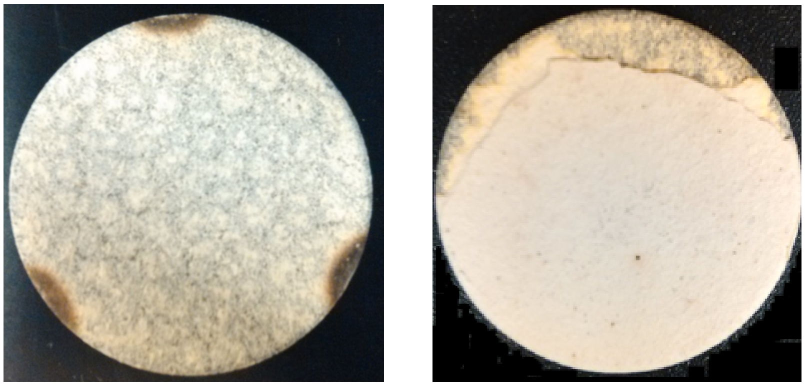

(a) Sample 6 (b) Sample 7

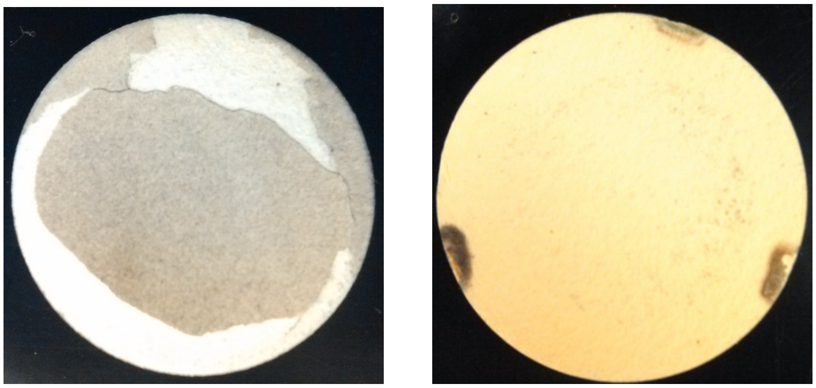

(c) Sample 8 (d) Sample 9

Figure 2.29. Optical images of the TBC samples after JETS tests.

as-sprayed coatings. The temperature drops of the single layer porous 8YSZ coating can be higher than those of the double-layer coatings with 8YSZ and LZ, due to the porosity difference, the interface roughness, sintering and thermal conductivity change in the JETS tests. In addition, the 8YSZ single layer coating was thicker than the double-layer coatings, so the temperature drops in the single layer 8YSZ coating can be larger than those of double-layer coatings.

As shown in Figure 2.30(b), the temperature differences of the single-layer LZ coating bumped up after 10 cycles and then dropped after 25 cycles. The gaps between the top and bond coats caused the increase of front-back surface temperature differences, indicating that the LZ top coat partially delaminated from the bond coat

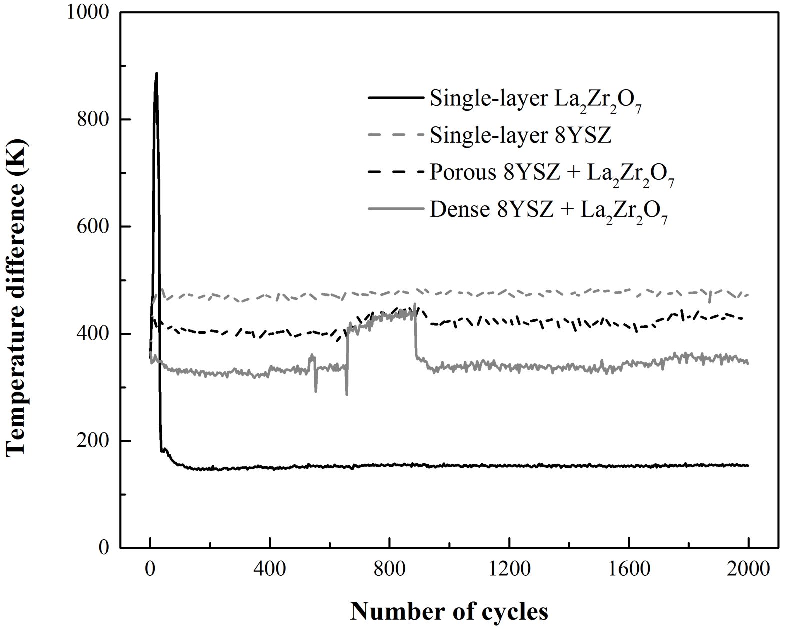

(a) Number of cycles from 0 to 2000

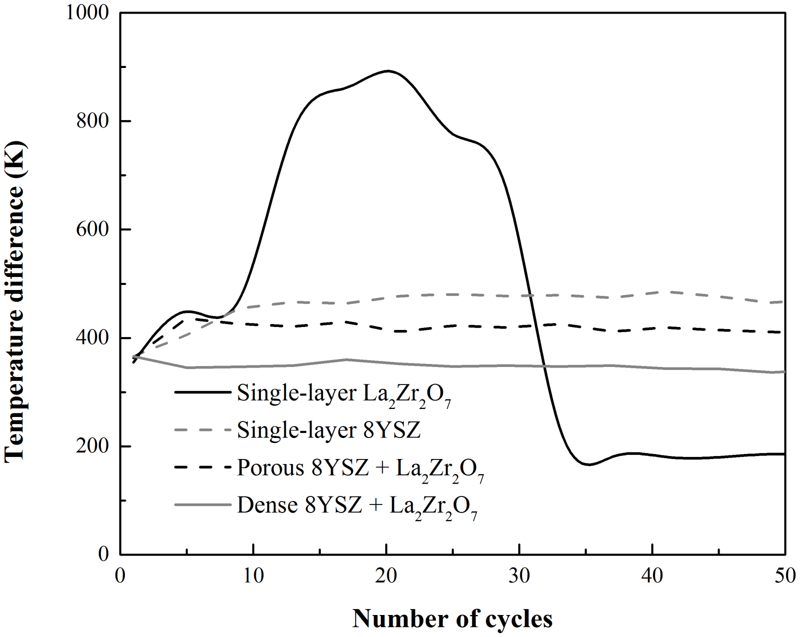

(b) Number of cycles from 0 to 50

Figure 2.30. Average temperature differences during JETS tests.

after 10 cycles. The top surface temperature of single-layer LZ coating reached to 2032 K (1759 °C) after 13 cycles due to accumulate of heat. As the top coat delaminated after 25 cycles, the bond coat and substrate were exposed to the JETS flame directly, causing a reduced temperature difference, as shown in Figure 2.30(b).

While the sprayed coating samples were heated and cooled in the thermal cycling test, thermal residual stress was generated in the TBCs layers due to the different CTE value between each layer. When the coating sample was heated, tensile stress was generated in the top and bond coat, and the compressive stress in the substrate. When the coatings were cooled from the high temperature, the compressive and shear stresses were generated in the top and bond coat, and the tensile stress in the substrate.

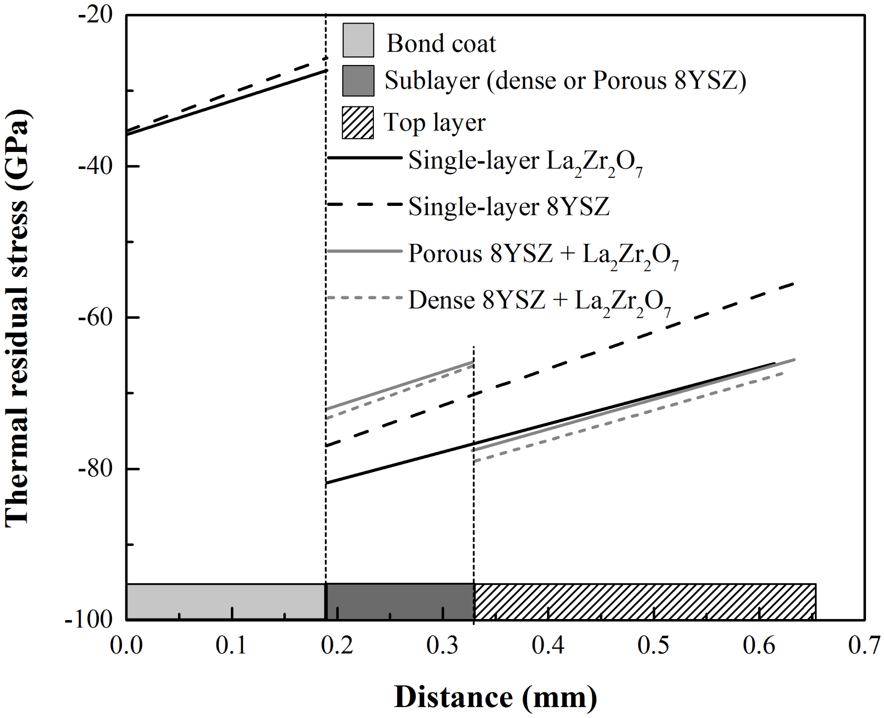

Figure 2.31. Calculated residual stress distributions as a function of thickness in four TBC samples.

The Equation (2.2)–Equation (2.7) were used to calculated the thermal residual stresses during the heating and cooling process. The residual stress distributions across the coating thickness of sample 6, 7, 8, and 9 are shown in Figure 2.31. The thermal residual stress difference at the interface between the top and bond coat of SCL LZ coat is larger than that of SCL porous 8YSZ coating. The stress differences at the interface between LZ and 8YSZ layers in DCL coatings were much smaller than that between the top coat and bond coat in the SCL LZ coating. Although the stress differences between the two DCL coatings were similar, the stress difference in sample 7 is smaller than that of sample 8. As a result, the SCL LZ coating was easily delaminated due to its larger residual stress and low fracture toughness, and sample 7 (porous 8YSZ + LZ) was survived due to its lowest residual stress at the interface and the stress accommodation characteristic from porous 8YSZ buffer layer.

2.3.6 Thermal Gradient Mechanical Fatigue Test

The thermal gradient mechanical fatigue (TGMF) tests combine the thermal exposure and mechanical loading test together, which introduce a thermal gradient over the tensile bar [126]. The experiments were conducted in argon atmosphere using tensile bar samples. A constant load of 150 N was added on the tensile bar during the thermal exposure. The samples were heated to 850 °C or 1100 °C for 10 minutes on the top coating side and kept at a constant temperature 350 °C on the back side, as shown in Figure 2.32 and Figure 2.33.

The thermal gradient was established during TGMF test across the TBC samples. After the heating process, the samples were cooled on front surface using a compressed air for 3 minutes and using ambient cooling for another 7 minutes. The thermal cycling experiments were repeated in this temperature control regime until the failure occurred. The failure criterion is the spallation for more than 20 % of the surface area.

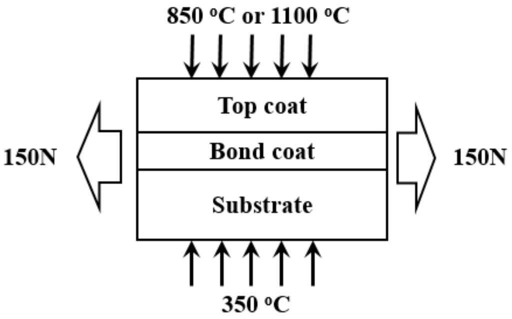

Figure 2.32. Schematic of TGMF test.

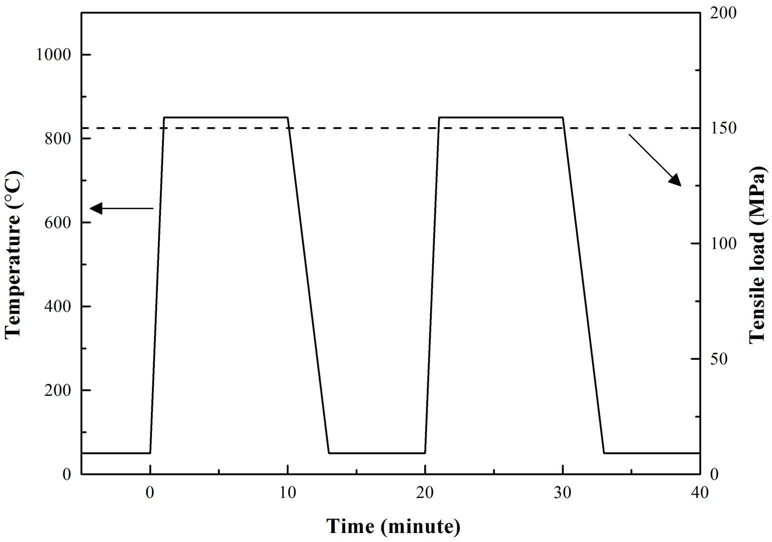

Figure 2.33. TGMF loading and heating and loading regime.

The TGMF tests in this work were categorized in two sets which were conducted in two different temperatures gradient environment. The first set of experiments heated 850 °C in the front side and kept 350 °C in back side; the second set heated the sample 1100 °C in front and kept 350 °C in back.

Figure 2.34 shows the optical images of the samples before and after the first set TGMF tests. As shown in Figure 2.34(e) and Figure 2.34(f), after 1200 cycles, there was no crack or spallation tendency in SCL porous 8YSZ coats. As shown in Figure 2.34(a) – Figure 2.34(d), the double layer LZ cannot last many cycles.

In Figure 2.34(a) and Figure 2.34(b), DCL porous 8YSZ and LZ coats (sample 7) delaminated on the edge after 220 TGMF cycles. In Figure 2.34(c) and Figure 2.34(d), DCL dense 8YSZ and LZ coats delaminated after 50 cycles.

(a) as-sprayed sample 7

(b) sample 7 after 220 cycles

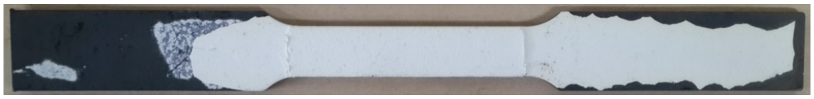

(c) as-sprayed sample 8

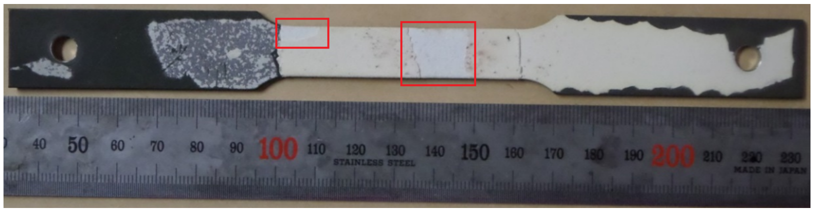

(d) sample 8 after 50 cycles

(e) as-sprayed sample 9

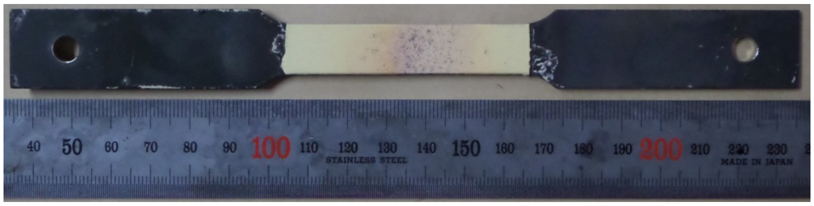

(f) sample 9 after 1200 cycles

Figure 2.34. Photograph of samples before and after the first set of TGMF test.

The optical images of the second set of TGMF test samples were shown in Figure 2.35. As shown in Figure 2.35(b), both 8YSZ and LZ layer were partly delaminated near the center of the tensile bar after 38 TGMF cycles. Part of the bond coat was exposed due to the delamination. Figure 2.35(d) shows only the top LZ layer was delaminated after 49 TGMF cycles. Comparing with the first set TGMF tests, both sample 3 and sample 4 have shorter lifecycles in the second set TGMF tests. DCL porous 8YSZ + LZ has better performance in lower temperature gradient (the first set TGFM tests) and became worse in higher temperature gradient (the second set TGFM tests).

(a) as-sprayed sample 7

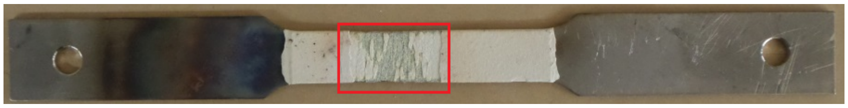

(b) sample 7 after 38 cycles

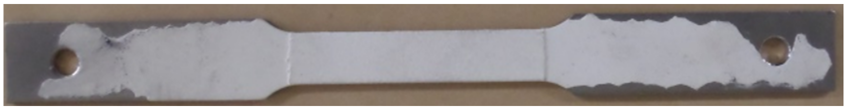

(c) as-sprayed sample 8

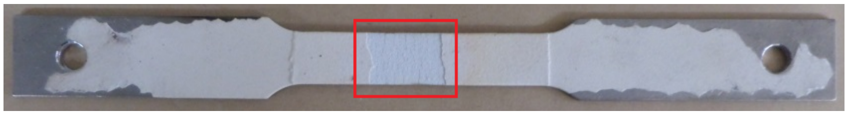

(d) sample 8 after 49 cycles

Figure 2.35. Photograph of samples before and after the second set of TGMF tests.

Typically, the spallation process began at edges between LZ coats and 8YSZ coats sublayer. In this TGMF experiments, all the spallation occurred near the interface of the LZ layer and 8YSZ layers, which is just underneath the LZ top coats. The first stage of the spallation process was the buckling of the LZ top coats layer, following the occurrence of cracks in the interface. The second stage was the propagation of cracks in the interface, which followed by the spallation of top coat. Finally, the LZ top coat was peeled off [127].

Because the coefficients of thermal expansion (CTE) in 8YSZ (11×10^{-6} K^{-1} at 1000 °C) are large than LZ (9×10^{-6} $K^{-}1$ at 1000 °C) [59,71], so the volume difference is very large between 8YSZ and LZ layers. Due to the mismatch of volume change, thermal residual stress was induced in the thermal cycles. The thermal residual stress in the interface was accumulated during this TGMF cycles. When the accumulated residual stress became larger than the critical yield stress of the LZ material, crack and spallation occurred. Besides, the fracture toughness of LZ is lower than 8YSZ [15,50], so DCL 8YSZ and LZ coats tend to delaminate first at LZ layers near the interface.

2.4 Thermal and Mechanical Stability of Composite LZ/8YSZ Coatings

2.4.1 Architecture of the LZ/8YSZ Composite Coating

Currently, the biggest challenge of LZ for the TBC application is the relative shorter thermal cycling lifetime than the traditional 8YSZ coating due to LZ's lower CTE and fracture toughness than 8YSZ. In this work, a new LZ/8YSZ composite coating material is designed, which is aimed to improve the toughness and CTE of the top coatings. Buffer layer is also introduced into this architecture to further reduce the residual thermal stress at the interface between the top and the bond coat. The architecture, composition, and thickness of the LZ/8YSZ composite coating sample are listed in Table 2.5. Sample 10 and 12 are SCL coatings that do not have buffer layer. Sample 11 is a double layer TBC that contains an 8YSZ buffer layer and a 50 % LZ/50 % 8YSZ composite coat. Sample 13 has an 8YSZ buffer layer and two composite top coats, which are a 25 % LZ/75 % 8YSZ composite coating on the bottom and a 50 % LZ/50 % 8YSZ composite coat on the top. All of these composite coating samples are deposited using APS technique on the Ni-based superalloy substrates (Nimonic 263, ThyssenKrupp VDM, Germany, composition:

Ni-20Cr-20Co-5.9Mo-0.5Al-2.1Ti-0.4Mn-0.3Si-0.06C, in wt.%) with an AMDRY 962 bond coat (Sulzer Metco Holding AG, Switzerland, composition: Ni-22Cr-10Al-1.0Y in wt.%). The same LZ and 8YSZ powders are used in the deposition process as the previous sections [128].

Table 2.5. List of the LZ/8YSZ composite coating sample.

Sample number	**Buffer layer composition**	**Buffer thickness (μm)**	**Top coat composition**	**Top coat thickness** (μm)
10	No buffer layer	–	50% LZ/50% 8YSZ	430
11	Porous 8YSZ	60	50% LZ/50% 8YSZ	370
12	No buffer layer	–	25% LZ/75% 8YSZ	430
13	Porous 8YSZ	60	25% LZ/75% YSZ + 50% LZ/50% YSZ (top)	60 + 310 (top)

The cross-sectional microstructure SEM images of the as-sprayed composite TBC samples are shown in Figure 2.36. The bond coat and buffer layers show a typical microstructure of APS deposited coating. The two component materials LZ (white color) and 8YSZ (gray color) are glued together as a layered ''splats" form in the top coat, which leaves some micro-cracks and pores in the coating. There is no delamination in the as-sprayed top coat and buffer layer, suggesting the initial deposition has a high quality. All the surface and interfaces show an irregular roughness, and no TGO layer is observed at the interface between the top coat (or buffer layer) and the bond coat [128].

2.4.2 Thermal Cycling Test of the LZ/8YSZ Composite Coating

Both the FCT and the JETS test were performed in the composite coating samples. In the FCT test, the round button samples were heated at a surface temperature

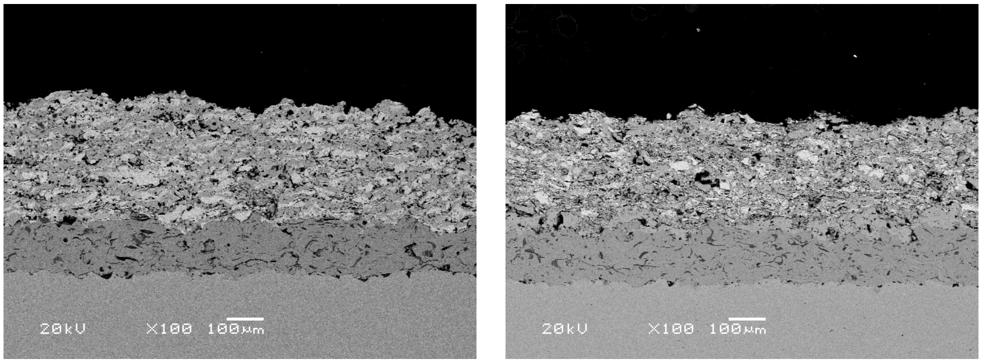

(a) Sample 10 (b) Sample 11

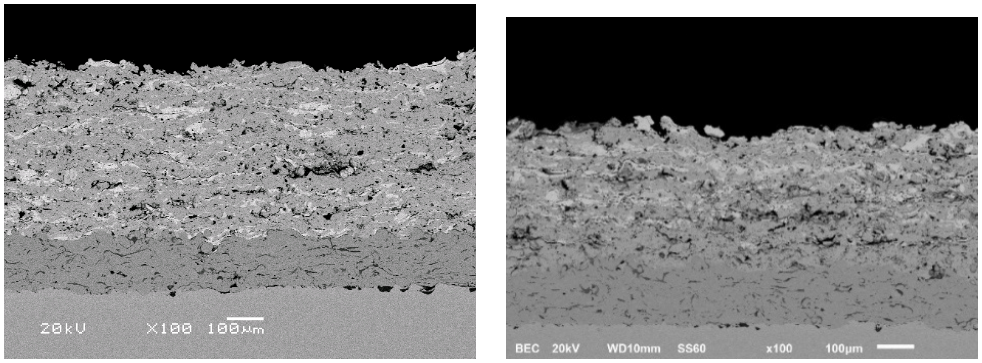

(c) Sample 12 (d) Sample 13

Figure 2.36. SEM microstructure images of composite coatings.

of 1100 °C (1373 K) for 40 min and then cooled with natural air at room temperature for 20 min. In the JETS test, the same equipment and heating/cooling regime were applied as the layered coating (see section 2.3.2), except the surface heating temperature is 1400 °C, which is higher than that used for the layered coating. The failure criterion for both FCT and JETS tests are defined as 20 % top coat delamination.

The equivalent operating hours (EOH) is an analytical parameter that widely used to estimate the TBC lifetime during the operation of the gas turbine engine, which can be expressed as the following equations.

$$EOH = AOH + 20(\sum S_i + \sum LR_i + \sum T_i + \sum LC_i) \times F \tag{2.10}$$

where AOH, $\sum S_i$, $\sum LR_i$, $\sum T_i$, $\sum LC_i$ and F correspond to actual operating hours, the coefficient of correction, load rejection, trip, rapid load change, and fuel factor, respectively. In this study, the EOH is approximated by multiplying 21 to the member of FCT cycles [128, 129].

Table 2.6. Thermal cycling results of composite TBC samples.

Sample #	**FCT test/Status**	**JETS test/Status**
10	540 cycles (11,340 EOH) Fully delaminated	70 cycles Fully delaminated
11	768 cycles (16,128 EOH) Fully delaminated	2000 cycles Intact
12	936 cycles (19,656 EOH) Fully delaminated	1022 cycle Fully delaminated
13	1143 cycles (24,000 EOH) Intact	2000 cycles Intact

The results of the FCT test and the JETS test are summarized in Table 2.6. The FCT tests are conducted for each sample to an equivalent thermal durability of 24000 EOH, which is equal to 1143 cycles. The JETS tests are aimed to perform for 2000 cycles to compare with the state-of-the-art 8YSZ coating shown in Table 2.4 (see section 2.3.2). Comparing to the layered LZ-based TBC, all the composite LZ/8YSZ coatings have better performance in FCT tests. Sample 10, which is a single layer coating with the composition of LZ/8YSZ in a 50%: 50% volume ratio, delaminated after 540 cycles in the FCT test and 70 cycles in the JETS test, showing very poor thermal stability. Sample 12 which is a single layer coating with the composition of LZ/8YSZ in a 25%: 75% volume ratio, delaminated in 936 cycles in the FCT test and 1022 cycles in the FCT test, showing a better performance than sample 10. The comparison between sample 10 and sample 12 indicates that the thermal durability can be improved by controlling the composition ratio of the composite coating. Although the sample 11, which have single 8YSZ buffer layer, shares the same top coat with sample 10, it shows a better performance in the JETS test and the FCT test than sample 10. The comparison between sample 10 and sample 11 indicates that the thermal durability can be effectively improved by introducing a buffer layer. Sample 13 has two composite coat layers and an 8YSZ buffer layer. Sample 13 shows the best performance in the FCT test and the JETS test, which is the only TBC survives in both tests without spallation, suggesting that the combination of the buffer layer and the gradient LZ/8YSZ composite coat is an effective way to improve the thermal durability performance.

The cross-sectional SEM microstructure images of all samples after the FCT test and the JETS test are shown in Figure 2.37 and Figure 2.38. As shown in Figure 2.37 and Figure 2.38, all delaminations occur near the interface between the top (the LZ/8YSZ composite layer and the buffer layer) and bond coat. During the FCT test the TGO layer (α-Al_2O_3 in black color) is observed at the interface between the top coat and bond coat. The TGO layer at the interface becomes fragile part and results to delamination if TGO thickness grows greater than 10 μm. However, the TGO layers in these composite samples are far less than 10 μm, which can not be the primary reason to the delamination of the top coat. In Figure 2.37(d) and Figure 2.38(b), the sample 11 and sample 13 have vertical cracks in top coat after the JETS test, which provide the strength compliance during the thermal cycling test and improve the thermal durability [106].

Figure 2.39 summarizes the results of the FCT test and the JETS test for both layered and composite LZ/8YSZ samples (from samples 6 to sample 13). As shown in Figure 2.39, the FCT performances of the composite LZ/8YSZ coatings (sample 10 - 13) have a great improvement. The JETS test results of the coating with buffer layer (multiple layer coatings, sample 7, 8, 11 and 13) have better performance than the SCL LZ-based TBC. Sample 9 (SCL 8YSZ TBC) is the standard reference sample. Comparing to other LZ-based TBC samples, sample 13 exhibits the most outstanding thermal durability performance. The improvement of the thermal durability primarily is primarily due to the reduce of the CTE mismatch at the interface by the relatively

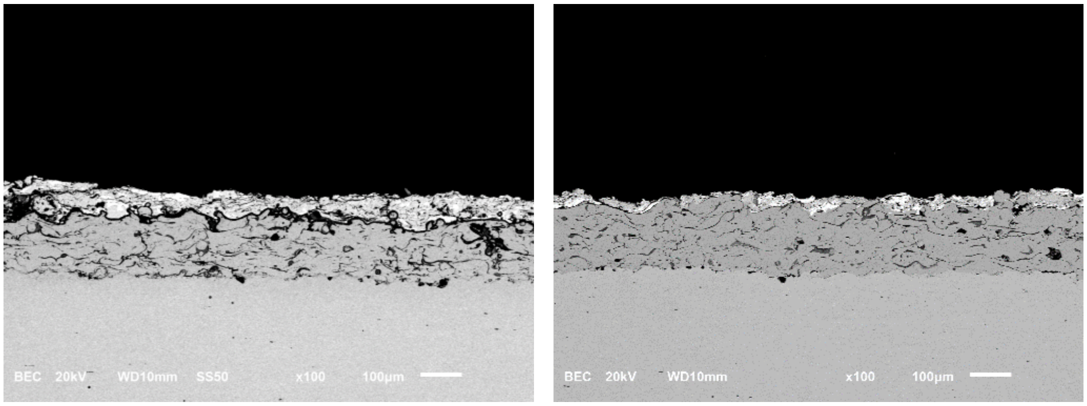

(a) sample 10 after FCT test (b) sample 10 after JETS test

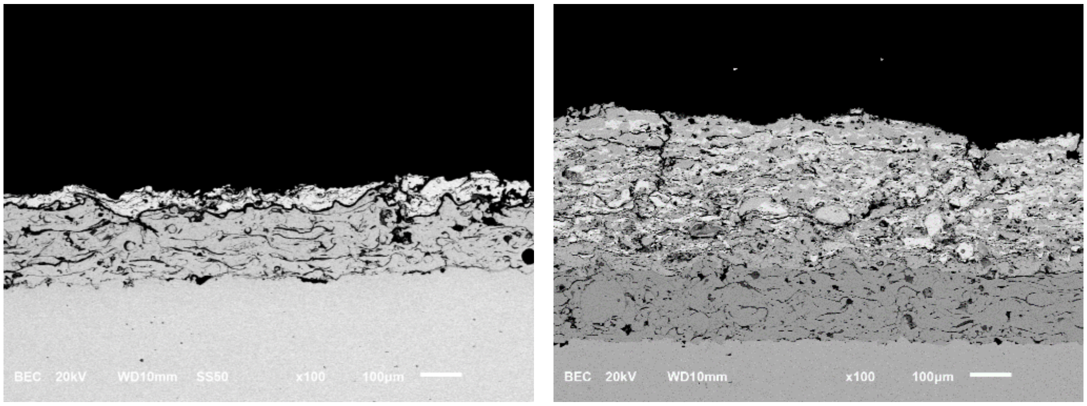

(c) sample 11 after FCT test (d) sample 11 after JETS test

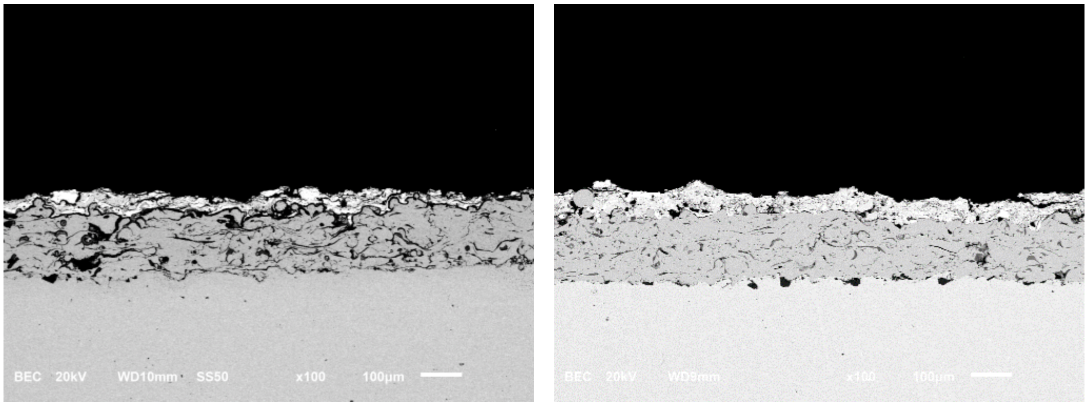

(e) sample 12 after FCT test (f) sample 12 after JETS test

Figure 2.37. SEM microstructure images of composite coatings after the FCT and the JETS tests.

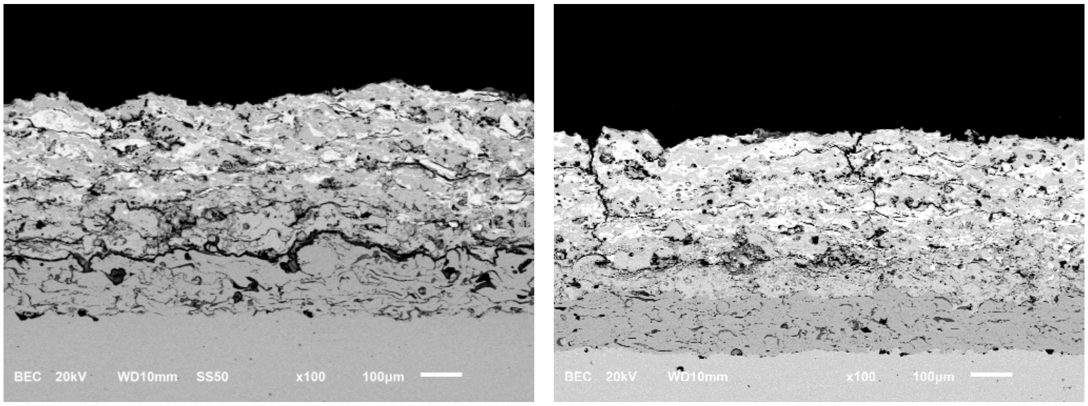

(a) sample 13 after FCT test

(b) sample 13 after JETS test

Figure 2.38. SEM microstructure images of sample 13 after the FCT and the JETS tests.

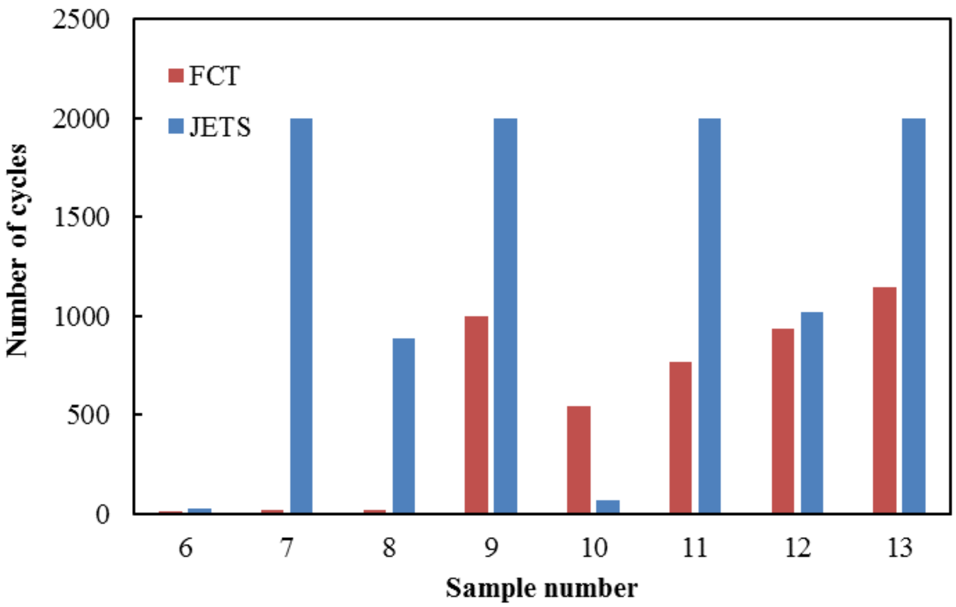

Figure 2.39. Powder size analysis results.

continuous composition variation, and the increase of the fracture toughness in the LZ coating by adding 8YSZ, which has a high fracture toughness. In addition, the double layer gradient composite LZ/8YSZ coating with the buffer layers can accommodate the thermal residual stress, so the stress is dissipated in the composite top coat and its buffer layers.

2.5 Summary

The SCL, DCL and composite LZ-based TBC samples are successfully deposited using APS technique. The microstructures confirm that the porosities increase as the standoff distance between the APS torch and the substrate increases. The intrinsic defects including pores, splat boundaries, and cracks are not uniformly dispersed in the LZ and the 8YSZ top coat. This chapter systematically discusses the physical, mechanical, thermal properties of LZ-based coatings, and analyzes the thermomechanical durability of LZ-based layered and composite TBCs. The main conclusions of this chapter are summarized in following aspects.

1. The Young's modulus and the nanoindentation hardness results show that as the porosity increases, the pores become larger and the "splat" boundaries become thicker, so that the corresponding hardness and Young's modulus show a decreasing trend. The hardness and Young's modulus results can be fitted into a linear equation.

2. The SCL LZ sample have lower adhesion strength than the SCL 8YSZ sample. Since the microstructure of the LZ grains have net-shape boundaries, which leads to the generation and propagation of the cracks. The 8YSZ material has higher fracture toughness and hardness than the LZ, which leads to a higher adhesion bond strength in the 8YSZ coatings. In addition, the LZ coating has a larger thermal residual stress difference at the interface than the 8YSZ coating. The thermal residual stress induces more grain boundary and pores inside the ceramic layer, where the crack occurs.

3. The Single and double layer LZ TBC samples have higher erosion rate than 8YSZ coats because the fracture toughness of LZ is lower than that of 8YSZ, and the critical erosion velocity of LZ is much lower than that of 8YSZ. However, the DCL dense 8YSZ + LZ TBC sample has lower erosion rate than other SCL and DCL

LZ-based TBC samples, because the DCL dense 8YSZ + LZ TBC sample has higher critical erosion velocity in its top coat.

4. The measured average thermal conductivity of SCL LZ coating is 0.59 – 0.68 W/m/K in the temperature range of 297 – 1172 K (24 – 899 °C), which is ∼25% lower than that of SCL porous 8YSZ coating in the same temperature range.

5. The CTE values of LZ coating are approximately 9-10$\times 10^{-6}$ K^{-1} in the temperature ranges of 400 – 1600 K (127 – 1327 °C). However, the CTE values of LZ are about 10 % lower than those of 8YSZ in the same temperature range. The large CTE difference between the LZ coating and bond coat might lead to large thermal residual stress, which is one of the main reasons for the failure of the SCL LZ coating in mechanical and thermal durability tests.

6. Both the furnace heat treatment and the JETS tests show that the layered DCL porous 8YSZ + LZ coating have a better thermal durability performances than the SCL LZ coating and the DCL dense 8YSZ + LZ coating. The result indicates that the porous 8YSZ can be used as a buffer layer for LZ-based TBC systems to improve the durability during service. However, all the LZ-based layered coatings are delaminated in the FCT tests. The delamination of the LZ-based coating in FCT and JETS test are related to the high thermal residual stress that induced by the large CTE difference and the low fracture toughness of the LZ material.

7. All the LZ-based coatings have shorter lifetime than the SCL 8YSZ coatings in the TGMF experiments. The primary reason for the spallation of the LZ coating is due to its low fracture toughness. In addition, the large CTE difference between the 8YSZ layer and the LZ layer leads to high thermal residual stress. The residual stress accumulates during the thermal cycling test, until it reaches the ultimate strength of the LZ coating. Then, the crack is initiated near the interface of 8YSZ and LZ layer.

8. Since the layered LZ-based TBCs have limited thermal durability performance, the LZ/YSZ composite coatings are proposed and deposited in four architectures. The triple layer composite TBC sample (sample 13, the gradient 50 % LZ/50 % 8YSZ + 25% LZ/75% 8YSZ top layer with the 8YSZ buffer layer) exhibits the best

thermal durability performance in both the FCT test and the JETS test. This is primarily because the composite LZ/YSZ coating reduce the CTE difference at the interface, and the fracture toughness is increased in the LZ top coat by adding the 8YSZ powder.

CHAPTER 3. MECHANICAL PROPERTIES MODELING OF LZ

3.1 Motivation and Introduction

Although the low thermal conductivity of LZ is an advantage for the application of TBC, the LZ is also reported to have lower Young's modulus, hardness, and fracture toughness than the 8YSZ [15]. As discussed in chapter 2, the thermal cycling performance of the SCL LZ TBC is worse than that of the 8YSZ, which might due to the high thermal residual stress and the poor mechanical properties of the LZ [54, 71]. As a result, the investigation of the mechanical properties of LZ would be very important for systematically understanding the LZ materials. The Tensile and shear stress-strain relations of the single crystal LZ exhibit anisotropic characteristic. However, single crystal LZ samples are hard to be prepared. Since it is hard to measure the intrinsic mechanical properties of the single crystal LZ in experiment due to its porous character, theoretical modeling techniques are used to study these mechanical properties.

The most widely used theoretical method to investigate the mechanical properties is an analytical method based on Voigt-Reuss-Hill's theories, which calculates the elastic moduli from the elastic constants [130–132]. The elastic constants can be computed using the first principles calculation based on density functional theory (DFT) [77, 78]. In addition, the nanoscale tensile and shear simulations can be conducted using DFT and MD calculations directly. The uniaxial nanoscale-tensile strain can be applied stepwise in the tensile direction. The shear strain can be applied stepwise by changing the crystal angle. After the full relaxation at each strain stage, the tensile and shear stresses can be computed using the DFT or the MD calculations.

Although several methods were developed to conduct the nanoscale tensile and shear simulation, to our best knowledge, no such investigation was performed on LZ material. In this work, the single LZ crystal model is built and the lattice parameter of LZ conventional unit cell is calculated by minimizing the total system energy. The nanoscale tensile and shear stress-strain relations of single crystal LZ are investigated using DFT and MD method. The corresponding elastic moduli are calculated using two approaches: stress-strain curve analysis in large deformation and the elastic constant analysis in small deformation [130, 133]. The Toughness of the single crystal LZ is calculated based on the stress and strain curves as well. Average Bader charge difference and charge density distribution are used to explain the influence of election interaction on Young's modulus.

3.2 Theoretical LZ Model

3.2.1 DFT Model

In this work, the DFT calculations were conducted using Vienna Ab initio Simulation Package (VASP) [87, 88]. The exchange-correlation potential was specified using projector augmented wave (PAW) method of generalized gradient approximation (GGA) functional. The Brillouin zone k-point was conducted using 3×3×3 Monkhost-Pack scheme. A conjugate-gradient algorithm was used for the ironic relaxation. The plan-wave cutoff energy was 500 eV. The energy relaxation criterion for the electron was 10^{-6} eV and the ionic relaxation convergence criterion was that the total force was smaller than 0.01 eV/A.

The LZ crystal is a cubic pyrochlore structure, which is belong to space group of $Fd3\bar{m}$ [26]. There are four independent crystallographic atom sites, where La is at 16d at (1/2, 1/2, 1/2) , Zr is at 16c at (0,0,0), O1 is at 48f at (x, 1/8, 1/8) and O2 is at 8b position of (3/8, 3/8, 3/8). The x value of O1 varies from 0.3125 to 0.375. According to Tabira's experiments, 0.333 is chosen as the initial x value of the LZ crystal in this work [28]. The conventional LZ unit cell is used in the elastic constant calculation and the shear stress-strain calculations, as shown in Figure 3.1.

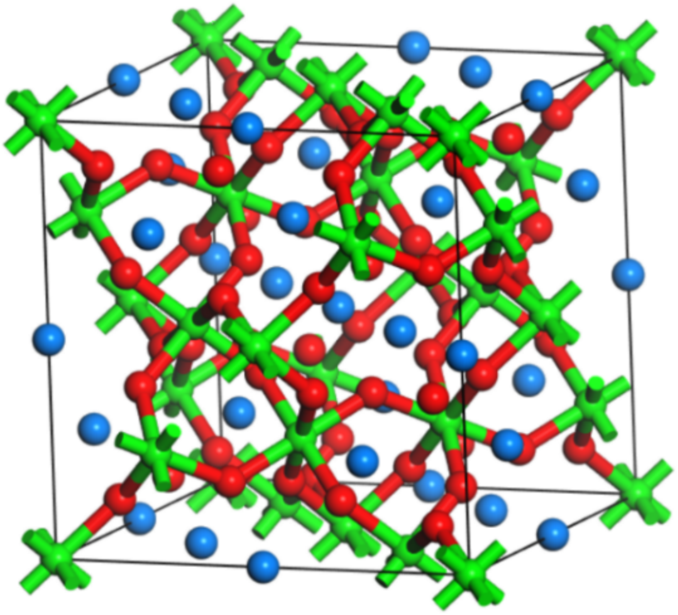

Figure 3.1. Crystal structure of LZ unit cell. Each ball shown as green, red, and blue indicates Zr atom, O atom and La atom, respectively (same coloring schemes are used in all figures afterwards).

To calculate the stress in a specific crystal direction, the LZ unit cell was rebuilt to align the (001), (011) and (111) surface perpendicular to the tensile axis for the tensile stress-strain calculations, as shown in Figure 3.2. The atom numbers of the (001), (011) and (111) model are 44, 44, 66 respectively. All of the LZ structures were relaxed before the elastic constant, tensile and shear calculations.

Large deformation stress-strain analysis and the small deformation elastic constant analysis were used to calculate the anisotropic elastic moduli. In the stress-strain analysis, the anisotropic Young's modulus and shear modulus in a particular tensile and shear direction were obtained from the slope of the linear fitted line in the elastic stage of the stress-strain curves. In the small deformation elastic constant analysis, Voigt-Reuss-Hill approximation was used to calculate the elastic moduli of LZ base on the elastic constants of single LZ unit cell. The elastic constants of LZ unit cell were calculated using DFT method by performing finite distortion of the LZ unit cell [134]. The Voigt proposed approach expresses the stress in a single crystal in terms of the

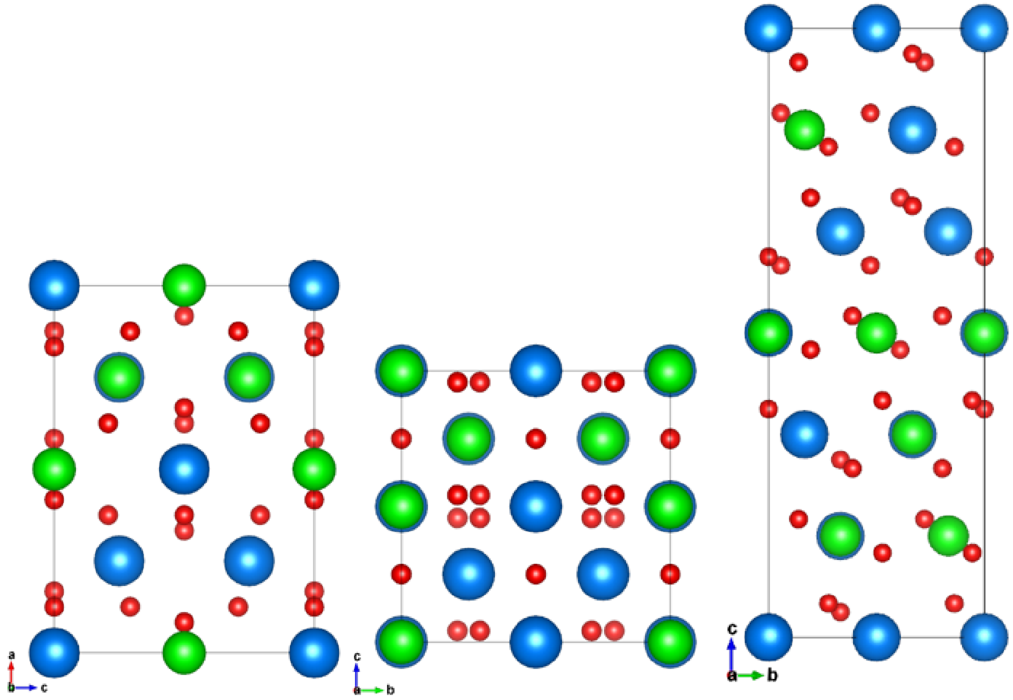

(a) (b) (c)

Figure 3.2. Tensile model at (a) [001] direction along a axis, (b) [011] direction along c axis, and (c) [111] direction along c axis directions. Each ball shown as green, red, and blue indicates Zr atom, O atom and La atom, respectively.

given strain. On the other hand, the Reuss proposed approach expresses the strain in terms of the giving stress. The Voigt-Reuss-Hill approximation calculated the effective moduli of an aggregated polycrystalline combined the Voigt and Reuss's approximation [130, 135]. For cubic single crystal LZ, only 3 elastic constants are independent (C_{11}, C_{12}, C_{44}). The effective bulk modulus (K), shear modulus (G), Young's modulus (E) and Poisson's ratio (υ) of cubic LZ crystal can be calculated using following equations:

$$K = \frac{C_{11} + 2C_{22}}{3} \tag{3.1}$$

$$G = \frac{G_V + G_R}{2} \tag{3.2}$$

$$E = \frac{9KG}{3K+G} \tag{3.3}$$

$$\upsilon = \frac{3K-2G}{2(3K+G)} \tag{3.4}$$

where G_V and G_R are the shear modulus expressed by the Voigt and Reuss approach, respectively [130, 135].

$$G_v = \frac{(C_{11} - C22) + 3C_{44}}{5} \tag{3.5}$$

$$\frac{5}{G_R} = \frac{4}{C_{11} - C_{22}} + \frac{3}{C_{44}} \tag{3.6}$$

The slip system (easy slip plane and direction) in the shearing process often locates on the plane of high atomic density in closely packed directions [136]. For example, the primary slip system for face center cubic (fcc) crystal is {111}<110> and the secondary slip direction is {111}<11$\bar{2}$>. Because the {111} is the closest packed plane in LZ crystal, the most possible slip directions are along {111}<110> and {111}<11$\bar{2}$> directions. The conventional unit cell of LZ is used in the shear stress calculation, as shown in Figure 3.1. The shear direction is controlled by rotating the LZ unit cell to align the slip plane perpendicular to one of the coordination axes. The shear strain is applied by changing the angle in the shear directions. The shear stress is calculated using first principles calculations corresponding to each strain step.

Bader charge transfer analysis in tensile and shear DFT model is conducted to describe the electron gain and loss between different atoms [137, 138]. The average charge differences between Zr, La and O are calculated from the Bader charge results, which give the insights of atom bonding characteristics in different orientations.

3.2.2 MD Model

However, all of the DFT calculations for tensile and shear are performed on the ground state of atoms, which is typically at the temperature of 0 K. The tensile and shear simulations at a higher temperature can be conducted using molecular dynamics (MD) calculation, and MD also can be performed at a larger scale than the first principles calculations. All of the MD calculations in this study are conducted using LAMMPS (Large-scale Atomic Molecular Massively Parallel Simulator) MD simulation package [139]. In this work, the interactions between atoms are assumed to be purely ionic, so the Buckingham and the Coulomb potentials are applied to describe the short and long range atom interactions, respectively, which can be expressed as follows:

$$U_{ij}(r_{ij}) = A_{ij}exp(\frac{-r_{ij}}{\rho_{ij}}) - \frac{C_{ij}}{r_{ij}^6} + \frac{1}{4\pi\epsilon_0} \cdot \frac{q_i q_j e^2}{r_{ij}} \tag{3.7}$$

where r_{ij} is the distance of the interactive ions, q_i and q_j are the charges of La^{3+}, Zr^{4+}, O^{2-} ions, ρ is an ionic pair dependent length parameter, and A and C are adjustable parameters. The parameters of the Buckingham potential used in this study are listed in Table 3.1, which are fitted based on experimental crystallographic data and Hartree-Fock calculated elastic constants by Crocombette et al. [140]. Both the tensile and the shear MD simulations in this work were conducted in 300 K. The tensile simulations were carried out using an uniaxial elongation regime along the x-axis, and the shear simulations were performed using an uniaxial compression regime. The periodical boundary condition was used in all these MD simulations. The LZ unit cells model used in the first principles calculations, as shown in Figure 3.2, were applied to assemble the MD tensile and shear models. For tensile MD calculation, three tetragonal prisms with 12×12×24 (individually in x, y, z directions) LZ unit cells in [001], [110] and [111] directions were assembled as tensile models in each direction. The MD models of tensile simulation in [001] direction is shown in Figure 3.9(a). In the tensile model, the (001), (110) and (111) surfaces are perpendicular to the tensile axis (z). The shear models were built with 16×16×16 LZ unit cells in $[11\bar{2}]$ direction and 24×36×16 LZ unit cell in [110] direction. The compression axis was aligned along [110] and $[11\bar{2}]$ directions. The conjugate gradient method was used to minimize the energy of the system in both tensile and shear simulations [141]. Then, the time integration was performed in isothermal-isobaric (NPT) ensembles, which was dedicated to generate the position and velocity parameters. Finally, the tensile models were elongated in the NPT ensembles, and the shear models were compressed in the canonical (NVT) ensembles. The time step of all the MD simulations are at 1 femtosecond.

Table 3.1. Buckingham potential parameters for LZ [140].

Interactions	**A** (eV)	**P (Å)**	**C** (eV·**Å**^{6})	**Charge**
O-O	22764.00	0.1490	27.89	-2.0
La-O	1367.41	0.3591	0.00	-3.0
Zr-O	1478.69	0.3554	0.00	+4.0

3.3 LZ Crystal Constant Optimization

The crystal constant (geometry optimization) is calculated by minimization of the total system energy. The interatomic potential energy is the sum of the repulsive energy and attractive energy. The potential energy (E) as a function of interatomic distance (r) is shown in Figure 3.3 [142]. In a two atoms system, when r is smaller than the equilibrium distance r_0, the r decreases as the repulsive energy increases and attractive energy decreases, which results to a repulsive force on the atoms. Therefore, the atom pair will be pushed away. On the other hand, when r becomes larger than r_0, the attractive energy takes advantage to pull the atoms together. When the equilibrium distance r_0 between the two atoms is reached, the total energy reaches its lowest value. In a crystal system, the crystal constant that has the minimum total energy can be regarded as the equilibrium state of the system, which means the system has the highest possibility to balance the repulsive and the attractive forces among all atoms. As a result, the lattice constants can be obtained by analysis relations between the total energy and the lattice contents.

Since LZ is a cubic crystal, it has only one lattice constant. The actual LZ lattice constant was determined by finding the minimum point on the curve of the total energy as a function of lattice constant. Figure 3.4 shows the DFT-calculated total

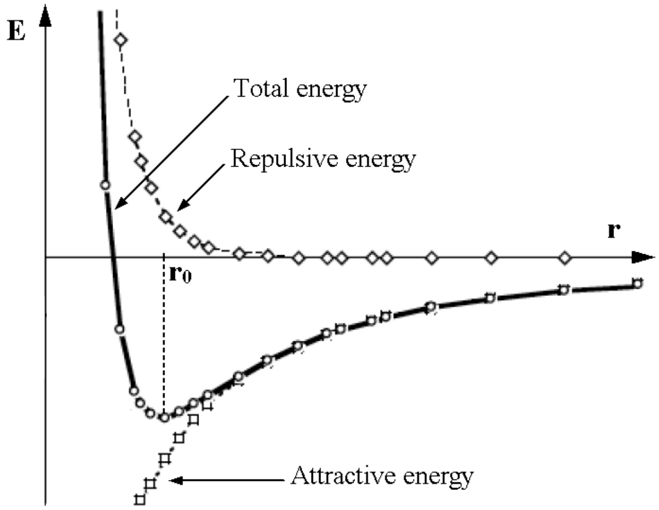

Figure 3.3. Potential energy as a function of interatomic distance.

energy of single LZ conventional cell as a function of lattice constant. This work tries the lattice constant of LZ model from 9 Å to 12 Å, which has a wide enough range to cover the actual LZ lattice constant. The calculation results indicate that the equilibrium state of the system occurs at the lattice constant of 10.875 Å, where the total energy reached its minimum point of -803.749 eV.

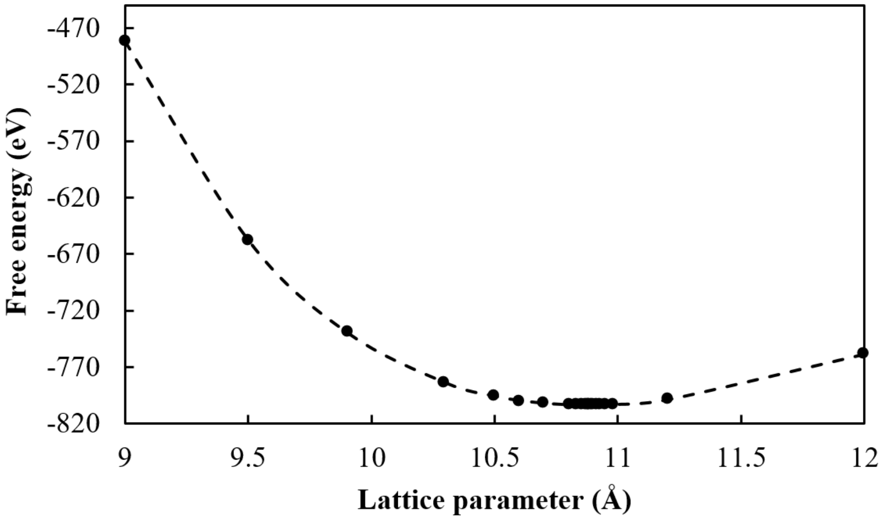

Figure 3.4. Total energy as a function of LZ lattice constant.

To validate the DFT-calculated results, the lattice constant of LZ powders was analytically calculated from XRD experimental data, as shown in Figure 2.2 (section 2.1.2 LZ Powder characterizations). Bragg's Law was used to analyze the XRD data:

$$n\lambda = 2dsin\theta \tag{3.8}$$

where $\lambda = 1.54$ Å (for the laboratory XRD used in this work), and n = 1. The lattice parameters can be derived from d and Miller indices <h k l> of each XRD peak. specifically, for cubic unit cell, the lattice parameter (a_0) can be expressed by:

$$d_{hkl} = \frac{a_0}{s}, \qquad wheres = \sqrt{h^2 + k^2 + l^2} \tag{3.9}$$

Table 3.2 shows the calculated lattice constant from several XRD peaks experiential data. The average lattice constant of LZ powders obtained from XRD experimental data is 10.801 Å.

Table 3.2. Analytically calculated lattice constant from XRD peaks.

XRD Peak	**(2 2 2)**	**(4 0 0)**	**(4 4 0)**	(6 2 2)	(4 4 4)	(8 0 0)
Lattice constant (Å)	10.814	10.799	10.802	10.798	10.786	10.804

Shimamura and Tabira's experiment results of the LZ lattice constant are 10.8 Å and 10.802 Å, respectively, which are the same as the XRD experimental results in this work [23, 28]. The difference between the DFT-calculated result and the XRD experiments result is 0.68 %. The DFT-calculated lattice constant of LZ is very accurate.

3.4 Stress-Strain Analysis and Anisotropic Elastic Moduli

3.4.1 Large Deformation Stress-Strain Analysis

As mentioned in section 3.2, the single LZ cell nanoscale models used for the DFT tensile and shear simulations are (001), (110), (111) and conventional LZ cell, respec-

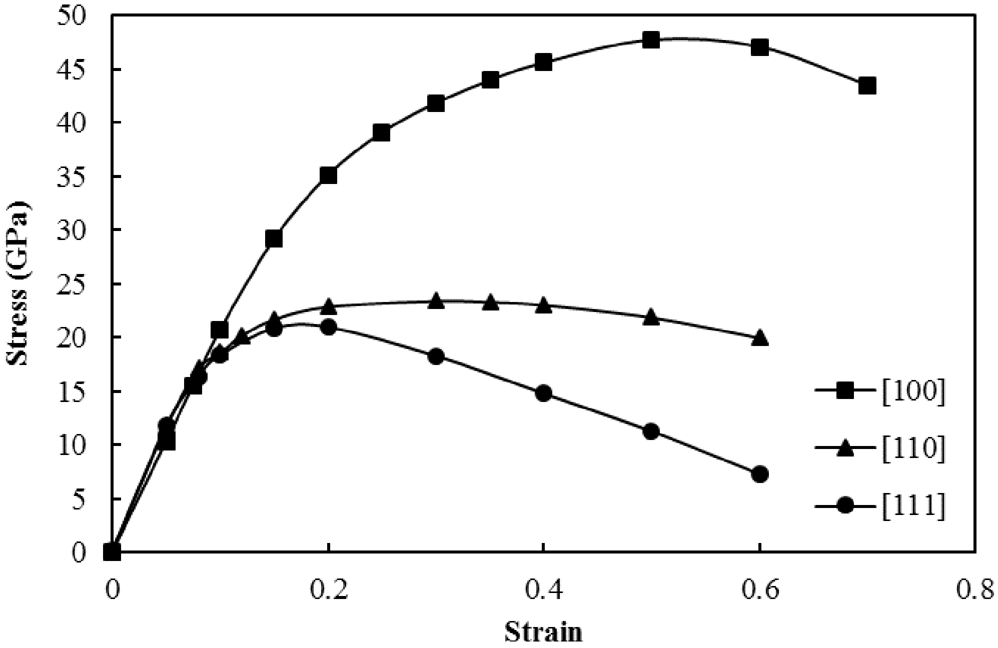

Figure 3.5. DFT-calculated tensile stress-stain curve.

tively. The ions positions of all the DFT models are relaxed using conjugate-gradient algorithm before and in the deformation calculations. In the tensile simulation, the model is uniaxial elongated in the z-direction, so the tensile stress is obtained directly from the stress tensor in the z direction. Figure 3.5 shows the tensile stress-strain curves calculated using first principle calculations. The linear elastic stage on these curves only occurs in the first a few steps, then the stress drops slowly after it reached the ultimate tensile strength. The LZ tensile model in [001] direction has the largest ultimate tensile strength, and the LZ tensile models in [110] and [111] directions have similar ultimate strength. Young's modulus can be calculated from the slope of the linear section in the curve using Hooke's law. The Young's moduli in [001], [110] and [111] directions are obtained from the slope of the linear fitted line, which corresponds to the strain from 0 to 0.1 in [001] direction, and from 0 to 0.08 in [111] and [110] directions. The toughness can be calculated from the integration of the area under the stress-strain curve. The calculated Young's modulus, ultimate tensile strength, and toughness are summarized in Table 3.3. The single crystal LZ has the maximum tensile Young's modulus in [111] direction, and minimum Young's modulus in [001] plane, this trend is consistent with Liu's results [143]. In the nanoscale DFT simulation results, the quasi-plastic deformation stage occurs on the stress-strain curves rather than the ideally elastic-brittle type [144]. The stress and strain are largely increased during the quasi-plasticity stage, which determined the magnitude of ultimate strength and toughness. Although Young's modulus in [001] direction is lower than that in [110] and [111] directions, the tensile stress-strain curve in [001] direction possesses a higher "yield" point in quasi-plasticity stage than that in [110] and [111] directions. As a result, the LZ tensile model in [001] direction has the maximum ultimate strength and toughness. The ultimate strength and the toughness are properties of large deformation; however, Young's modulus is a property of small elastic deformation. These properties describe stress-strain relations under different deformation circumstances, so they exhibit the different trends.

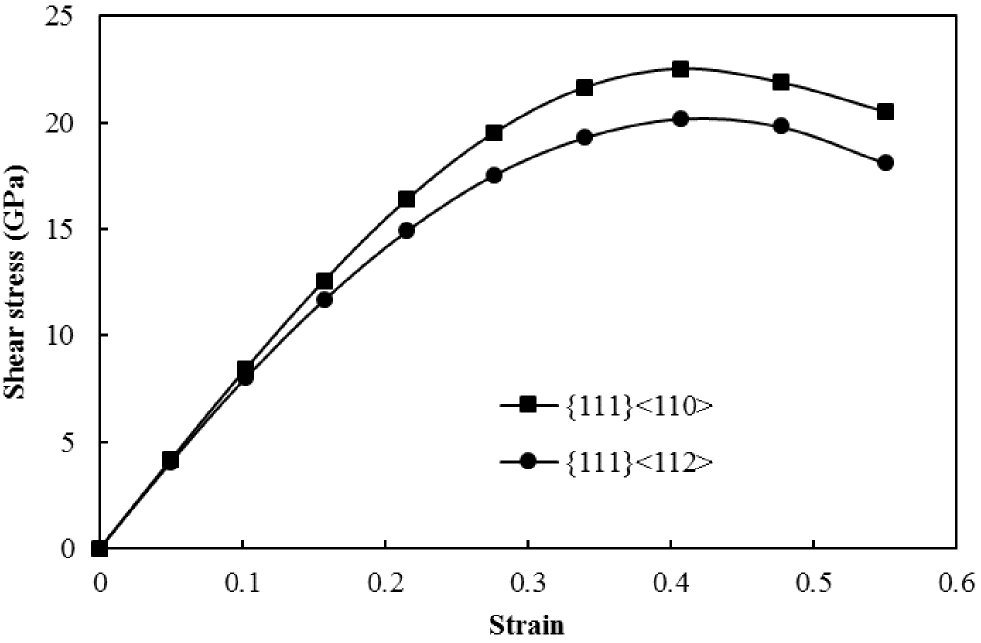

Figure 3.6. DFT-calculated shear stress-stain curve.

Table 3.3. Calculated elastic modulus, ultimate strength, and toughness.

Calculation model	**Elastic modulus (GPa)**	**Ultimate strength (GPa)**	**Toughness (MJ/m^3)**
DFT Tensile [001]	207.211	47.747	21.565
DFT Tensile [110]	213.225	23.453	12.219
DFT Tensile [111]	222.596	20.980	8.934
MD Tensile [001]	230.355	30.250	3.018
MD Tensile [110]	226.897	18.867	2.192
MD Tensile [111]	229.751	18.914	1.839
DFT Shear {111}<110>	76.037	22.507	8.862
DFT Shear {111 <11$\bar{2}$>	73.381	20.192	8.028
MD Shear {111}<110>	-	29.008	-
MD Shear {111}<11$\bar{2}$>	-	20.774	-

Figure 3.6 shows the DFT-calculated shear stress-strain curves in two slip system {111}<11$\bar{2}$> and {111}<110>. Basically, the two curves are very similar. As summarized in Table 3.3, the shear modulus of {111}<110> is slightly larger than that of {111}<11$\bar{2}$>, and so as the ultimate shear strength and the toughness, although the differences are very small. When the two slip systems of LZ crystal are under the same stress level, the corresponding strain in {111}<11$\bar{2}$> direction is larger than that in {111}<110> direction. Based on these DFT-calculated results, in single crystal LZ material, the {111}<11$\bar{2}$> direction system is more likely to slip in the shear deformation.

3.4.2 Small Deformation Elastic Moduli Calculation

The elastic constants C_{11}, C_{12} and C_{44} of LZ single crystal were calculated using DFT method in small deformation condition, which were 256.001 GPa, 116.425 GPa and 86.708 GPa, respectively. The effective elastic moduli of LZ were calculated using Equation (3.1) – Equation (3.6), as summarize in Table 3.4. Selected experimental results from the literature are also listed in Table 3.4 as a comparison. In these literature results, Zhang et al. measured the Young's modulus of 7 % porous LZ coating using nanoindentation [48], and Shimamura et al. studied the moduli of LZ materials using the ultrasound pulse-echo measurement [23]. Comparing with the experimental data from the literature, the effective moduli of the LZ are in a reasonable range.

Table 3.4. Effective moduli of LZ and the expeirmental results.

	Effective moduli	**Experimental results**
Young' s modulus (GPa)	205.12	15610 (Zhang [48]) 280 (Shimamura [23])
Bulk modulus (GPa)	162.95	216 (Shimamura [23])
Shear modulus (GPa)	79.49	109 (Shimamura [23])
Poisson' s ratio	0.29	0.28 (Shimamura [23])

The anisotropic characteristics can be determined by Zener anisotropic ratio, which is defined as $Z = 2C_{44}/(C_{11}\text{-}C_{22})$ [131]. If the Z = 1, the material is isotropic. The calculated Z value for LZ is 1.24, indicating that the elastic modulus of LZ is anisotropic, and the maximum Young's modulus is in <111> direction. Anisotropic Young's modulus of cubic LZ crystal can be expressed using the DFT-calculated elastic constants, which is given by the following equations [131].

$$\frac{1}{E} = \frac{l^4 + m^4 + n^4}{E_0} + \frac{2(m^2n^2 + n^2l^2 + l^2m^2)}{F_0} \tag{3.10}$$

$$\frac{1}{E_0} = \frac{C_{11} + C_{22}}{(C_{11} - C_{22})(C_{11} + 2C_{22})} \tag{3.11}$$

$$\frac{2}{F_0} = \frac{-2C_{12}}{(C_{11} - C_{22})(C_{11} + 2C_{22})} + \frac{1}{C_{44}} \tag{3.12}$$

where l, m, n are directional cosines. The (110) plane is chosen in this work for the anisotropic calculation because it includes all three of the principal directions in a cubic crystal <111>, <110> and <001>. The directional cosines for (110) plane can be calculated by:

$$l = cos\theta \qquad\qquad m = \frac{sin\theta}{\sqrt{2}} \qquad\qquad n = \frac{sin\theta}{\sqrt{2}} \tag{3.13}$$

where θ is the angle in (110) plane, which measured from [100] direction to the [110] direction.

The anisotropic Young's modulus results are plotted in Figure 3.7, including the solid curve calculated from the elastic constants of the LZ single crystal in small deformation status, and the scattered points calculated from the DFT and the MD (MD results will be discussed in section 3.4.4) stress-strain curves in large deformation tensile simulation. As shown in Figure 3.7, most of anisotropic Young's modulus results are very close to each other, suggesting that these modeling studies have good consistency and accuracy.

3.4.3 Bader Charge Analysis and Charge Density Distribution

Bader charge transfer was calculated according to each atom in the tensile and shear systems. The unit of Bader charge is electron (e), which means that the number of the electrons that one atom gains or losses. The average Bader charge difference between cation and anion reveals the electron interaction between those two types of atom, which relate to the bonding character of those atoms. The high average Bader charge difference leads to a strong bond. Table 3.5 summarizes the Bader charge differences between cation and anion in each tensile and shear deformation. The charge differences between Zr and O, and between La and O in tensile [111] calculation are the largest among three tensile cases, suggesting the bonding strength

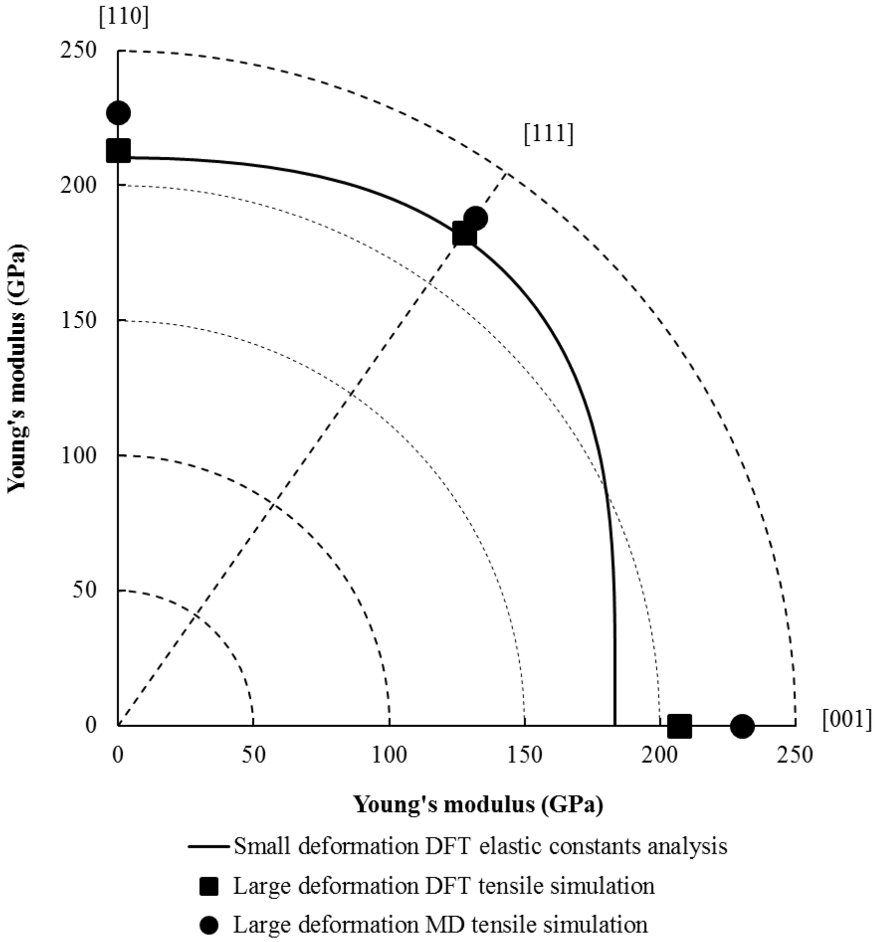

Figure 3.7. Summary of anisotropic Young' s modulus.

in the tensile model in [111] direction are the strongest. The strong bond between the cation and anion in the [111] tensile model corresponds to the high Young's modulus result in the DFT calculations. In the shear models, the average Bader charge difference in LZ shear model in {111}<110> direction is slightly larger than that in {111}<11$\bar{2}$> direction, suggesting the atom bond in {111}<110> shear model is stronger than that in {111}<11$\bar{2}$> direction. The stronger bond in the shear model in {111}<110> direction results to higher Young' s modulus than that of the shear model in {111}<11$\bar{2}$> direction.

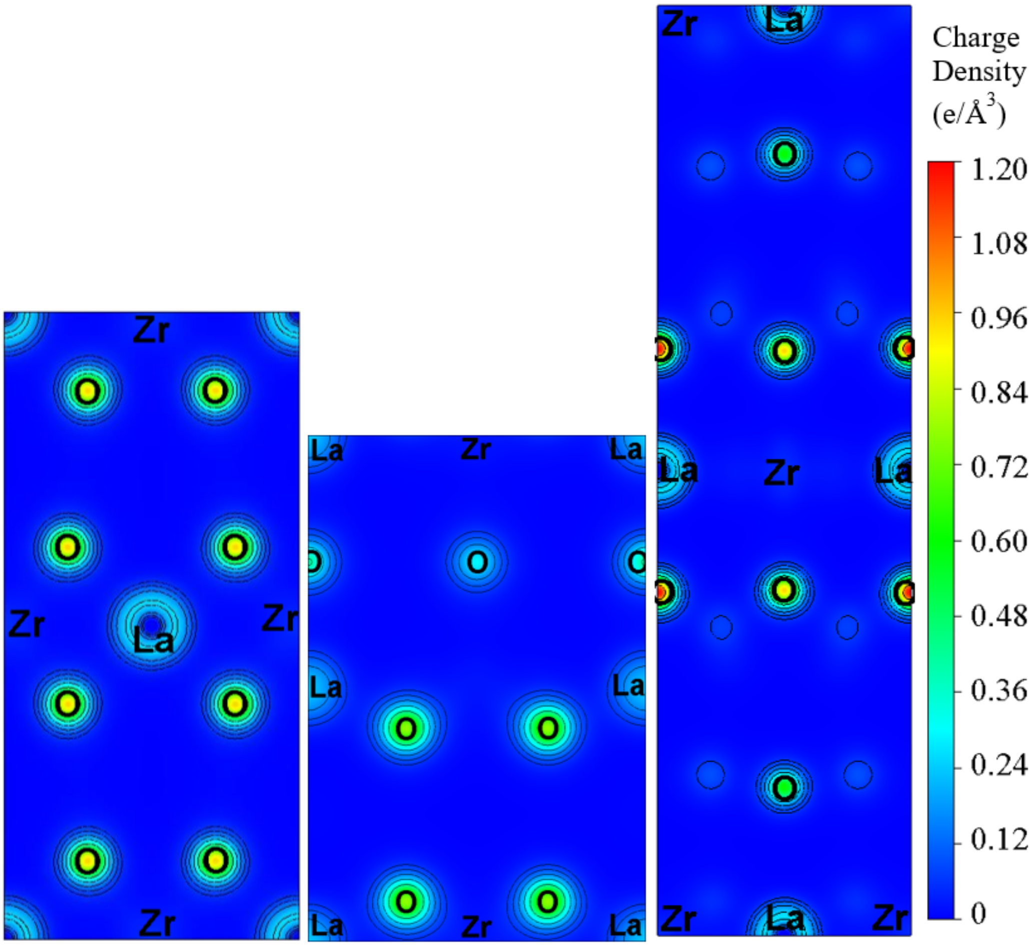

(a) (b) (c)

Figure 3.8. Charge density distribution (e/Å^3) of tensile calcualtion at strain of 0.5 in (a) [001] direction, (b) [110] direction and (c) [111] direction.

The color map of charge density distribution in each LZ tensile simulation at the strain of 0.5 are plotted in Figure 3.8. Charge density distribution reveals the election gain and loss characteristic. The red color indicates election gain and the blue color indicates the election loss. As shown in Figure 3.8, the Zr atoms lost almost all its valence election to the O atoms. The Density distributions near O atoms are similar between the [001] tensile model and [110] tensile model. However, the [111] tensile model has the highest charge density near O atom among all the tensile models,

Table 3.5. Calculated average Bader charge difference between O – Zr and O – La atoms.

	Young's modulus (stress-strain DFT analysis)	**Average Bader Charge difference (O – Zr)**	**Average Bader Charge difference (O – La)**
Tensile [001]	188.139	4.592	3.469
Tensile [110]	189.556	4.804	3.603
Tensile [111]	208.462	5.106	3.696
Shear {111}<110>	76.037	4.965	3.568
Shear {111}<11$\bar{2}$>	73.381	4.893	3.535

suggesting the electron interaction in [111] tensile model are the strongest. This strong electron interaction leads to a high Young's modulus in [111] direction.

3.4.4 MD Tensile and Shear Simulations

Figure 3.9 shows the models of the first and the last steps of the MD tensile calculations in [001] direction. The model image of initial step demonstrates the perfect LZ single crystal without any tensile strain. The model image of 0.16 strain step shows that there are some vastly deformed areas in the model, which reach its critical strength and are about to break apart.

Figure 3.10 shows the MD-calculated tensile stress and strain curves in [111], [001], [011] directions. All the stress-strain curves in these tensile simulation cases exhibit an elastic stage and the stress drops after the ultimate strength is reached. The slopes of these stress-strain curves in the elastic stage are very similar when the strain is at the beginning stage (less than 0.03). Then, the slope changes as the increase of the stress, when the deformation occurs in the tensile model. The Young's moduli of LZ

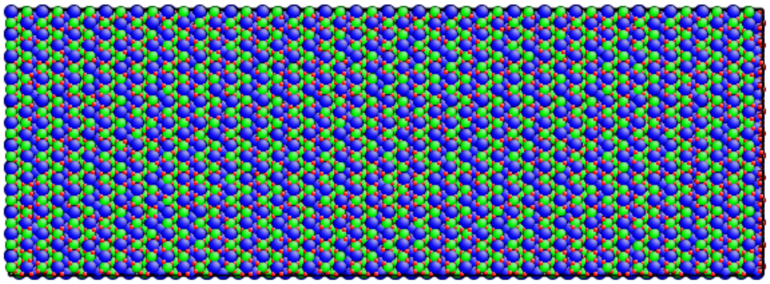

(a) The initial step (no strain)

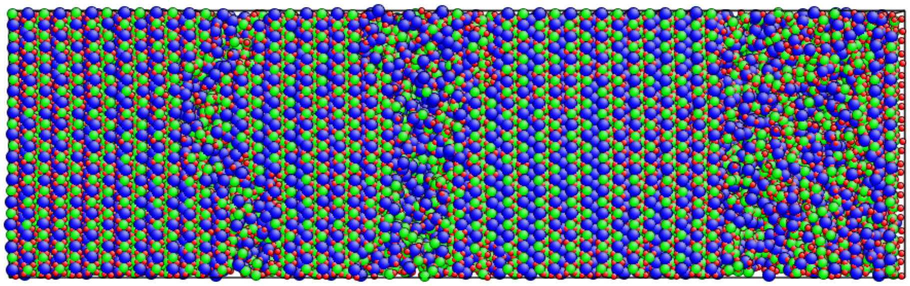

(b) The step with 0.16 strain

Figure 3.9. MD-calculated tensile model in [001] direction. Each ball shown as green, red, and blue indicates Zr atom, O atom and La atom, respectively.

in [111], [001], [011] directions are calculated from the slope of the elastic stage on the MD-calculated stress-strain curves, whose strains range from 0 to 0.03, as summarized in Table 3.3. The Young's modulus values in [001] and [111] directions are very close to each other, which are higher than that in [110] direction. The stress-strain curve in [001] direction shows longer linear elastic stage and higher ultimate stress than the stress-strain curves in other two directions, indicating that LZ has a larger toughness in [001] direction than that in [110] and [001] directions. The MD-calculated ultimate tensile strengths share the same trend with the DFT results. However, the magnitude of Young's modulus, ultimate strength and toughness results are different with DFT results, as listed in Table 3.3. This is primarily due to the different scale in dimension and different atom number between DFT and MD calculations. The MD models used in this works are about several hundred times larger than the DFT model in both atom number and dimensions.

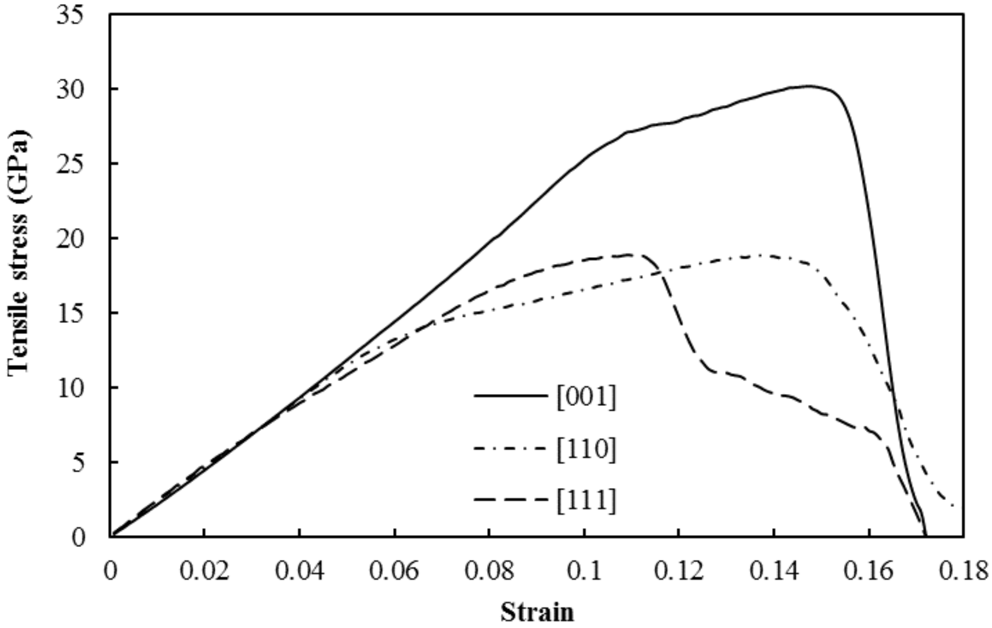

Figure 3.10. The MD-calculated tensile stress-strain curves.

The shearing stress is derived from the virial theory by averaging the virial stress over the whole system, which includes both the potential and kinetic energies [145]. The shear stress is calculated by the following equation:

$$\tau = -0.5[\sigma_{xx} - 0.5(\sigma_{yy} + \sigma_{ZZ})] \tag{3.14}$$

where x is the uniaxial compression axis [146]. The relation between the resolved compression and shear slip system is also considered. The orientation of the slip plane in the LZ normal compression model is very close to the initial compression axis, so the compressive shear strain is used to specify the strain in the slip plane as a simplification [146].

Figure 3.11 shows the MD-calculated shear stress-strain curves in [110] and [112] directions. The shear stress-strain curves have the similar form as the tensile stress-strain curves, which show a linear elastic stage. The ultimate shear strength in

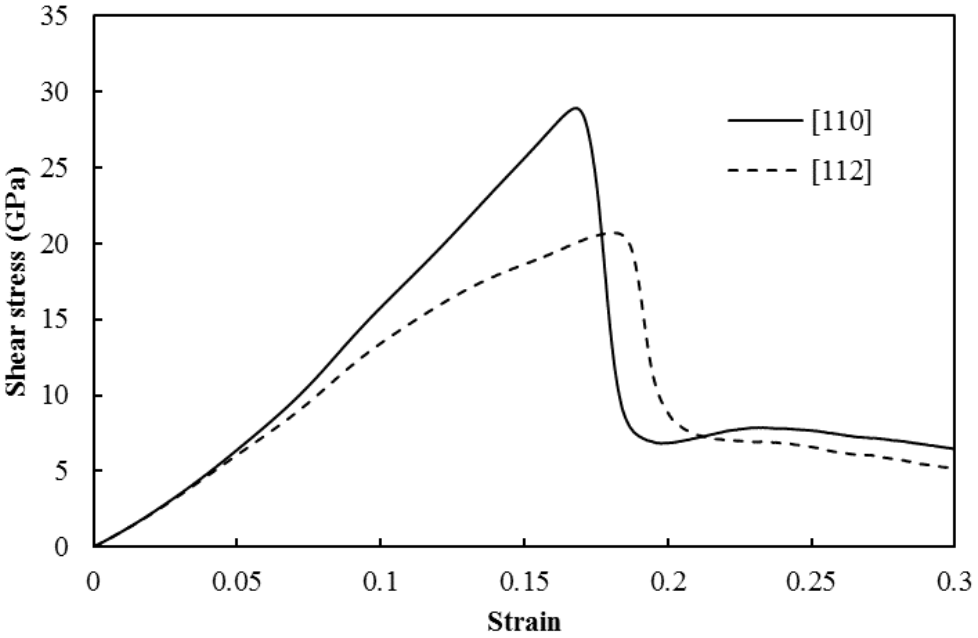

Figure 3.11. The MD-calculated shear stress-stain curves.

[110] direction is obviously larger than that in [112] direction. Similar to the DFT-calculated shear stress-strain curves, the MD shear results also indicate that the LZ single crystal in [112] direction is more likely to slip than in [110] direction.

3.5 Summary

In this work, the conventional unit cell of the single crystal LZ was built, and the lattice constant of LZ unit cell was optimized using the DFT calculations. Based on the LZ unit cell model, the nanoscale tensile and shear simulations for LZ single crystal material were performed using the DFT and the MD calculations, and the corresponding mechanical properties were calculated using two approaches: stress-strain curve analysis in large deformation and elastic constants analysis in small deformation. The DFT-calculated results of both methods are very close, suggesting the consistency of these two methods. Compare experimental results from the literature data, the effective elastic moduli calculated from Voigt-Reuss-Hill approximation have a good accuracy. The major conclusions of this chapter can be summarized as the following aspects.

(1) The actual lattice constant of LZ was calculated by minimization of the total energy. The DFT-calculated LZ lattice constant is 10.875 Å, which has an error of 0.68 % comparing to the experimental result.

(2) The elastic moduli of LZ single crystal are anisotropic. The DFT results show that the largest Young's modulus occurs in [111] direction. The average Bader charge difference analysis indicates that the bonds between Zr and O, and between La and O are the strongest in LZ tensile model in [111] direction. The charge density distribution analysis exhibits the strong electron interaction in tensile [111] model, which leads to a high Young's modulus.

(3) The DFT-calculated shear stress-strain curves in {111}<110> and $\{111\}<11\bar{2}>$ slip systems are very similar, so as the average Bader charge difference between the cations and anions in these two models. The most likely slip system in {111} plane is $\{111\}<11\bar{2}>$, because more strain is generated in $\{111\}<11\bar{2}>$ shear model than that in {111}<110> shear model under the same stress level.

(4) The MD-calculated tensile and shear stress-strain curves show the same trend as the DFT-calculated results. However, the values of the mechanical properties calculated using the MD method are quite different from the DFT results, because the scale in dimensions and number of atoms are different between the MD and the DFT models.

CHAPTER 4. THERMAL PROPERTIES MODELING OF LZ

4.1 Introduction of Thermal Properties Calculations

TBCs are operated in the high-temperature environment, so the thermal properties are very important for TBC material. The primary requirements of TBCs for the turbine designer are low thermal conductivity [1, 6]. Although there are several experimental methods to measure the thermal conductivity, such as flash method and pulsed thermal imaging-multilayer analysis (PTI-MLA) method (see section 4.3.3), no theoretical modeling calculation of the thermal conductivity is performed on the LZ material. Actually, the intrinsic thermal conductivity of single crystal LZ is almost impossible to be accurately measured using experimental method due to the porous and fragile characteristic of the LZ powder, which includes the huge number of defects. In addition, the experimental equipment has limitations on the temperature range and the sample size. However, the theoretical calculation does not have the temperature limitation.

In this chapter, the specific heat of single LZ crystal was calculated based on the optimized LZ unit cell using DFT calculations. Then, we propose a novel image-based multi-scale simulation framework combining MD and FE method calculations to study the thermal conductivity of LZ thermal barrier coating. A reverse non-equilibrium molecular dynamics approach is used at first step to compute the temperature-dependent thermal conductivity of LZ single crystal. Then, the single crystal data is plugged into an FE model of a thermal barrier coating that generated using SEM microstructures images. The predicted thermal conductivities from the FE model are compared against thermal conductivity experimental results using both flash laser and PTI-MLA techniques.

4.2 Thermodynamic Energy and Specific Heat of LZ

The thermodynamic energies (Gibbs free energy, enthalpy and entropy) and specific heat capacity calculations of the LZ unit cell were implemented by CASTEP code in this work [84]. The thermodynamic energies and specific heat can be well described using a quasi-harmonic Debye model, in which the non-equilibrium Gibbs function G*(V, P, T) is expressed as the following equation [147].

$$G^*(V(x), P, T) = E(x) + PV(x) + A_{vib}[V(x), T] \tag{4.1}$$

where x represents all the geometric information such as lattice constant, E(x) is the total energy of LZ unit cell, PV(x) represents the energy in constant hydrostatic pressure condition, and A_{vib} is the vibrational Helmholtz free energy. E(V) and PV can be obtained from DFT calculation results, so the next step is to calculate the vibrational contribution A_{vib} using Debye model of the phonon density of states:

$$A_{vib}(\Theta, T) = nkT[\frac{9}{8}\frac{\Theta}{T} + 3ln(1 - e^{-\Theta/T} - D(\frac{\Theta}{T})] \tag{4.2}$$

where Θ(V) is Debye temperature, n represents the number of atoms per formula unit, and D(y) is the Debye integral that defined as:

$$D(y) = \frac{3}{y^3}\int_0^y \frac{x^3}{e^x - 1}dx \tag{4.3}$$

In Debye's theory, the vibration of a solid is considered as elastic waves, so the Debye temperature of the solid is related to the average sound velocity. In addition, Debye temperature in a solid material is also determined by phonon perturbation and lattice vibration, which can be computed as:

$$\Theta = \frac{h}{k}(6\pi^2 V^{1/2} n)^{1/3} f(\upsilon)\sqrt{\frac{B}{M}} \tag{4.4}$$

where M represents the molecular mass, B is the adiabatic bulk modulus, υ is Poisson ratio, and f(υ) is given by the following equation:

$$f(\upsilon) = \{3[2(\frac{2}{3}\frac{1+\upsilon}{1-2\upsilon})^{2/3} + (\frac{1}{3}\frac{1+\upsilon}{1-\upsilon})^{2/3}]^{-1}\}^{1/3} \tag{4.5}$$

The Phonon calculations in CASTEP are used to evaluate the enthalpy, entropy, free energy, and the specific heat capacity of the LZ unit cell as a function of temperature in the quasi-harmonic Debye approximation. The specific heat (C_v) can be expressed using the following equation [147].

$$C_v = 3nk[4D(\Theta/T) - \frac{3(\Theta/T}{e^{\Theta/T} - 1}] \tag{4.6}$$

The calculated thermodynamic energy curves are shown in Figure 4.1, in a temperature range of 0 – 1800 K. The entropy increases as temperature increases, which is consistent with the second law of thermodynamics. The enthalpy increases slowly and the free energy decreases as the temperature increases. The enthalpy indicates the amount of heat transfer into the crystal cell. Since the Gibbs free energy equals to the enthalpy minus the product of temperature and entropy, it is reasonable that the free energy decreases as temperature increases.

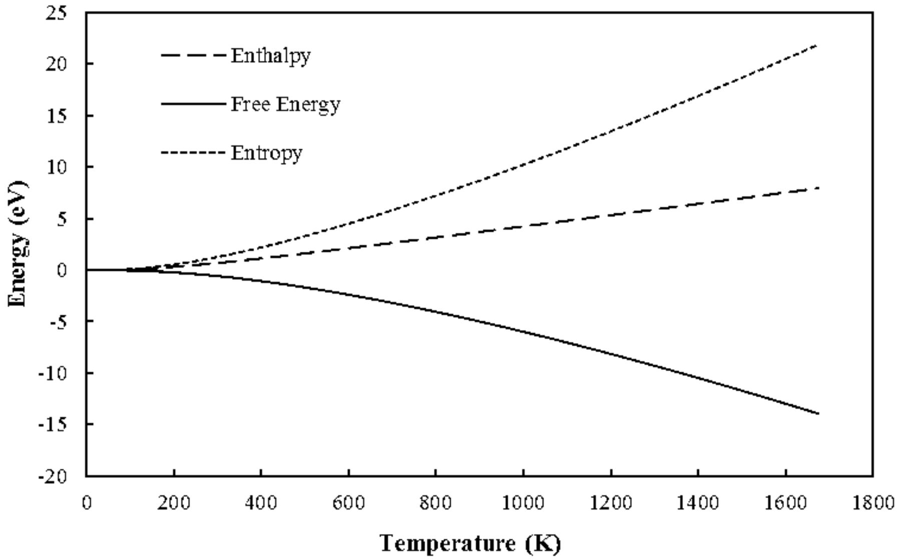

Figure 4.1. Thermodynamic energy curves of LZ as a function of temperature.

The calculated specific heat (C_v) curve in constant pressure shows in Figure 4.2, in a temperature range of absolute zero to 1327 °C, which is very difficult to measure by experiment in such wide temperature range. The value of specific heat increases

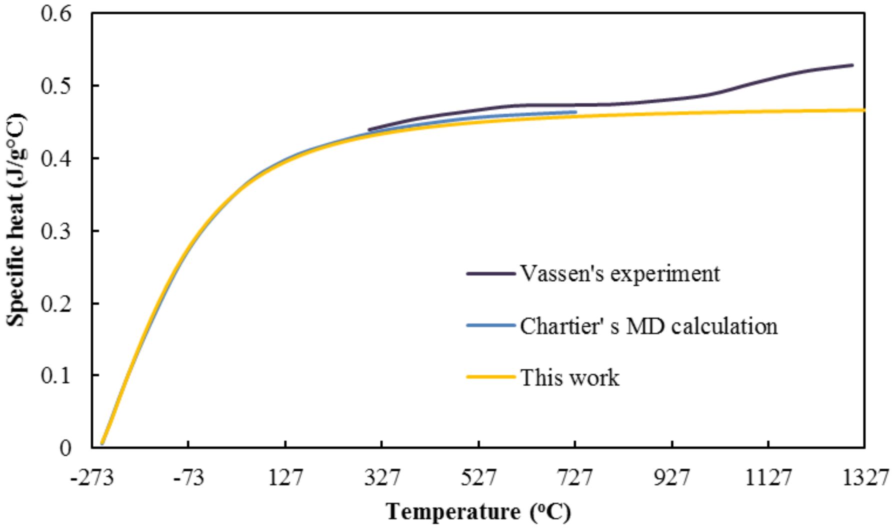

Figure 4.2. Specific heat results and comparison to literatures.

as the temperature increases, especially in a low-temperature range it increases very rapidly. When the temperature reaches above 400 °C, the specific heat increases very slowly, the value is 0.4 – 0.467 J/(g·°C) from 400 °C to 1400 °C.

Comparing experiment data from Vassen's work [15, 40] and calculated results from Chartier's work [148], it can be concluded that the specific heat calculated in this work is accurate and reliable.

4.3 Thermal Conductivity of LZ

4.3.1 Thermal Conductivity of Single Crystal LZ Using MD Simulation

The MD method can be used to investigate the thermal conductivity. For single crystals, there are two common molecular dynamics methods for thermal conductivity calculations: direct method [149,150] and Green-Kubo method [151,152]. The direct method is a non-equilibrium molecular dynamics (NEMD) method which imposes a temperature gradient to the system. The Green-Kubo method is an equilibrium MD (EMD) method which uses the current fluctuation to calculate the thermal conductivity according to the fluctuation-dissipation theorem [153]. Based on the NEMD, a more reliable method to compute thermal conductivity was developed, which is the reverse NEMD (RNEMD) method [154]. In RNEMD method, the Muller-Plathe algorithm [155] is applied to exchange kinetic energy between two atoms in different regions of the simulation box at every finite step to induce a temperature gradient in the system. It works by exchanging velocities between two atoms in different parts of the simulation cell. At set intervals, the velocity of the fastest atom in one region is replaced by the velocity of the slowest atom in another region and vice versa. Consequently, the first region becomes colder, whereas, the second region increases in temperature. The system will be reacted by flowing energy from the hot to cold regions. Eventually, a steady state is established when the exchanged energy equilibrates the energy flowing back in a temperature gradient over the space between the two regions. This enables the thermal conductivity of a material to be calculated. The usual NEMD approach is to impose a temperature gradient on the system and measure the response as the resulting heat flux. In RNEMD using the Muller-Plathe algorithm, the heat flux is imposed, and the temperature gradient is the system' s response. The advantage of RNEMD over traditional NEMD is that there are no artificial "temperature walls" in the simulated system because these cause a fluid structure different from the bulk. Additionally, energy and momentum are conserved, and there are no thermostat issues [154].

The reverse non-equilibrium molecular dynamics (RNEMD) method is used to predict temperature-dependent thermal conductivities of the single crystal LZ model in this work. The thermal conductivity model is assembled using the geometry optimized LZ unit cell, which contained 2×2×30 unit LZ cell and had the dimension of 21.6×21.6×324 Å^3 in x,y,z directions [156]. The thermal conductivity model (LZ supercell model) contains total 10560 atoms, including 6720 O atoms, 1920 La atoms, and 1920 Zr atoms. The supercell model is sliced into 30 layers with equal thickness. A temperature decay constant 0.1 per picoseconds is imposed in each layer. The thermal conductivity calculations are performed as the energy flux divided by the temperature gradient [154]:

$$\kappa = \frac{\dot{q}}{\partial T/\partial z} \tag{4.7}$$

where κ is thermal conductivity, $\dot{q}$ is heat flux defined by the amount of heat (Q) transferred per unit time per unit area in heat transfer direction; ∂T/∂z is the temperature gradient in the heat transfer direction. The universal force field was used in this work, which has a full coverage of the periodic table [157].

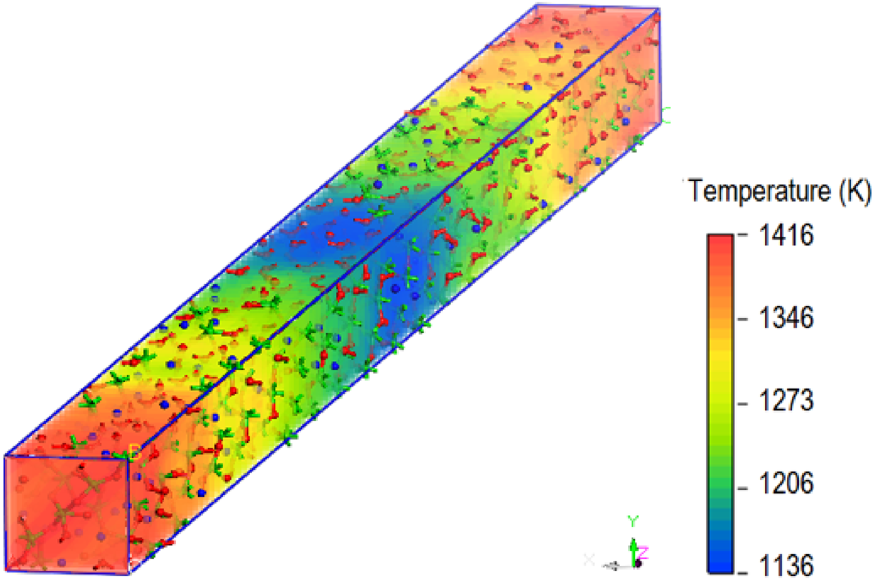

Figure 4.3. Temperature distribution in LZ single crystal supercell at 1273 K.

One of the calculated temperature distribution contour in the LZ supercell model is shown in Figure 4.3. There are two high-temperature hot zones at the ends due to the periodic boundary condition, and a low-temperature cold zone in the middle for generating a temperature gradient. The target temperature in Figure 4.3 is 1273 K, which is the average temperature in the supercell [158].

The temperature gradient along the heat flux direction in the supercell is plotted in Figure 4.4. Two linear temperature gradients were identified and the thermal conductivity was calculated using Equation (4.7).

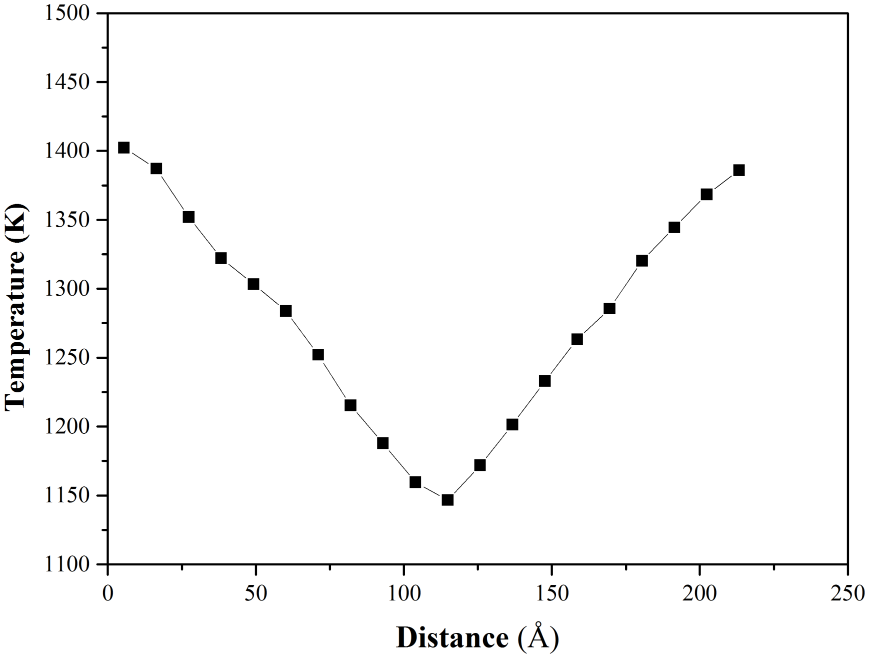

Figure 4.4. Temperature distribution along the heat flux direction.

The calculated temperature-dependent thermal conductivity of LZ single crystal is shown in Figure 4.5. The thermal conductivity values range from 1.25 W/m/K to 1.39 W/m/K in the temperature range of 473 – 1273K. It is noted that thermal radiation effect at high temperatures is not considered in this RNEMD model. Our predicted LZ single crystal thermal conductivity is lower than Schelling' s NEMD result (1.98 W/m/K at 1200 °C [149]), probably due to two factors. One is the method, Schelling used NEMD and we use RNEMD. The second is the different force fields used in the model. Schelling used Buckingham potentials and this work applied the universal force field. Schelling' s single crystal result compared reasonably well with fully dense polycrystalline experimental data. However, the influence of microstructure in the polycrystalline was not considered in Schelling' s work. In our model, we also calculate temperature-dependent thermal conductivity of polycrystalline LZ using the FE model as discussed below.

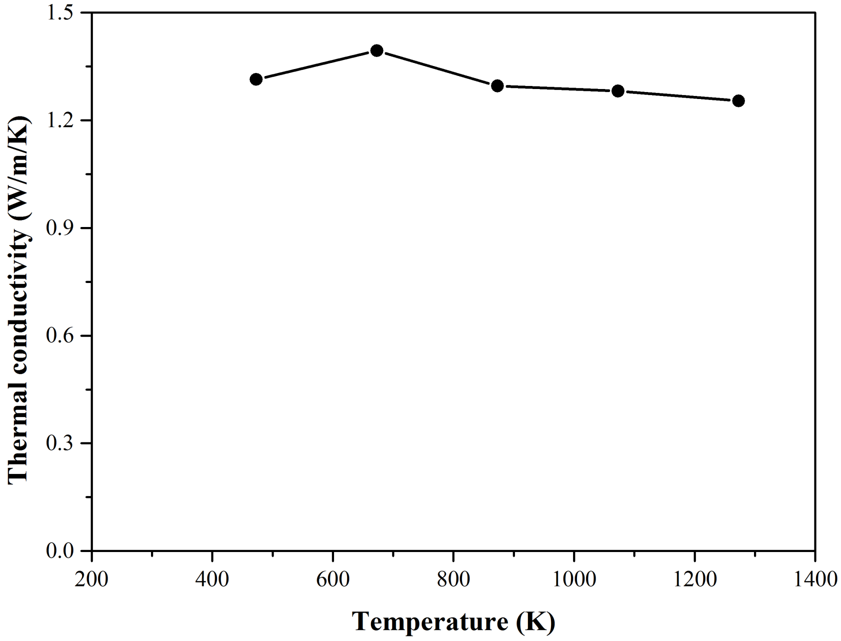

Figure 4.5. Temperature-dependent thermal conductivity of LZ single crystal using the RNEMD method.

4.3.2 Thermal Conductivity of Polycrystalline LZ Coating

Finite element (FE) method can be used to simulate the heat conduction process of a coating structures with cracks and pores [159]. The pore and crack morphology of thermal barrier coating is an important parameter affecting the mechanical and thermal properties [160, 161]. The quantitative imaging analysis method can be used to investigate the non-uniformity properties of the porous coating with polycrystalline microstructure [46, 48]. Based on the quantitative imaging analysis, the image-based FE method uses scanning electron microscope (SEM) images to generate microstructures and import into an FE model [162]. Therefore, the image-based FE method is able to calculate the thermal conductivity of non-uniform porous polycrystalline coatings.

Three representative SEM images of the cross-sectional view of the porous LZ TBC sample with the porosity of 13.61 % are converted into binary images using imaging processing software package ImageJ [163]. In the binary images, white color regions represent solid LZ coating phase, and black color regions are pores and cracks. The binary images then are passed into to an FE software package, COMSOL Multiphysics [164], to automatically generate FE meshes. In the FE models, a constant temperature difference boundary condition is applied at the top (T_{top}) and bottom (T_{bot}) surface of the system, with the average temperature ($T_{top}/2+T_{bot}/2$) as the target temperatures, 473 – 1273 K. The pores and cracks are filled with non-flowing air. Zero thermal conductivity is assumed for the pores and cracks because the thermal conductivity of non-flowing air is much smaller than that of the coating [165,166]. For LZ coating solid phase, the calculated temperature-dependent thermal conductivities of LZ single crystal from RNEMD are used.

For porous LZ polycrystalline coating samples, SEM images of cross-sectional views of three free-standing coating samples were used. A representative SEM image of LZ coating is shown in Figure 4.6(a). The simulated temperature contour in the sample is shown in Figure 4.6(b). As shown in Figure 4.7, comparing with the flash method experiment results, the FE method calculated thermal conductivity values are in the good agreement with the experiments results. The cracks and pores in the coating clearly reduce the thermal conductivity of the coatings.

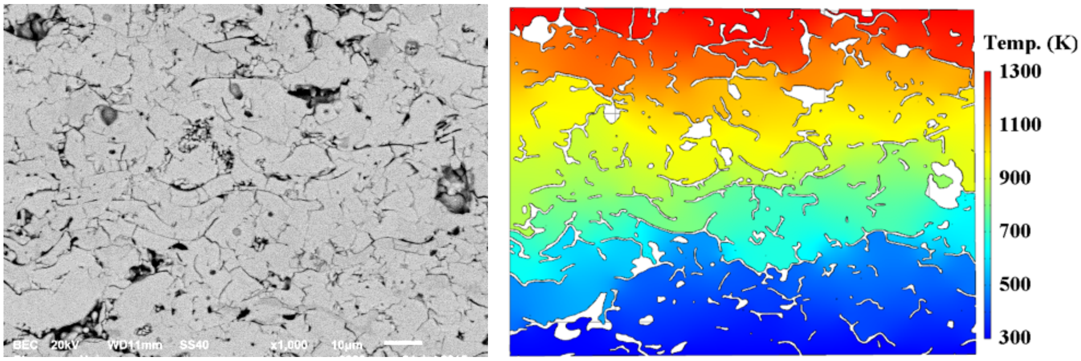

(a) (b)

Figure 4.6. (a) SEM image and (b) calculated temperature contours of LZ.

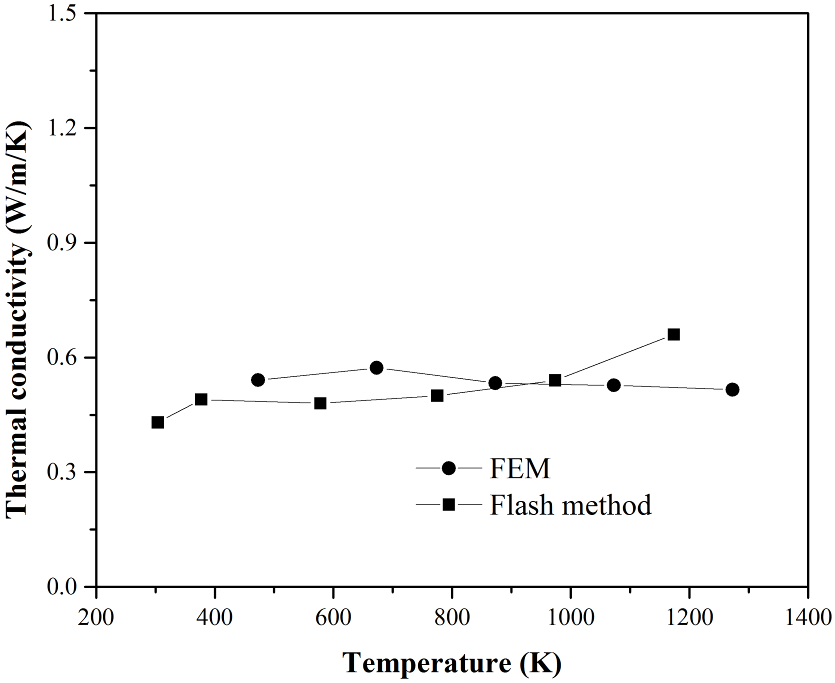

Figure 4.7. Thermal conductivity of LZ coating – FE method prediction and flash method.

Using the flash method, the averaged thermal conductivity measured from the three LZ porous coating samples is given in Figure 4.7, which ranges from 0.44 to 0.62 W/m/K in the temperature range of 300 – 1200 K. The measured thermal conductivity is relatively constant below 900 K, and slightly increases above 900 K. As shown in Figure 4.7, the predicted thermal conductivity using the FE model is in a good agreement with experimental measurement.

Pulsed thermal imaging-multilayer analysis (PTI-MLA) method is recently developed as a new method to measure the thermal conductivity [167], to overcome the limitations of the flash method. For example, the flash method requires two sides accessible for the specimens. The sample surface is destructed by the laser flash. In addition, the flash method obtains a single averaged thermal conductivity of the sample, and it does not provide the spatial distribution of the thermal conductivity [167]. In comparison, the PTI-MLA technique is a one-sided experimental system, which consists a photographic flash lamp (Source 6400; BALCAR, France), an infrared filter and a mid-wavelength (3 – 5 μm) infrared camera (Phoenix, FLIR). PTI-MLA method is based on monitoring the surface temperature decay, after it is applied with a pulsed thermal energy that is transferred inside the sample gradually [167].

In the pulsed thermal image-multilayer analysis method, the optical image of LZ coating specimen, thermal conductivity map, and heat capacity map are shown in Figure 4.8. The measured product of heat capacity is ~2.16 J/cm^3/K. The average thermal conductivity measured by the PTI-MLA technique is 0.55 W/m/K, which is also consistent with the results measured by the flash method and calculated by FE model.

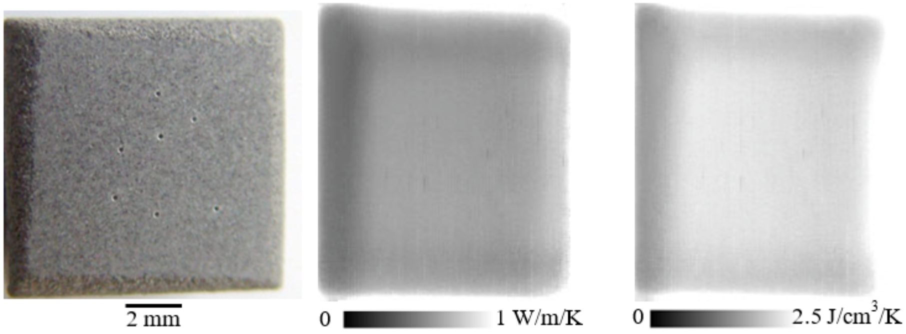

(a) (b) (c)

Figure 4.8. LZ coating (a) optical image; (b) thermal conductivity map; (c) product of heat capacity (ρc) map.

4.4 Summary

In this chapter, some thermodynamic energies (Gibbs free energy, enthalpy and entropy) and the specific heat of single crystal LZ were calculated using the DFT calculations based on a quasi-harmonic Debye model. In addition, a novel image-based multi-scale simulation framework combining the molecular dynamics and the finite element calculations has been proposed to study the thermal conductivity of the porous LZ coatings. Experimental validations include the flash method and pulsed thermal image-multilayer analysis technique were applied to measure the coating thermal conductivity. The main conclusions of this chapter can be summarized as the following aspects.

1. The calculated specific heat capacity of single crystal LZ ranges from 0.4 – 0.467 J/g/K at a temperature range from 400 °C to 1400 °C. The calculated results have a good accuracy comparing to the literature data.

2. The calculated thermal conductivity of LZ single crystal ranges from 1.25 W/m/K to 1.39 W/m/K in the temperature range of 473 – 1273K, using RNEMD method.

3. Using the image-based FE method and single crystal thermal conductivity data, the calculated thermal conductivities of porous LZ polycrystalline are in the range of 0.46 – 0.59 W/m/K at the temperature range of 473 – 1273K. The predicted FE data are in good agreement with the flash method, 0.44 to 0.62 W/m/K, in the temperature range of 300 – 1200 K, and the PTI-MLA technique, 0.55 W/m/K. The image-based multi-scale simulation framework proposed in this work provides a design tool to the future design of advanced coating systems.

CHAPTER 5. TENSILE AND SHEAR MODELING OF ZRO_2-NI INTERFACE

5.1 Introduction of Interface Modeling

It is widely accepted that the mechanical properties at the ceramic-metal interface between the top and bond coats and/or between the top coat and the TGO layer have a primary influence on the lifetime of the TBCs in the thermomechanical environments. It is still challenging to directly examine the interfacial mechanical properties from experiments. Modeling and simulation are powerful tools as an alternative way to investigate the interfacial properties and decipher failure mechanisms [168]. The failure and spallation mechanisms of the were discussed by Evans et al. in the context of continuum mechanics [125,169,170]. Evans suggested that the delamination, typically observed in TGO layer or near the interface, was related to a significant residual stress gradient which amplifies the imperfections in TBCs. Cracks propagate when the residual tensile and/or shear stresses exceed the delamination toughness of the top bond coat interface. At the atomic level, the mechanical characteristics at the ceramic-metal interface are related to the intrinsic atomic properties. The idealized mechanical properties can be calculated which offers insights into the complex interface systems. Guo et al. investigated the mechanical properties of Ni (111) / α–Al_2O_3 (0001) interface, and calculated the theoretical shear strength and unstable stacking energy, using the first principles calculations [171]. Since the LZ, 8YSZ and NiCrAlY bond coat structure is too complicated to calculate using DFT method, the ZrO_2/Ni interface structure is implemented as a simplified top and bond coat model. This simplification is reasonable because the primary composition of the 8YSZ and the LZ coatings is ZrO_2, and Ni is the primary composition of the bond coat. Christensen et al. studied the adhesion energy of ZrO_2(111)/Ni(111) interface using the ultrasoft pseudopotential within the density functional theory [172].

Although previous efforts, however, the exact mechanical properties of ZrO_2/Ni interface are still not well examined using theoretical calculation approach. Specifically, the interfacial mechanical behaviors under tensile and shear stresses are not available. The difficulty of such studies primarily stems from the complexity of the interface structure, which requires minimizing the misfit between different crystal surfaces, and intensive calculations involved in the interfacial tensile and shear deformation simulations.

In this chapter, we conduct the DFT and MD tensile and shear calculations of ZrO_2 (111)/Ni (111) interface. In the DFT modeling, an interface model in Ref. [172] is used to compare and/or partially validate the model through calculating the adiabatic work of adhesion. For mechanical property calculations, two Ni thickness of 1 and 3 atomic layers are modeled to investigate the effect of interface thickness on the mechanical properties. The crystallographic orientation (111) is considered since the primary slip system in face-centered cubic (fcc) metal crystals, such as Ni, is $\{111\}<110>$, with $\{111\}<11\bar{2}>$ being the secondary slip system [136]. Although the actual slip systems of the ZrO_2/Ni interface may be more complicated, both $\{111\}<110>$ and $\{111\}<11\bar{2}>$ should be the major slip systems. Therefore, the tensile stress-strain curve in $<111>$ direction is calculated, and the shear stress-strain curves along $\{111\}<110>$ and $\{111\}<11\bar{2}>$ directions are computed. The toughness and elastic modulus, Youngs modulus or shear modulus, are also calculated. Finally, the Bader charge analyses are conducted to explain the observed interfacial mechanical properties. In the MD model, the electron charge was considered in the force field potential. The tensile simulation in [111] direction and the shear simulation in $\{111\}<110>$ and $\{111\}<11\bar{2}>$ direction were conducted using MD method.

5.2 DFT Methods of ZrO_2/Ni Interface Model

5.2.1 ZrO_2 (111)/Ni (111) Interface Model

The constructed ZrO_2 (111)/Ni (111) interface atomistic models are shown in Figure 5.1. The cubic zirconia (c–ZrO_2) has the fluorite crystal structure (space group $Fm3m$) and Ni has a face-centered cubic (fcc) crystal structure (space group $Fm3m$). Both c-ZrO_2 and Ni small portions are cut from their bulk counterpart on (111) plane. To match the interface with minimal lattice misfit, the c-ZrO_2 and Ni small portions are rotated according to Ref. [172].

As shown in Figure 5.1, the interface model contains two layers of ZrO_2 (111) atoms, and 1 or 3 layers of Ni (111) atoms [173]. Because the O atoms and Zr atoms are not positioned in the same horizontal plane, the termination of the ZrO_2 (111) surface may result in dipole moment perpendicular to the interface. Therefore, symmetric models are built to screen out the dipole interactions. Two ZrO_2 (111)/Ni (111) interfaces are in this interface model, corresponding to a sandwich structure. This model with the interface is extended periodically in three dimensions, due to the periodical boundary condition. To calculate adiabatic work of adhesion, ZrO_2 (111)/Ni (111) interface slabs are built with a vacuum layer thickness of 10 Å, which is large enough to eliminate the interaction between each interface film layer.

The first principles calculations in this chapter are carried out using the VASP [86–88], based on the density functional theory (DFT) [77, 78].The projector augmented wave (PAW) method of generalized gradient approximation (GGA) functional is adopted to specify the exchange-correlation potential. A periodic supercell regime is used and k-point of the Brillouin zone is conducted using 3×3×1 Monkhost-Pack scheme. A conjugate-gradient algorithm is used to relax the ions into its instantaneous ground state. The plan-wave cutoff energy is 400 eV. The energy relaxation criterion for the electron is 10^{-5} eV for the self-consistency. The total forces are smaller than 0.01 eV/A in the ionic relaxation convergence criterion.

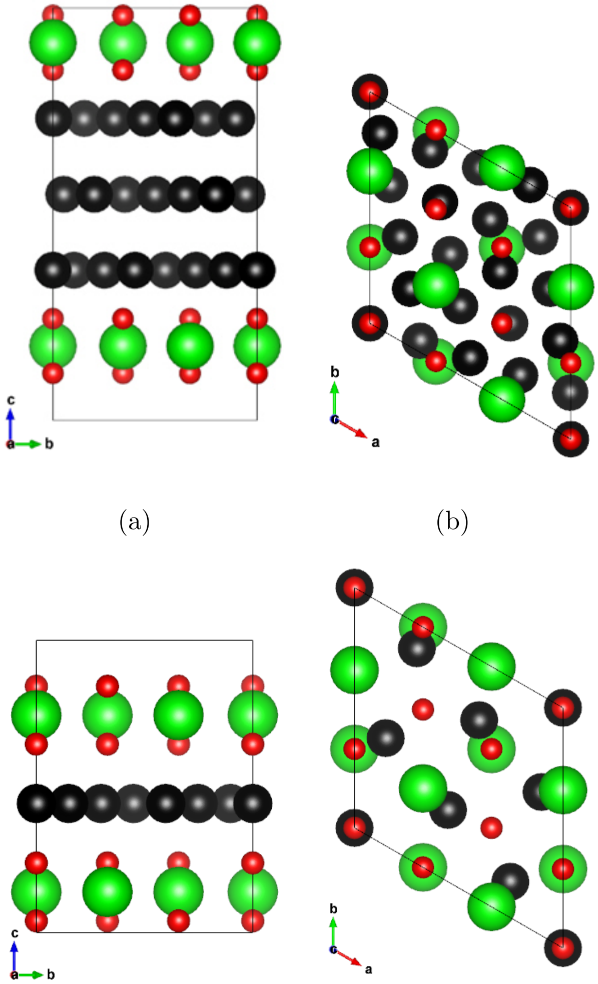

(a) (b)

(c) (d)

Figure 5.1. Figure 5.1 ZrO_2 (111)/Ni (111) interface models with different Ni atomic layers: (a) side view and (b) top view with 3 layers of Ni, and (c) side view and (d) top view of 1 layer of Ni. Green, red, and black balls are Zr, O, and Ni atom, respectively (same coloring schemes are used in all of the DFT modeling figures afterwards).

5.2.2 Adiabatic Work of Adhesion

In order to compare or partially validate the interface model, due to limited literature data, adiabatic work of adhesion (W_{adh}) is calculated using the atomistic model described in Ref. [172]. W_{adh} is the most commonly used property to describe the adhesion characteristics, which can be described using the following equation [172]:

$$W_{adh} = \frac{E_{0,Ni} + E^{N}_{0,ZrO_2} - E^{N}_{ZrO_2,Ni}}{A} \tag{5.1}$$

where $E_{0,Ni}$ and E_{0,ZrO_2} are the total energies of the relaxed Ni and ZrO_2 surfaces, respectively. $E_{ZrO_2,Ni}$ is the total energy of the relaxed ZrO_2/Ni interface structure. A is the area of the interface and N is the number of the ceramic layers [172].

5.2.3 Stress-Strain Behaviors in Tensile and Shear Deformations

For tensile deformation, the calculations are conducted by extending the lattice parameters of the interface model in [111] direction, which is perpendicular to the interface. All ions in the interface model are relaxed, and the volume and the shape of the interface unit cell are also optimized during the stress tensor calculation process. Similarly, for shear deformations, the shear stress is calculated by accumulating the shear strain in {111}<110> or {111}<11$\bar{2}$> direction [174].

5.2.4 Bader Charge Analysis

To explain the calculated stress-strain behaviors, the Bader method is used to calculate the charge transfer numbers and electron density distributions [137, 138, 175]. The charge transfer results are processed by calculating the average charge difference between O and Ni ions. This is because the bonds formed in the ZrO_2/Ni interface models through the Zr and Ni atoms losing electrons, and the O atoms gaining electrons.

5.3 DFT Interface Modeling Results and Discussion

5.3.1 Adiabatic Work of Adhesion

The relaxed ZrO_2/Ni interface models for adiabatic work of adhesion calculations are shown in Figure 5.2. In this work, all of the atoms except the two bottom Ni layers (which are away from the interface) are relaxed to allow to reach their equilibrium. Comparing with the structures in Ref. [172], the relaxed atomic structures in this study are slightly different. This is due to limited information regarding computation details in Ref. [172].

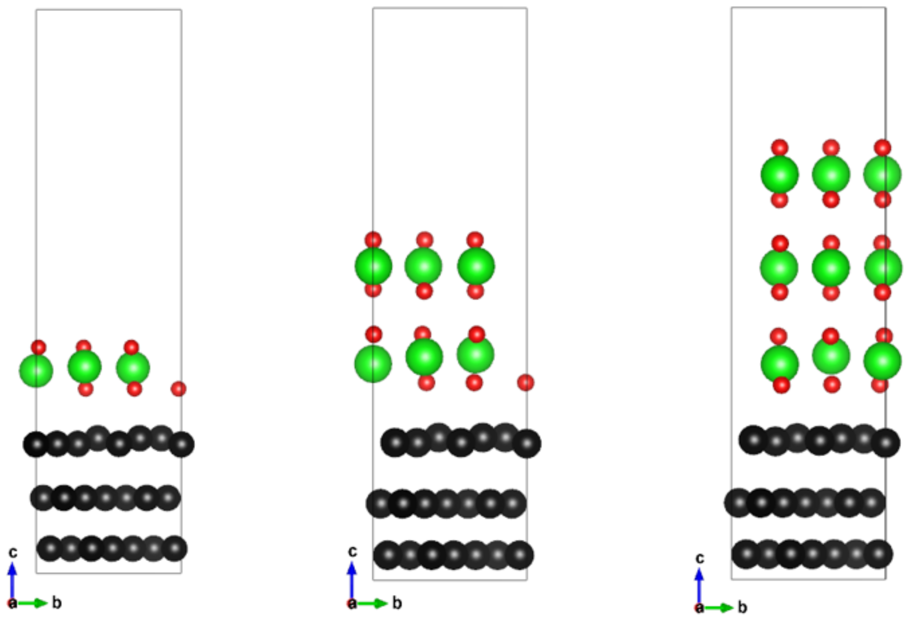

(a) (b) (c)

Figure 5.2. Relaxed ZrO_2 (111)/Ni (111) interface models with a vacume layer above the slabs: (a) 1-layer ZrO_2, (b) 2-layer ZrO_2, and (c) 3-layer ZrO_2.

In this work, the calculated Wadh value of the interface with 1-layer ZrO_2 is 629 mJ/m^2, which is greater than those of 2 and 3-layers ZrO_2 (554 mJ/m^2 and 296 mJ/m^2, respectively). In Ref. [172], the W_{adh} values are 2011, 1308, and 995 mJ/m^2

for 1, 2, and 3-layers ZrO_2, respectively. Although our calculated values are lower than reported in Ref. [172] in ∼60 %, our calculated values follow the same trend as Ref. [172], i.e., a thicker ZrO_2 layer corresponds to a lower adhesion energy.

5.3.2 Stress-Strain Behaviors in Tensile and Shear Deformations

(1) Tensile Deformation Along [111] Direction

For mechanical property calculations, the atomic configurations of relaxed tensile models along [111] direction with Ni slabs of 1 and 3 layers are shown in Figure 5.3 and Figure 5.4, respectively.

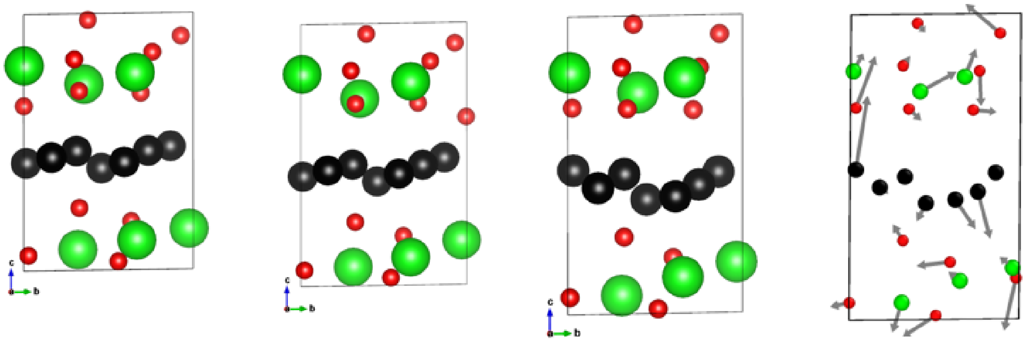

(a) (b) (c) (d)

Figure 5.3. Tensile deformation models with 1 layer of Ni: (a) initial configuration, (b) strain of 0.051, (c) strain of 0.105 and (d) atom displacement vector between strain 0.105 and initial steps.

The tensile stress-strain curves of ZrO_2 (111)/Ni (111) interface with Ni slabs of 1 and 3 layers are shown in Figure 5.5. As shown in Figure 5.5, a thinner (1-layer) Ni layer has almost double Young' s modulus (139.9 GPa) and higher ultimate tensile strength (11.6 GPa) than those of the 3-layer Ni case (60.2 GPa and 7.9 GPa, respectively) (see Table 1 for a complete summary of calculated mechanical properties, including elastic modulus, ultimate tensile/shear strength, and toughness). The layer thickness dependence is consistent with work of adhesion values in Section 3.1, i.e.,

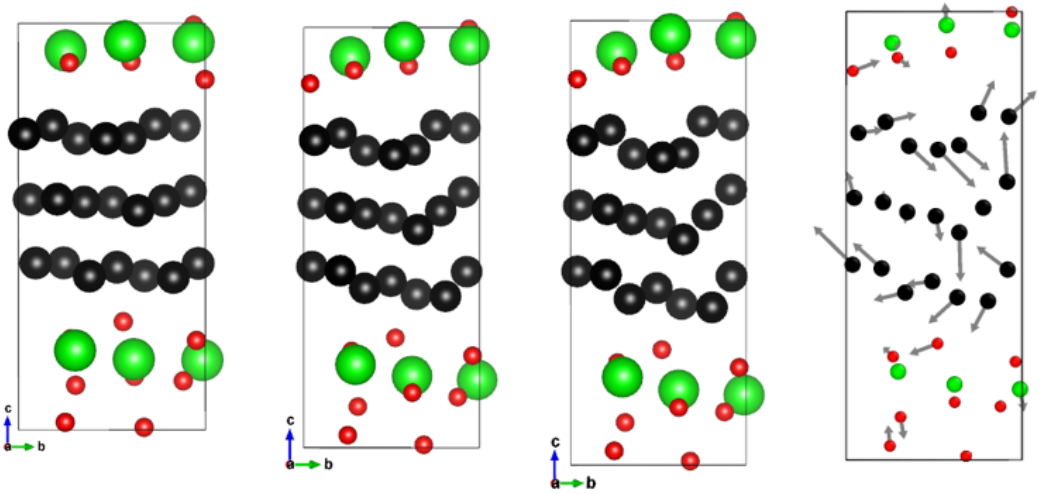

(a) (b) (c) (d)

Figure 5.4. Tensile deformation models with 3 layers of Ni: (a) initial configuration, (b) strain of 0.072, (c) strain of 0.138 and (d) atom displacement vector between strain 0.138 and initial steps.

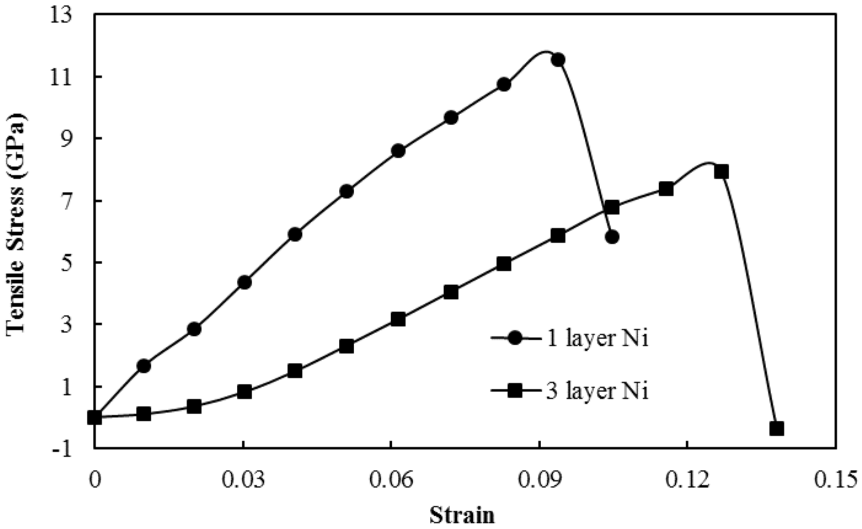

Figure 5.5. Tensile stress-strain curves of ZrO_2(111)/Ni (111) interfaces with Ni slabs of 1 and 3 layers.

a thin Ni layer interface model has higher strength or work of adhesion. In terms of deformation strain, the 3-layer Ni interface is more ductile as illustrated with larger tensile strain. This can be interpreted by the atom displacement vectors between the final and initial steps of the nanoscale tensile calculation, as shown in Figure 5.3(d) and Figure 5.4(d). As shown in Figure 5.4(d), the atom displacement of Ni atoms at the interface are larger than that of Zr and O atoms in 3-layer Ni interface model, indicating most of the deformation occurs among Ni layers in the 3-Ni-layers model. In the 1-layer Ni interface model, the displacement of Ni, Zr and O atoms are arbitrarily distributed, but the total outcome of these displacement extends the model in the tensile direction. The 3-layer Ni interface possesses more deformation compatibility than 1-layer Ni interface, suggesting a thick Ni interface can provide extra deformation to accommodate tensile strain.

(2) Shear Deformations Along {111}<110> and {111}<11$\bar{2}$> Directions

The atomic configurations of 1-layer Ni slab model during shear deformations along {111}<110> and {111}<11$\bar{2}$> directions are shown in Figure 5.6, and Figure 5.7, respectively. The calculated shear stress-strain curves are given in Figure 5.8. Both the shear modulus (43.9 GPa) and ultimate shear strength (7.9 GPa) along {111}<110> direction are greater than those along {111}<11$\bar{2}$> direction (30.9 GPa for shear modulus and 6.0 GPa for ultimate shear strength). Therefore, {111}<11$\bar{2}$> is a favorable shear slip system in this ZrO_2 (111)/Ni (111) interface system, which is different from pure Ni. It is also noted that the ductility of {111}<110> measured by strain, 0.23, is lower than that of {111}<11$\bar{2}$>, 0.27.

The shear deformations along {111}<110> and {111}<11$\bar{2}$> directions of the 3-layer Ni model are shown in Figure 5.9 and Figure 5.10, respectively. The calculated shear stress-strain curves are given in Figure 5.11. Similar to the 1-layer Ni model, for the 3-layer Ni, both the shear modulus (30.4 GPa) and ultimate shear strength (3.0 GPa) along {111}<110> direction are greater than those along {111}<11$\bar{2}$> direction (17.3 GPa for shear modulus and 1.8 GPa for ultimate shear strength). Therefore, {111}<11$\bar{2}$> is again a favorable shear slip system. Again, the ductility of {111}<110> measured by strain, $\sim$0.10, is lower than that of {111}<11$\bar{2}$>, $\sim$0.11.

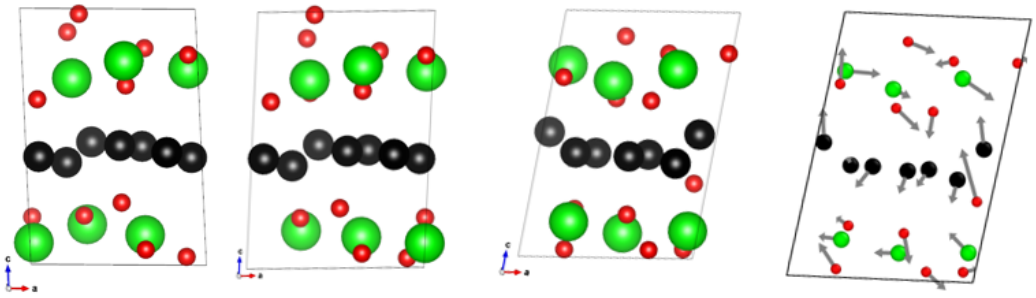

(a) (b) (c) (d)

Figure 5.6. Figure 5.6 Shear deformation model with 1-layer Ni along {111}<110> direction after relaxation: (a) initial position, (b) strain 0.126, (c) strain 0.230, and (d) atom displacement vectors between strain 0. 230 and initial steps.

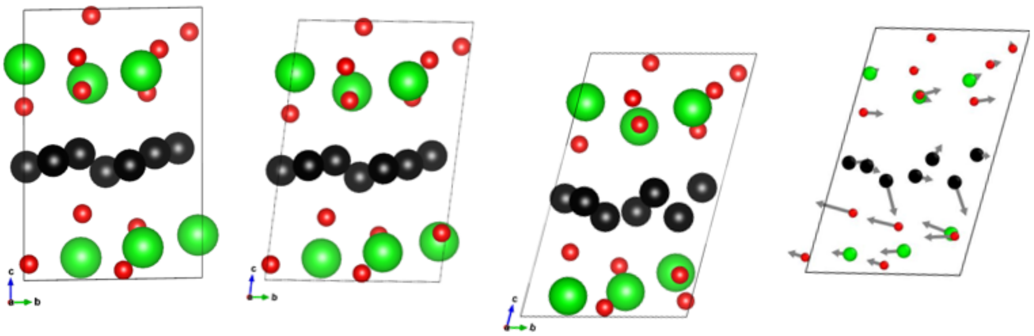

(a) (b) (c) (d)

Figure 5.7. Figure 5.7 Shear deformation model with 1-layer Ni along {111}<11$\bar{2}$> direction after relaxation: (a) initial position, (b) strain 0.126, (c) strain 0.267, and (d) atom displacement vectors between strain 0.267 and initial step.

The atom displacement vectors between the final and initial step of shear deformation models are plotted in Figure 5.6(d), Figure 5.7(d), Figure 5.9(d) and Figure 5.10(d). In the 1-layer Ni interface models, there is no obvious difference for the displacement vectors between Ni, Zr and O atoms, as shown in Figure 5.6(d) and Figure 5.7(d). However, the displacement directions between upper and lower

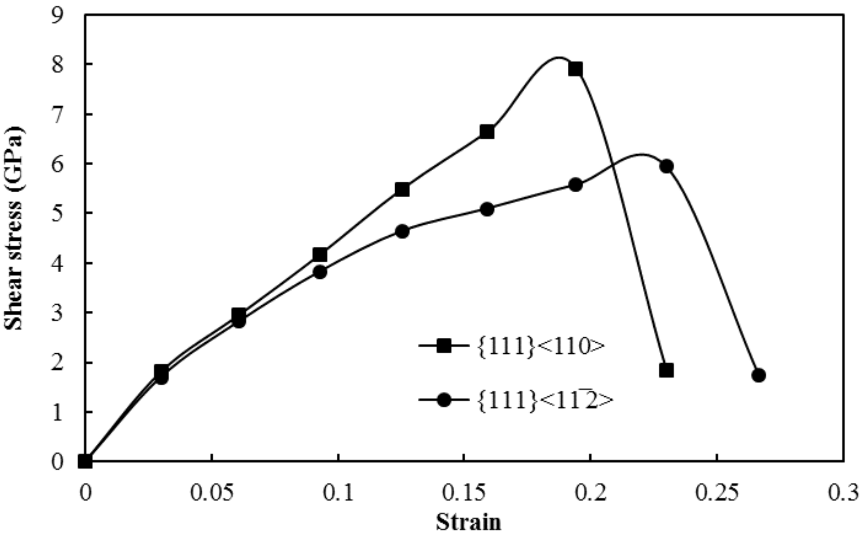

Figure 5.8. Calculated shear stress-strain curves of 1-layer Ni shear deformation model.

ZrO_2/Ni interface are in opposite trend, which properly illustrates the shear deformation. As shown in Figure 5.9(d) and Figure 5.10(d), the 3-layer Ni interface models show larger displacement in the Ni layers than that in the ZrO_2 layers, indicating that the Ni layers provide the most deformation in these interface models.

Comparing with the 1-layer Ni shear deformation model, the shear modulus and strengths in the 3-layer model are much lower by 40 %. This is because the shear deformation is primarily achieved by the deformation of Ni atoms. A thicker Ni layer allows to deformation at lower stress level.

In addition to stress, toughness can be used to measure the interfacial strength in large deformations. Toughness is calculated by integrating the are below the stress-strain curve. As shown in Table 5.1, the 1-layer Ni interface model has higher toughness than the 3-layer Ni model for both tensile and shear deformations. This is also consistent with the results from the adiabatic work of adhesion in section 3.1. In addition, the toughness in {111}<110> system is higher than that of {111}<11$\bar{2}$> direction for both 1-layer and 3-layer Ni models, primarily due to higher shear modulus and ultimate shear strength in the {111}<110> system. It also suggests that the

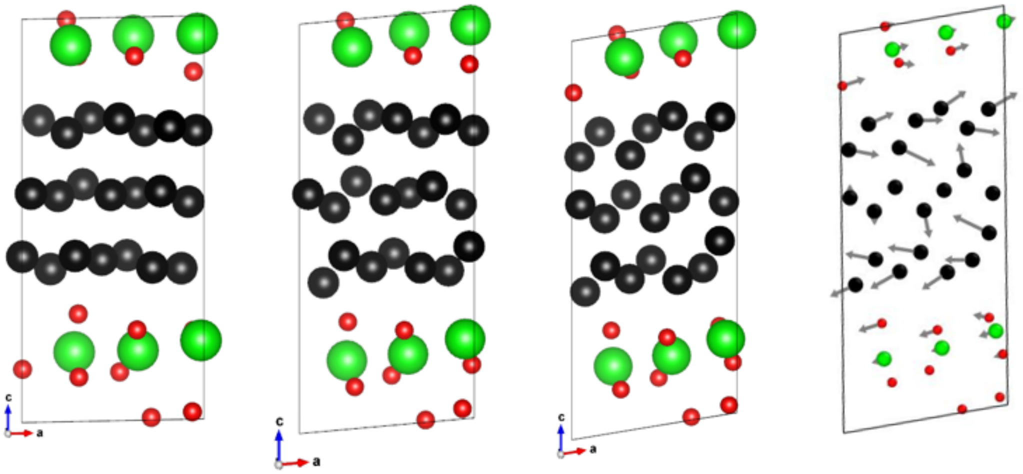

(a) (b) (c) (d)

Figure 5.9. Shear deformation model with 3-layer Ni along {111}<110> direction after relaxation: (a) initial position, (b) strain 0.051, (c) strain 0.105, and (d) atom displacement vectors between strain 0.105 and initial steps.

{111}<110> direction is stronger than that of {111}<11$\bar{2}$> direction during interface fracture.

Since most interfacial deformation is achieved by Ni atoms, it is worthy to compare the interfacial models with pure Ni. Ogata et al. calculated the shear stress-strain curves of pure Ni in {111}<11$\bar{2}$> direction using the DFT calculations [176]. The calculated ultimate strength is 5.1 GPa. It is similar to the 1-layer Ni interface model in this work, 6.0 GPa. However, the shear modulus in Ogata' s work is ~60.3 GPa, which is larger than that in this work, 30.9 GPa. Comparing to experimental data, Young' s modulus of polycrystalline Ni (190 – 220 GPa) [177] is also much higher than that of ZrO_2/Ni interface calculated in this work (139.9 GPa for 1-layer and 60.2 GPa for 3-layer Ni). Both elastic modulus and the ultimate strength values decrease as the increase of the Ni layer thickness. These comparisons suggest that the strength of the ZrO_2/Ni interface is substantially different from its pure component, and is determined by the Ni layer thickness.

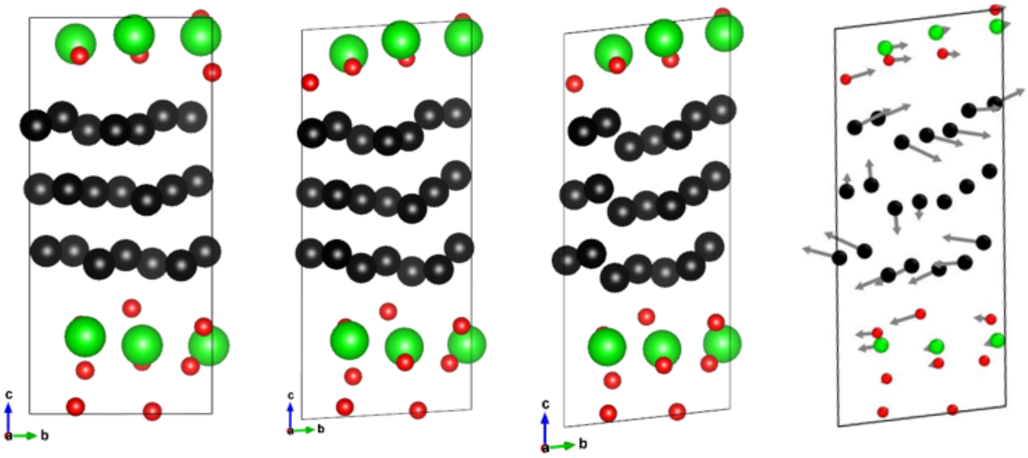

(a) (b) (c) (d)

Figure 5.10. Shear deformation model with 3-layer Ni along $\{111\}<11\bar{2}>$ direction after relaxation: (a) initial position, (b) strain 0.062, (c) strain 0.116 and (d) atom displacement vectors between strain 0.116 and initial steps.

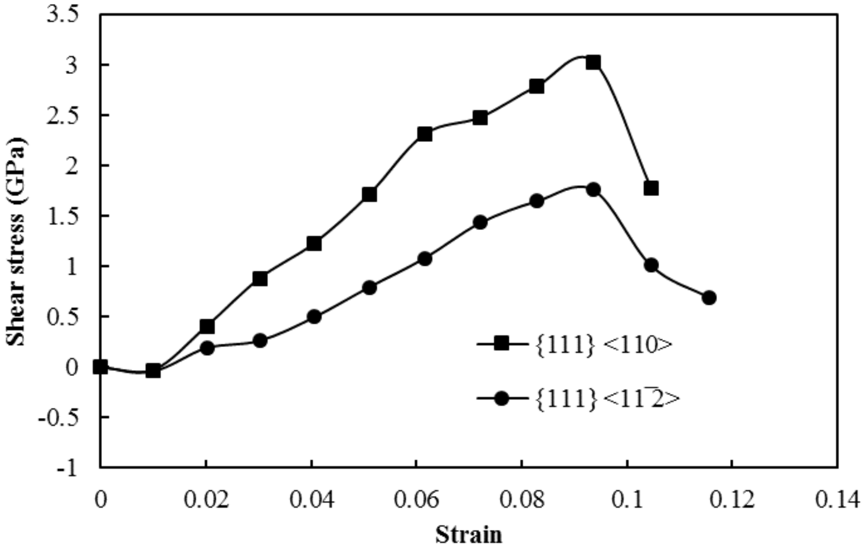

Figure 5.11. Calculated shear stress-strain curves of 3-layer Ni shear deformation model.

Table 5.1. Calculated elastic modulus, ultimate strength, and toughness.

Deformation mode, stress direction, and number of Ni layers	**Elastic modulus (GPa)**	**Ultimate tensile/shear strength (GPa)**	**Toughness (MJ/m^3)**
Tensile [111] 1-layer Ni	139.9	11.6	0.728
Tensile [111] 3-layer Ni	60.2	7.9	0.486
Shear {111}<110> 1-layer Ni	43.9	7.9	1.040
Shear {111}<110> 3-layer Ni	30.4	3.0	1.038
Shear {111}<$11\bar{2}$> 1-layer Ni	30.9	6.0	0.166
Shear {111}<$11\bar{2}$> 3-layer Ni	17.3	1.8	0.096

5.3.3 Charge Density and Bader Charge Analyses

The contours of charge density distribution are plotted in Figure 5.12. As shown in the figure, it is clear that the 1-layer Ni interface models (Figure 5.12(a), Figure 5.12(b), and Figure 5.12(c)) have stronger O–Ni bonds than the 3-layer Ni cases (Figure 5.12(d), Figure 5.12(e), and Figure 5.12(f)). This is the reason why the 1-layer Ni interface models have higher elastic modulus and strength. The electron localization function (ELF) can be used to describe the electron localization status and bonding behaviors, which depends on the electron density, gradient, and the kinetic energy density [178, 179]. Typically the value of ELF ranges from 0 to 1, which specifies vacuum to perfect localization of the electrons. A higher ELF value in the ELF graph indicates the electron are more localized. Metallic bonding in the ELF graph typically shows electron vacuum near the atom nucleus and a relatively high electron localization value at area far from the atom nucleus. Figure 5.13 shows the ELF graph of 1-layer and 3-layer Ni shear {111}<110> interface models, ELF graph in other tensile and shear cases shows the similar trend. The ELF of 3-layer Ni model shows electron vacuum near the Ni atom, however, it has a comparatively higher electron localization value in space far from the Ni atom. The Ni layers in the interface model show the typical metallic bonding characteristics, which can accommodate the deformation during the tensile and shear process. This is consistent with the above discussions that thicker Ni layer results to lower elastic modulus and lower ultimate strength.

As shown in Figure 5.13, the O and Zr atoms have higher ELF values than that of the Ni atoms in both 1-layer and 3-layer Ni interface models. The chemical bonding between the O and Ni atom at the interface shows an ionic bonding feature. In addition, both ELF graphs show a delocalized electron gap between ZrO_2 and Ni layer, suggesting the ionic bonding might be weaker than the metallic bonding in Ni layer, which has higher ELF value than ionic bonding. During the tensile and shear processes, the ionic bonding becomes weaker and weaker, until it breaks. Because 1-layer Ni models have stronger ionic bonding than that of 3-layer Ni models, as shown in Figure 5.12 of the charge density distribution contour, the 1-layer Ni interface models possess higher ultimate strength than that of the 3-layer Ni counterpart.

To get more quantitative measurements about bond characteristics, the average Bader charge numbers, including O, Zr, Ni ions, and the difference between O and Ni ions for both tensile and shear deformations, are summarized in Table 5.2. It is clear that the O and Ni differences, the average Bader charge difference between O and Ni ions of 1-layer Ni interface are consistently larger than those of 3-layer Ni interface in both tensile and shear cases. The Bader charge analysis results are also consistent with the charge density distributions in Figure 5.12. A larger average Bader charge difference indicates a stronger interaction between O and Ni, or more interaction between ZrO_2 and Ni. This explains the higher ultimate strength and

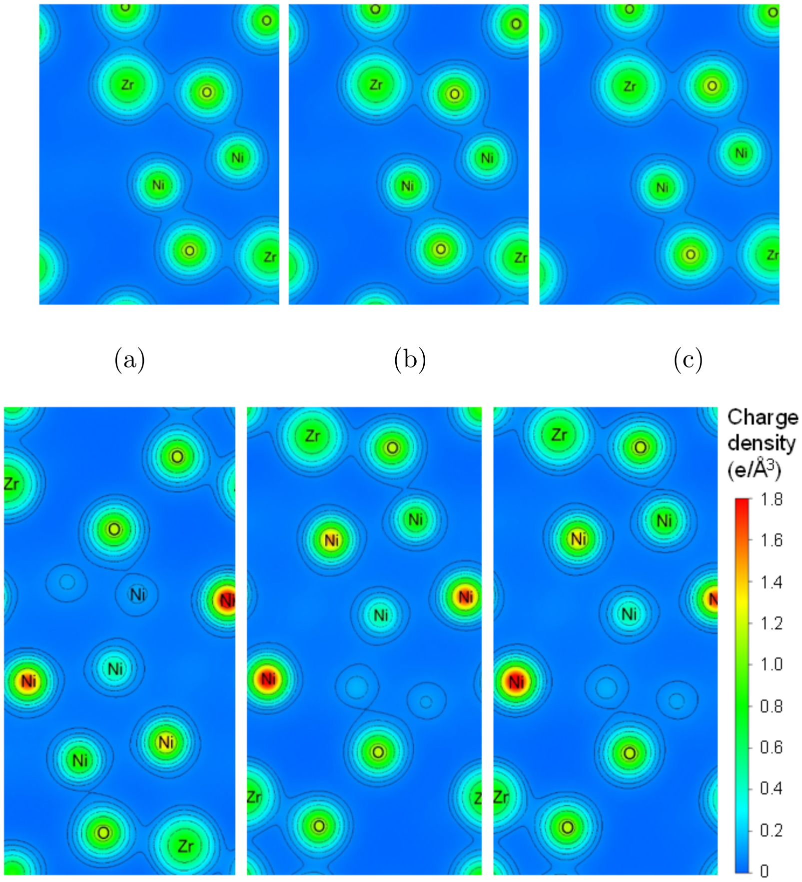

(a) (b) (c)

(b) (b) (c)

Figure 5.12. Charge density distributions in logarithmic scale: (a) tensile <111> with 1-layer Ni, (b) shear {111}<110> with 1-layer Ni, (c) shear {111}<11$\bar{2}$> 1-layer Ni, (d) tensile <111> with 3-layer Ni, (e) shear {111}<110> 3-layer Ni, (f) shear {111}<11$\bar{2}$> 3-layer Ni.

elastic modulus in the thin Ni layer interface than in the thick Ni layer interface, as listed in Table 5.1.

From the calculated mechanical properties of ZrO_2/Ni ceramic-metal interface, the layer thickness of bond coat film, NiCrAlY, at the interface makes a major impact on the coatings mechanical behavior. Typically, fracture or delamination in as-sprayed TBC system occurs near the interfaces between the top and bond coats [54, 125]. Therefore, the mechanical properties near the interface are important to enhance the

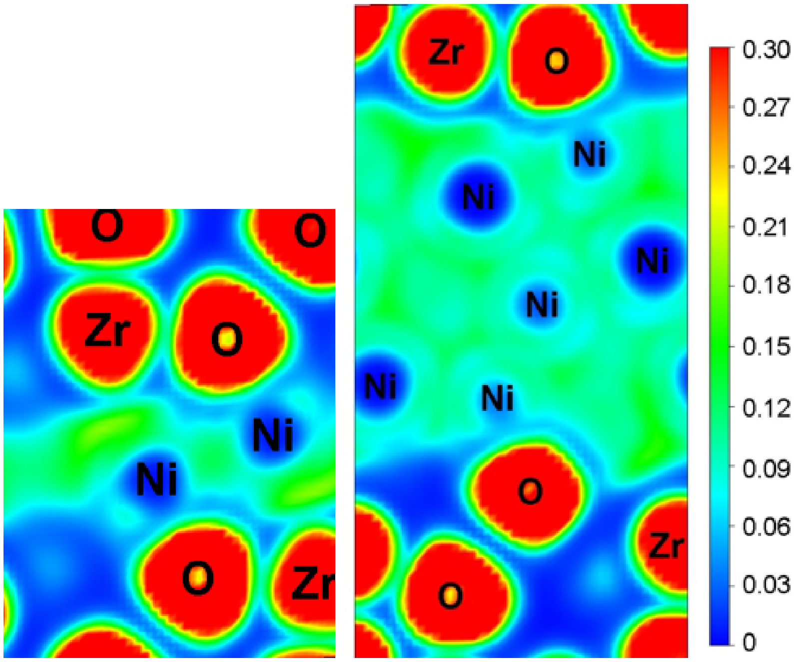

(a) (b)

Figure 5.13. ELF graph in the (a) shear {111}<110> 1-layer Ni interface model, (b) shear {111}<110> 3-layer Ni interface model.

lifetime performance of TBC system. Higher toughness and elastic modulus at the interface enhance the ability of fracture resistance to impede crack propagations in the ceramic top coat near the interface. From the theoretical analyses of this work, the ultimate tensile and shear strength are decreased with the increase of the bond coat film thickness at the interface, which means a thicker thickness of bond coat in TBC system corresponds to a weaker adhesion strength. On the other hand, a thin bond coat film will deteriorate the oxidation resistance of the TBC system. Therefore, the thickness of bond coat should be properly optimized to design and fabricate robust TBC systems.

Table 5.2. Average Bader charge number (e).

Deformation mode, stress direction, and number of Ni layers	**O**	**Zr**	**Ni**	**Difference between O and Ni**
Tensile [111] 1-layer Ni	1.258	-2.457	-0.050	1.308
Tensile [111] 3-layer Ni	1.264	-2.459	-0.019	1.283
Shear {111}<110> 1-layer Ni	1.252	-2.451	-0.045	1.297
Shear {111}<110> 3-layer Ni	1.266	-2.462	-0.019	1.285
Shear {111}<11$\bar{2}$> 1-layer Ni	1.257	-2.460	-0.046	1.303
Shear {111}<11$\bar{2}$> 3-layer Ni	1.265	-2.460	-0.019	1.284

5.4 MD Tensile and Shear Simulations of ZrO_2/Ni Interface Model

The DFT calculation is performed at the ground energy state of the atomic system, which means the DFT theoretical result is limited at very low temperatures (close to 0 K). Therefore, the MD method was performed to simulate the nanoscale tensile and shear process of ZrO_2/Ni interface model at high temperatures. LAMMPS code was used to conduct all of the MD calculations in this work. The charge-optimized many body potential (COMB3) was applied to describe the interatomic force field of the ZrO_2/Ni interface [180]. In COMB potential series (including both COMB and COMB3), the total potential energy U^{tot} of system is described by:

$$U^{tot}(r,q) = U^{es}(r,q) + U^{short}(r,q) + U^{vdW}(r) + U^{corr}(r) \tag{5.2}$$

where r represents the coordinate array of the system and q represents the charge array. U^{es} represents the electrostatic energies that include the energies to form a charge on an atom, the charge-nuclear interaction, the charge-charge interaction and the energies related with atomic polarizability. U^{short} is the short-range interaction energies that describe the pairwise repulsive and attractive potentials. The long-range van der Waals interactions (U^{vdW}) is described using Lennard-Jones expression. The energy corrections term (U^{corr}) were used to optimize the total energy.

To validate the COMB3 potential in the ZrO_2/Ni interface system, the lattice constants of ZrO_2 unit cell and Ni unit cell were calculated using MD model, respectively. Cubic ZrO_2 with a space group $Fm3m$ and cubic Ni of the same space group were used to calculate the lattice constant. The DFT calculation methods were similar to the one used in LZ unit cell model, except different cutoff energy and Brillouin zone k-point scheme. The cutoff energy for ZrO_2 and Ni were 500 eV and 300 eV, respectively, and the 5×5×5 Monkhost-Pack scheme was used for both ZrO_2 and Ni as Brillouin zone k-point. Table 5.3 lists the DFT and MD calculation results of the ZrO_2 and the Ni lattice constants. The error difference between MD results and DFT results for ZrO_2 and Ni are 1.478 % and 0.378 %, respectively, suggesting that the COMB3 potential is reliable in single material ZrO_2 or Ni MD models.

The ZrO_2/Ni interface MD models were built based on the DFT model as described in section 5.2, and the lattice mismatch was less than 3%. The work of adhesion of ZrO_2(111)/Ni(111) interface was calculated according to Equation (5.1) using MD method, and it was compared with the DFT results. The calculated work of adhesion results are listed in Table 5.3 and plotted in Figure 5.14. The MD-calculated work of adhesion results have the same trend as DFT results, which is acceptable in the interface simulations.

The tensile stress-strain curves of the ZrO_2/Ni interface model were calculated using the same scheme as LZ model. However, the shear stress and strain values here were calculated from the single direction pure shear deformation. Therefore, the shear

Table 5.3. DFT and MD calculated lattice constant and work of adhesion results.

	DFT-calculated result	**MD-calculated result**
Lattice constant ZrO_2 (Å)	5.146	5.070
Lattice constant Ni (Å)	3.514	3.527
Work of adhesion with 1 layer ZrO_2 (mJ/m^2)	629	751
Work of adhesion with 2 layer ZrO_2 (mJ/m^2)	554	602
Work of adhesion with 3 layer ZrO_2 (mJ/m^2)	296	378

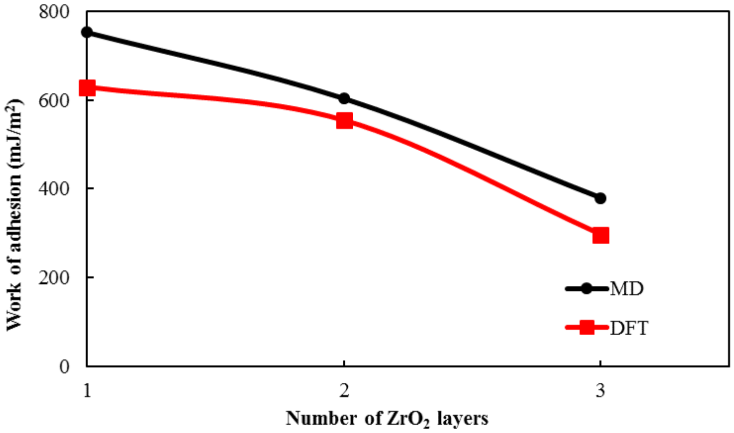

Figure 5.14. Comparison of work of adhesion between DFT and MD models.

strain was represented by the deformation angle, and shear stress was calculated from the elastic constants.

The MD models of the ZrO_2(111)/Ni(111) interface before and after the tensile simulation are shown in Figure 5.15. The periodic boundary condition was applied in all 3 dimensions of this tensile model, so the ZrO_2-Ni-ZrO_2 sandwich model was built to match the periodic condition in the tensile direction. As shown in Figure 5.15(b), the Ni layer in the model with 0.16 tensile strain does not keep the initial lattice array, suggesting that the primary deformation comes from the Ni layer.

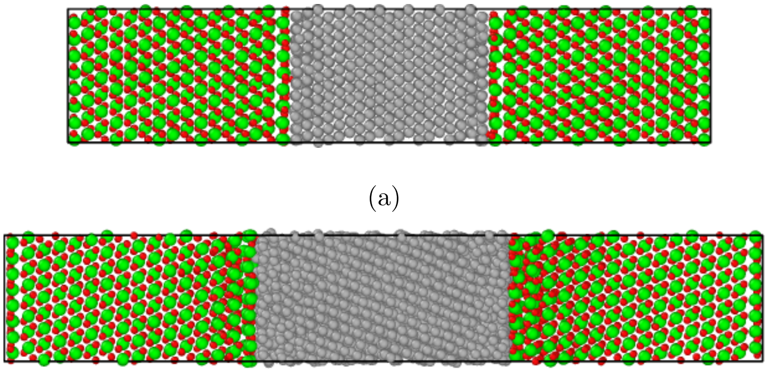

(a)

(b)

Figure 5.15. MD ZrO_2(111)/Ni(111) interface model in tensile simulations at 300 K (a) initial position with 0 strain (b) the position of tensile strain 0.16, Green, red, and grey balls represent Zr, O, and Ni atom, respectively (same coloring schemes are used in all of the MD figures afterwards).

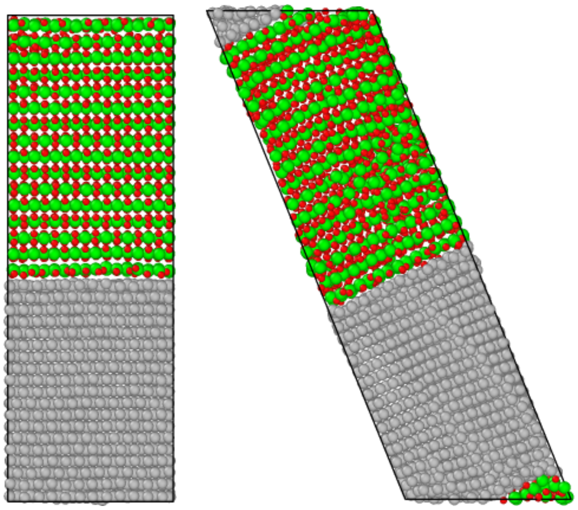

(a)

(b)

Figure 5.16. MD ZrO_2(111)/Ni(111) interface model in shear simulation in {111}<110> direction (a) initial position with 0 strain (b) the position of shear strain 0.35.

The MD ZrO_2(111)/Ni(111) interface model used in the shear simulation of {111} <110> direction at 300 K are shown in Figure 5.16. The non-periodic boundary conduction was applied in the shear direction, and the periodic boundary condition was used in the other two dimensions.

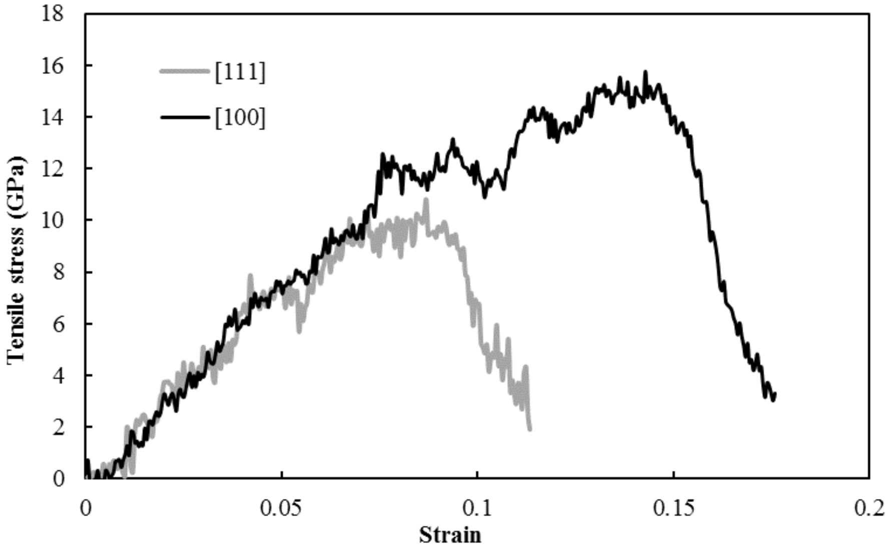

Figure 5.17. Tensile stress-strain curves of ZrO_2/Ni interface at 300 K.

The tensile stress-strain curves of ZrO_2(111)/Ni(111) interface model in [111] direction and ZrO_2(100)/Ni(100) model in [100] direction at 300K are shown in Figure 5.17. The tensile curve in [111] direction reaches its ultimate strength of ∼15 GPa at the strain of ∼0.143. The MD-calculated ultimate strength is in the similar level but larger than the DFT-calculated results (The DFT results are shown in Figure 5.5). The undulation of the curve is due to the limitation of the atom numbers. The average Young's modulus in [111] direction is 131.56 GPa, which is similar as the DFT result of 1 Ni-layer interface model as listed in Table 5.1 (139.9 GPa). The average Young's modulus in [100] direction is 127.85 GPa, which is slightly lower than that in [111] direction. However, the ultimate strength in [100] direction is only ∼10 GPa, which is about two thirds of that in [111] direction, indicating that the mechanical strength of ZrO_2/Ni interface in [111] direction is much stronger than that in [100] direction.

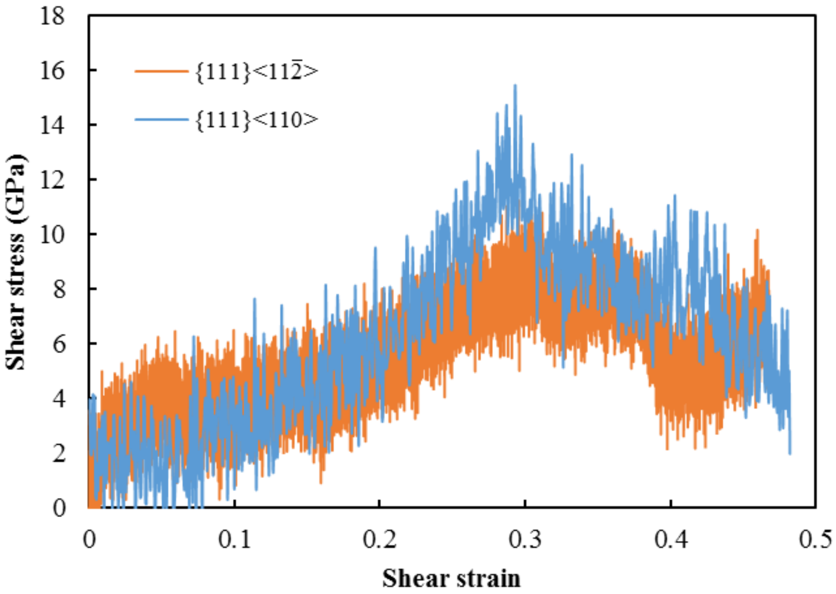

Figure 5.18. Shear stress-strain curves of ZrO_2/Ni interface at 300 K.

The shear stress-strain curves in {111}<11$\bar{2}$> and {111}<110> directions at 300K are shown in Figure 5.18. These two curves share the similar shear stress-strain trend as the thin-Ni-layer DFT results (The DFT results are shown in Figure 5.8). The ultimate shear strength in {111}<11$\bar{2}$> direction is ~9 GPa at the shear strain of ~0.31. The average shear modulus in {111}<11$\bar{2}$> direction is ~29.4 GPa. The ultimate shear strength in {111}<110> direction is ~12 GPa at the shear strain of ~0.29. The average shear modulus in {111}<110> is ~34.5 GPa. The ultimate strength is larger than the DFT-calculated results, as listed in Table 5.1. The shear modulus is similar to the DFT-calculated results. The differences of ultimate strength and elastic modulus between the DFT and the MD results are due to the differences of dimension scale and atom number. In addition, the MD calculation is performed in a dynamic equilibration, and the DFT calculations are conducted in the static equilibration of each tensile steps.

5.5 Summary

The ideal tensile strength and shear strength of ZrO_2/Ni ceramic-metal interface are calculated using the DFT and MD methods. The major conclusions are summarized as the following aspects.

For tensile deformation in [111] direction, Young's moduli of the 1-layer Ni and 3-layer Ni metal-ceramic models are 139.9 GPa and 60.2 GPa, respectively; the ultimate tensile strengths are 11.6 GPa and 7.9 GPa, respectively; the toughnesses are 0.728 MJ/m^3 and 0.486 MJ/m^3, respectively. The 1-layer Ni model shows higher mechanical strength than the 3-layer Ni model in tensile deformation.

For shear deformation in $\{111\}<110>$ system, the shear moduli of the 1-layer Ni and 3-layer Ni M-C models are 43.9 GPa and 30.4 GPa, respectively; the ultimate shear strengths are 7.0 GPa and 3.0 GPa, respectively; the toughnesses are 1.040 MJ/m^3 and 1.038 MJ/m^3, respectively. The 1-layer Ni model shows higher mechanical strength than the 3-layer Ni model in shear deformation.

For shear deformation in $\{111\}<11\bar{2}>$ system, the shear moduli of the 1-layer Ni and 3-layer Ni metal-ceramic models are 30.9 GPa and 17.3 GPa, respectively; the ultimate shear strengths are 6.0 GPa and 1.8 GPa, respectively; the toughnesses are 0.166 MJ/m3 and 0.096 MJ/m3, respectively.

Both charge distribution and Bader charge analyses show that the 1-layer Ni ceramic-metal model has stronger interaction between Ni and O ions than that of the 3-layer Ni model, which explains the higher mechanical properties in 1-layer Ni model from the calculated tensile and shear stress-strain results.

From the theoretical analyses of this work, the ultimate tensile and shear strength are decreased with the increase of the bond coat film thickness at the interface, which means a thicker thickness of bond coat in TBC system corresponds to a weaker adhesion strength. On the other hand, a thin bond coat film will deteriorate the oxidation resistance of the TBC system. Therefore, the thickness of bond coat should be properly optimized to design and fabricate robust TBC systems.

CHAPTER 6. CONCLUSIONS

6.1 Summary of Major Conclusions

Lanthanum zirconate is proposed as a promising thermal barrier coating material due to its outstanding phase stability in high temperature and lower thermal conductivity than the commercial 8YSZ TBCs material. In this work, the layered LZ TBC (SCL LZ coatings with porosity range from 11.81 % to 16.52 % and DCL LZ/8YSZ coatings with LZ porosity of 11.54 %) and composite LZ/8YSZ TBCs were designed and deposited using APS method. The physical, mechanical and thermal properties of LZ coating were investigated through experiments and multi-scale modeling techniques. The thermal cycling tests of LZ-based coatings were performed to investigate the thermal durability performance. The tensile and shear nanoscale simulations of interface model were conducted to give an insight of the TBC's delamination. The primary conclusions of this dissertation are summarized as following aspects.

1. The mechanical properties of the layered LZ-based TBCs, such as hardness and Young's modulus, were investigated using Vickers microhardness and nanoindentation. The Vickers hardness of SCL LZ is in the range of 3.90 – 4.22 GPa. On the other hand, the nanoindentation shows the nanohardness of the SCL LZ is in the range of 5.41 – 6.08 GPa, and the corresponding Young's modulus is calculating from the nanoindentation data with the value range of 89.0 – 104.3 GPa. The porosity of the LZ coating has a big influence on the hardness and Young's modulus. The hardness and Young's modulus decrease with the increase of the LZ coating porosity.

2. Bond strength test is used to study the adhesion bond strength between the top coat and bond coat. The measured adhesion strength of the as-sprayed SCL LZ coating is about 10.48 MPa, which is lower than the adhesion strength of the SCL 8YSZ coating (13.59 MPa). After thermal spray process, the thermal residual

stress is generated in the TBC system. From the theoretical thermal residual stress calculation, the SCL LZ coating has larger residual stress difference at the interface than that of 8YSZ coating due to the big CTE difference between LZ coating and the bond coat. In addition, the LZ has lower fracture toughness than the 8YSZ, indicating that the crack propagation in LZ is much easier than that in 8YSZ. The low fracture toughness of LZ also leads to the high erosion rate.

3. Thermal conductivity and CTE of the LZ coating with a porosity of 11.54 % were measured using the laser flash method and the dilatometry method, respectively. The thermal conductivity of the LZ coating is 0.59 – 0.68 W/m/K in a temperature range of 373 – 1173 K, which is about 25 % lower than that of the porous 8YSZ coating. The CTE values of the LZ are approximately $9-10\times10^{-6}$ /K in a temperature range of 400 – 600 K, which are about 10 % lower than that of the 8YSZ. The large CTE difference between the LZ and bond coat might lead to large thermal residual stress.

4. The furnace cycling test (FCT), heat treatments, and jet engine thermal shock test (JETS) are performed to investigated the thermal durability performance of LZ-based TBCs. The results show that all of the layered LZ coatings are delaminated within the first 20 cycles in FCT tests. The large thermal residual stress and low fracture toughens are the primary reason of LZ coating's delamination. In both the heat treatment and the JETS tests, the double-layer coating with porous 8YSZ and LZ layers exhibits a better performance than other layered LZ-based coating, suggesting that porous 8YSZ can be used as a buffer layer for increasing the lifetime in thermal cycling tests. On the other hand, the composite LZ/YSZ TBC samples have a big improvement in the FCT tests because the CTE difference between top and bond coats are reduced by the composite coatings and buffer layer. The double layer composite coating (50 % LZ/50 % 8YSZ and 25 % LZ/75 % 8YSZ) with 8YSZ buffer layer shows the best thermal durability performance in both FTC and JETS among all the LZ-based TBCs.

5. The thermal gradient mechanical fatigue (TGMF) test was performed to investigate the thermal-mechanical coupled stability. The LZ TBCs samples have fewer

cycles than 8YSZ. The large CTE difference between LZ topcoat and bond coat leads to high thermal residual stress, which is accumulated during the TGMF test process. Delamination occurs at the interface of the LZ top coat and bond-coat.

6. The DFT and the MD calculations are effective techniques to investigate the intrinsic physical, mechanical and thermal properties of various materials. The LZ unit cell is geometrically optimized by minimization of the total energy using the DFT calculations. The calculated lattice parameter is 10.875 Å. The nanoscale tensile and shear simulations are conducted based on the optimized LZ unit cell using the DFT and the MD method. The elastic modulus, ultimate strength, and toughness are calculated based on the stress-strain curves. The anisotropic Young's modulus is calculated using two different approaches: (1) the tensile stress-strain relation in large deformation, and (2) the elastic constant analysis in elastic deformation. The largest Young's modulus is located in [111] direction of LZ unit cell. The anisotropic Young's modulus is related to the bonds between cation and anion, which are investigated by the electronic charge distribution and charge transfer analysis.

7. The thermal properties such as specific heat capacity and thermal conductivity are investigated using DFT, MD, and FE methods. The specific heat of LZ unit cell is 0.4 – 0.46 J/g/K at a temperature range of 673 – 1673 K, which is computed using the DFT calculations. The thermal conductivities of LZ single crystal and porous LZ coating are calculated using multiscale modeling techniques, which was based on the MD and the image-based FE methods. The thermal conductivities of the single crystal LZ is calculated using the MD method, whose values are 1.25 – 1.39 W/m/K in a temperature range of 473 – 1273 K. The thermal conductivities of polycrystalline LZ coating are calculated using the SEM image-based FE method, whose values are 0.46 – 0.59 W/m/K at a temperature ranges of 473 – 1273 K. The calculated specific heat and thermal conductivity results have a good accuracy, comparing with the experimental results.

8. The tensile and shear stress-strain conditions at the interface of top and bond coat have a big influence on the thermal and mechanical durability of the LZ coating,

so the nanoscale tensile and shear simulations are performed using the DFT calculations. The ZrO_2/Ni interface model is chosen as a feasible simplification model to mimic the interface of top and bond coat. Both of Young's modulus and shear modulus values of the interface ZrO_2/Ni model are decreased with the increase of the Ni layer thickness, so as the ultimate strength and the toughness.

6.2 Contributions of This Thesis Work

This dissertation systematically investigated the LZ-based coating in both experimental and modeling approaches. The major contributions of this thesis are summarized as following aspects.

1. The layered LZ-based TBC is designed and deposited using APS technology. The porous 8YSZ is proposed as a good buffer layer to improve the thermal durability of LZ-based TBC.

2. This work proposes a double layer composite LZ/8YSZ coating materials with the porous 8YSZ buffer layer, which greatly improves the thermal stability of the LZ-based TBC.

3. In this work, the nanoscale tensile and shear stress-strain calculations of LZ material are performed for the first time. The anisotropic Young's modulus is calculated.

4. The thermal conductivities of single crystal and polycrystalline LZ are calculated using the MD method and the image-based FE method for the first time, which provides a good method to predict the thermal conductivity of TBCs.

5. The tensile and shear nanoscale simulations of ZrO_2/Ni interface are performed to understanding the stress-strain status at the interface area, which also give us an idea about the relation between the interface layer thickness and elastic modulus.

6.3 Recommendation for Future Work

In this work, the physical, mechanical and thermal properties of lanthanum zirconate based thermal barrier coatings are systematically studied. The powder fabrication, deposition technique, microstructure morphology, physical, thermal and mechanical properties, thermomechanical durability and failure mechanisms of LZ coating are discussed. Since the TBC is a quite complicated composite material system, there are many factors related to the TBC's properties and durability, for instance: the coating material species, deposition technique, coating porosity, cracks and pore morphology, grain size, dope element choice, coating thickness, heat treatment method, multiple layer coating architecture and so on. The research on the LZ-based TBC is still far from the end. Based on this dissertation, there are several issues of LZ, which need to be solved before it can be accepted as a TBC material.

The LZ possesses a lower fracture toughness as shown in Table 1.1. The low fracture toughness leads to the initiation and propagation of the micro-cracks even at a very low-stress level. The vulnerability of the LZ for the fracture propagation harms its thermal durability. It becomes very important to improve the fracture toughness of the LZ-based coatings. Although the composite material and the graded layered structure help to improve the durability performance in thermal cycling test, some artificial defects also introduce into the TBC systems, which might reduce the lifetime of the coating. Doping some other element might be a feasible way to improve the fracture toughness of LZ coating. But, the doping element and the doping ratio are still unclear, which requires further investigations.

The thermal conductivity can be reduced and the coefficient of thermal expansions can be increased by doping other elements. However, the material that has better thermal properties does not guarantee a good thermal cycling performance. The thermomechanical durability investigations about the low thermal conductivity material need to be further conducted.

The failure mechanisms of delamination of the LZ coatings in thermal cycling, mechanical fatigue cycles, and chemical corrosive environment are not totally clear. The combination of experimental techniques and theoretical modeling tools can be the most effective way to unfold the mystery of failure in the LZ-based TBCs. The modeling studies about the TGO initiation and growth, bond coating oxidation, and the crack propagation in the LZ coating are still challenging work, which will help to fully understand of those failure mechanisms and improve the design of the TBC coating.

Most of the mechanical test conducted in this dissertation are in room temperature. However, the high-temperature mechanical properties of the LZ-based TBCs might affect the thermal mechanical durability. The mechanical properties in high-temperature condition also need to be investigated.

The composite LZ/8YSZ TBC exhibits a better thermal durability performance than the traditional layered LZ-based TBCs, which provides a feasible direction for the future work. The architecture of the TBC and the species/ratio of the composite coat need to be improved to achieve better performance. In addition, the phase stability in high-temperature operation of the composite coating needs to be studied.

LIST OF REFERENCES

LIST OF REFERENCES

[1] D. Clarke and C. Levi. Materials design for the next generation thermal barrier coatings. *Annual Review of Materials Research*, 33(1):383–417, 2003.

[2] J. Perepezko. The hotter the engine, the better. *Science*, 326(5956):1068–1069, 2009.

[3] R. Miller. Thermal barrier coatings for aircraft engines: history and directions. *Journal of Thermal Spray Technology*, 6(1):35–42, 1997.

[4] R. Miller. Current status of thermal barrier coatings an overview. *Surface and Coatings Technology*, 30(1):1–11, 1987.

[5] N. Padture, M. Gell, and E. Jordan. Thermal barrier coatings for gas-turbine engine applications. *Science*, 296(5566):280–284, 2002.

[6] D. Clarke, M. Oechsner, and N. Padture. Thermal-barrier coatings for more efficient gas-turbine engines. *MRS Bulletin*, 37(10):891–898, 2012.

[7] W. Pan, S. Phillpot, C. Wan, A. Chernatynskiy, and Z. Qu. Low thermal conductivity oxides. *MRS Bulletin*, 37(10):917–922, 2012.

[8] S. Weber, H. Lein, T. Grande, and M. Einarsrud. Lanthanum zirconate thermal barrier coatings deposited by spray pyrolysis. *Surface and Coatings Technology*, 227(0):10–14, 2013.

[9] T. Taylor. Low thermal expansion bondcoats for thermal barrier coatings. *US Patent 7910225 B2*, 2011.

[10] J. Davis. *Handbook of thermal spray technology.* ASM international, 2004.

[11] W. Nelson and R. Orenstein. TBC experience in land- based gas turbines. *Journal of Thermal Spray Technology*, 6(2):176–180, 1997.

[12] P. Fauchais, J. Heberlein, and M. Boulos. *Thermal spray fundamentals: From powder to part.* Springer Science and Business Media, 2014.

[13] M. Chen, M. Glynn, R. Ott, T. Hufnagel, and K. Hemker. Characterization and modeling of a martensitic transformation in a platinum modified diffusion aluminide bond coat for thermal barrier coatings. *Acta Materialia*, 51(14):4279–4294, 2003.

[14] S. Sjöström, H. Brodin, and M. Jinnestrand. Thermomechanical fatigue life of a TBC-comparison of computed and measured behaviour of delamination cracks. In *ICF13*, 2013.

[15] R. Vassen, X. Cao, F. Tietz, D. Basu, and D. Stöver. Zirconates as new materials for thermal barrier coatings. *Journal of the American Ceramic Society*, 83(8):2023–2028, 2000.

[16] K. Schlichting, N. Padture, and P. Klemens. Thermal conductivity of dense and porous yttria-stabilized zirconia. *Journal of Materials Science*, 36(12):3003–3010, 2001.

[17] D. Hasselman, L. Johnson, L. Bentsen, R. Syed, H. Lee, and M. Swain. Thermal diffusivity and conductivity of dense polycrystalline ZrO_2 ceramics: a survey. *American Ceramic Society Bulletin*, 66(5):799–806, 1987.

[18] X. Cao, R. Vassen, W. Jungen, S. Schwartz, F. Tietz, and D. Stöver. Thermal stability of lanthanum zirconate plasma-sprayed coating. *Journal of the American Ceramic Society*, 84(9):2086–2090, 2001.

[19] Z. Lu, M. Kim, S. Myoung, J. Lee, Y. Jung, I. Kim, and C. Jo. Thermal stability and mechanical properties of thick thermal barrier coatings with vertical type cracks. *Transactions of Nonferrous Metals Society of China*, 24, Supplement 1(0):s29–s35, 2014.

[20] M. Subramanian, G. Aravamudan, and G. Subba Rao. Oxide pyrochlores a review. *Progress in Solid State Chemistry*, 15(2):55–143, 1983.

[21] M. Bolech, E. Cordfunke, A. Van Genderen, R. van der Laan, F. Janssen, and J. van Miltenburg. The heat capacity and derived thermodynamic functions of $La_2Zr_2O_7$ and $Ce_2Zr_2O_7$ from 4 to 1000 k. *Journal of Physics and Chemistry of Solids*, 58(3):433–439, 1997.

[22] D. Sedmidubsky, O. Benes, and R. Konings. High temperature heat capacity of $Nd_2Zr_2O_7$ and $La_2Zr_2O_7$ pyrochlores. *J. chem. Thermodynamics*, 37:1098–1103, 2005.

[23] K. Shimamura, T. Arima, K. Idemitsu, and Y. Inagaki. Thermophysical properties of rare-earth-stabilized zirconia and zirconate pyrochlores as surrogates for actinide-doped zirconia. *International Journal of Thermophysics*, 28(3):1074–1084, 2007.

[24] H. Tang, H. Sun, D. Chen, and X. Jiao. Fabrication and characterization of nanostructured $La_2Zr_2O_7$ fibers. *Material Letters*, 70:48–50, 2012.

[25] Y. Tong, Y. Wang, Z. Yu, X. Wang, X. Yang, and L. Lu. Preparation and characterization of pyrochlore $La_2Zr_2O_7$ nanocrystals by stearic acid method. *Materials Letters*, 62:889–891, 2008.

[26] T. Moriga, A. Yoshiasa, F. Kanamaru, K. Koto, M. Yoshimura, and S. Somiya. Crystal structure analyses of the pyrochlore and fluorite-type $Zr_2Gd_2O_7$ and anti-phase domain structure. *Solid State Ionics*, 31(4):319–328, 1989.

[27] D. Michel, M. Jorba, and R. Collongues. Study by raman spectroscopy of order-disorder phenomena occurring in some binary oxides with fluorite-related structures. *Journal of Raman Spectroscopy*, 5(2):163–180, 1976.

[28] Y. Tabira, R. Withers, L. Minervini, and R. Grimes. Systematic structural change in selected rare earth oxide pyrochlores as determined by wide-angle cbed and a comparison with the results of atomistic computer simulation. *Journal of Solid State Chemistry*, 153(1):16–25, 2000.

[29] W. Bragg and W. Bragg. The reflection of X–rays by crystals. *Proceedings of the Royal Society of London. Series A, Containing Papers of a Mathematical and Physical Character*, 88(605):428–438, 1913.

[30] F. Brown and P. Duwez. The systems zirconia-lanthana and zirconia-neodymia. *Journal of the American Ceramic Society*, 38(3):95–101, 1955.

[31] R. Roth. Pyrochlore-type compounds containing double oxides of trivalent and tetravalent ions. *Journal of Research of the National Bureau of Standards*, 56(1):17–25, 1956.

[32] M. Maloney. Thermal barrier coating systems and materials. *US Patents 6117560*, 2000.

[33] G. Di Girolamo, F. Marra, M. Schioppa, C. Blasi, G. Pulci, and T. Valente. Evolution of microstructural and mechanical properties of lanthanum zirconate thermal barrier coatings at high temperature. *Surface and Coatings Technology*, 268:298–302, 2015.

[34] J. Singh, F. Quli, D. Wolfe, J. Schriempf, and J. Singh. An overview: Electron beam-physical vapor deposition technology-present and future applications. *Applied Research Laboratory, Pennsylvania State University, USA*, 1999.

[35] Z. Xu, L. He, R. Mu, X. Zhong, Y. Zhang, J. Zhang, and X. Cao. Double-ceramic-layer tbc of $La_2Zr_2O_7$/YSZ deposited by electron beam-physical vapor deposition. *Journal of Alloys and Compounds*, 473:509–515, 2009.

[36] B. Saruhan, P. Francois, K. Fritscher, and U. Schulz. EB-PVD processing of pyrochlore-structured $La_2Zr_2O_7$-based TBCs. *Surface and Coatings Technology*, 182(23):175–183, 2004.

[37] K. Bobzin, N. Bagcivan, T. Brgelmann, and B. Yildirim. Influence of temperature on phase stability and thermal conductivity of single- and double-ceramic-layer EB-PVD TBC top coats consisting of 7YSZ, $Gd_2Zr_2O_7$ and $La_2Zr_2O_7$. *Surface and Coatings Technology*, 237(0):56–64, 2013.

[38] C. Wang, Y. Wang, L. Wang, G. Hao, X. Sun, F. Shan, and Z. Zou. Nanocomposite lanthanum zirconate thermal barrier coating deposited by suspension plasma spray process. *Journal of Thermal Spray Technology*, 23(7):1030–1036, 2014.

[39] S. Weber, H. Lein, T. Grande, and M. Einarsrud. Deposition mechanisms of thick lanthanum zirconate coatings by spray pyrolysis. *Journal of the American Ceramic Society*, 94(12):4256–4262, 2011.

[40] H. Lehmann, D. Pitzer, G. Pracht, R. Vassen, and D. Stöver. Thermal conductivity and thermal expansion coefficients of the lanthanum rare-earth-element zirconate system. *Journal of the American Ceramic Society*, 86(8):1338–1344, 2003.

[41] Standard test method for density, oil content, and interconnected porosity of sintered metal structural parts and oil-impregnated bearings, in ASTM 328-96, 1996.

[42] S. Myoung, J. Kim, W. Lee, Y. Jung, K. Lee, and U. Paik. Microstructure design and mechanical properties of thermal barrier coatings with layered top and bond coats. *Surface and Coatings Technology*, 205(5):1229–1235, 2010.

[43] R. Vassen, X. Cao, F. Tietz, G. Kerkhoff, and D. Stöver. $La_2Zr_2O_7-$ a new candidate for thermal barrier coatings. In *Proceedings of the United Thermal Spray Conference-UTSC99*, pages 830–834. DVS-Verlag, Dsseldorf, Germany, 1999.

[44] D. Zhu, N. Bansal, and R. Miller. Thermal conductivity and stability of HfO_2-Y_2O_3 and $La_2Zr_2O_7$ evaluated for 1650 °C thermal/environmental barrier coating applications. In *Proceedings of the 105th Annual Meeting and Exposition of the American Ceramic Society, The American Ceramic Society, Nashville, TN.*

[45] J. Nair, P. Nair, G. Doesburg, J. Ommen, J. Ross, A. Burggraaf, and F. Mizukami. Sintering of lanthanum zirconate. *Journal of the American Ceramic Society*, 82(8):2066–2072, 1999.

[46] J. Zhang, X. Guo, Y. Jung, L. Li, and J. Knapp. Quantitative analysis of pore morphology in lanthanum zirconate thermal barrier coating. In *Materials Science & Technology 2014 (MS&T)*. 2061-2068, 2014.

[47] S. Weber, H. Lein, T. Grande, and M. Einarsrud. Thermal and mechanical properties of crack-designed thick lanthanum zirconate coatings. *Journal of the European Ceramic Society*, 34(4):975–984, 2014.

[48] J. Zhang, X. Guo, Y. Jung, L. Li, and J. Knapp. Microstructural non-uniformity and mechanical property of air plasma-sprayed dense lanthanum zirconate thermal barrier coating. *Materials Today: Proceedings*, 1(1):11–16, 2014.

[49] Z. Xu, L. He, R. Mu, S. He, and X. Cao. Preparation and characterization of $La_2Zr_2O_7$ coating with the addition of Y_2O_3 by EB-PVD. *Journal of Alloys and Compounds*, 492(1-2):701–705, 2010.

[50] K. Jiang, S. Liu, G. Ma, and L. Zhao. Microstructure and mechanical properties of $La_2Zr_2O_7(Zr_{0.92}Y_{0.08})O_{1.96}$ composite ceramics prepared by spark plasma sintering. *Ceramics International*, 40(9, Part A):13979–13985, 2014.

[51] G. Beshish, C. Florey, F. Worzala, and W. Lenling. Fracture toughness of thermal spray ceramic coatings determined by the indentation technique. *Journal of Thermal Spray Technology*, 2(1):35–38, 1993.

[52] G. Anstis, P. Chantikul, B. Lawn, and D. Marshall. A critical evaluation of indentation techniques for measuring fracture toughness: I, direct crack measurements. *Journal of the American Ceramic Society*, 64(9):533–538, 1981.

[53] Y. Wang. *The improvement of thermal and mechanical properties of* $La_2Zr_2O_7$*-based pyrochlores as high temperature thermal barrier coatings.* Thesis, 2013.

[54] X. Guo, Z. Lu, Y. Jung, L. Li, J. Knapp, and J. Zhang. Thermal properties, thermal shock, and thermal cycling behavior of lanthanum zirconate-based thermal barrier coatings. *Metallurgical and Materials Transactions E*, 3(2):64–70, 2016.

[55] Q. Hong. *Methods for melting temperature calculation.* Thesis, 2015.

[56] S. Ushakov and A. Navrotsky. Experimental approaches to the thermodynamics of ceramics above 1500 °C. *Journal of the American Ceramic Society*, 95(5):1463–1482, 2012.

[57] K. Khor and Y. Gu. Thermal properties of plasma-sprayed functionally graded thermal barrier coatings. *Thin Solid Films*, 372(12):104–113, 2000.

[58] H. Chen, Y. Gao, S. Tao, Y. Liu, and H. Luo. Thermophysical properties of lanthanum zirconate coating prepared by plasma spraying and the influence of post-annealing. *Journal of Alloys and Compounds*, 486(12):391–399, 2009.

[59] J. Zhang, J. Yu, X. Cheng, and S. Hou. Thermal expansion and solubility limits of cerium-doped lanthanum zirconates. *Journal of Alloys and Compounds*, 525(0):78–81, 2012.

[60] T. Bergman, F. Incropera, D. DeWitt, and A. Lavine. *Fundamentals of heat and mass transfer.* John Wiley & Sons, 2011.

[61] P. Debye, W. Nernst, M. Smoluchowski, A. Sommerfeld, and H. Lorentz. *Vorträge über die kinetische Theorie der Materie und der Elektrizität*, volume 6. BG Teubner, 1914.

[62] C. Kittel. Interpretation of the thermal conductivity of glasses. *Physical Review*, 75(6):972–974, 1949.

[63] W. Parker, R. Jenkins, C. Butler, and G. Abbott. Flash method of determining thermal diffusivity, heat capacity, and thermal conductivity. *Journal of Applied Physics*, 32(9):1679–1684, 1961.

[64] N. Bansal and D. Zhu. Effects of doping on thermal conductivity of pyrochlore oxides for advanced thermal barrier coatings. *Materials Science and Engineering: A*, 459(12):192–195, 2007.

[65] J. Xiang, S. Chen, J. Huang, H. Zhang, and X. Zhao. Phase structure and thermophysical properties of co-doped $La_2Zr_2O_7$ ceramics for thermal barrier coatings. *Ceramics International*, 38(5):3607–3612, 2012.

[66] K. Kutty, S. Rajagopalan, C. Mathews, and U. Varadaraju. Thermal expansion behaviour of some rare earth oxide pyrochlores. *Materials Research Bulletin*, 29(7):759–766, 1994.

[67] X. Cao, R. Vassen, and D. Stöver. Ceramic materials for thermal barrier coatings. *Journal of the European Ceramic Society*, 24(1):1–10, 2004.

[68] R. Vassen, Y. Kagawa, R. Subramanian, P. Zombo, and D. Zhu. Testing and evaluation of thermal-barrier coatings. *MRS Bulletin*, 37(10):911–916, 2012.

[69] A. Bolcavage, A. Feuerstein, J. Foster, and P. Moore. Thermal shock testing of thermal barrier coating/bondcoat systems. *Journal of Materials Engineering and Performance*, 13(4):389–397, 2004.

[70] K. Bobzin, E. Lugscheider, and N. Bagcivan. Thermal cycling behaviour of lanthanum zirconate as eb-pvd thermal barrier coating. *Advanced Engineering Materials*, 8(7):653–657, 2006.

[71] R. Vassen, F. Traeger, and D. Stöver. New thermal barrier coatings based on pyrochlore/YSZ double-layer systems. *International Journal of Applied Ceramic Technology*, 1(4):351–361, 2004.

[72] L. Wang, Y. Wang, X. Sun, J. He, Z. Pan, and C. Wang. Thermal shock behavior of 8YSZ and double-ceramic-layer $La_2Zr_2O_7$/8YSZ thermal barrier coatings fabricated by atmospheric plasma spraying. *Ceramics International*, 38(5):3595–3606, 2012.

[73] R. Wellman and J. Nicholls. A review of the erosion of thermal barrier coatings. *Journal of Physics D: Applied Physics*, 40(16):R293, 2007.

[74] Standard test method for conducting erosion tests by solid particle impingement using gas jets, in ASTM G76-13, 2015.

[75] C. Ramachandran, V. Balasubramanian, and P. Ananthapadmanabhan. Erosion of atmospheric plasma sprayed rare earth oxide coatings under air suspended corundum particles. *Ceramics International*, 39(1):649–672, 2013.

[76] W. Kohn. Nobel lecture: Electronic structure of matterwave functions and density functionals. *Reviews of Modern Physics*, 71(5):1253–1266, 1999.

[77] P. Hohenberg and W. Kohn. Inhomogeneous electron gas. *Physical review*, 136(3B):864–871, 1964.

[78] W. Kohn and L. Sham. Self-consistent equations including exchange and correlation effects. *Physical Review*, 140(4A):1133–1138, 1965.

[79] W. Kohn. Density functional/wannier function theory for systems of very many atoms. *Chemical Physics Letters*, 208(34):167–172, 1993.

[80] D. Sholl and J. Steckel. *Density functional theory: a practical introduction.* John Wiley & Sons, 2011.

[81] J. Perdew, K. Burke, and M. Ernzerhof. Generalized gradient approximation made simple. *Physical Review Letters*, 77(18):3865–3868, 1996.

[82] P. Nylén, J. Wigren, L. Pejryd, and M. Hansson. The modeling of coating thickness, heat transfer, and fluid flow and its correlation with the thermal barrier coating microstructure for a plasma sprayed gas turbine application. *Journal of Thermal Spray Technology*, 8(3):393–398, 1999.

[83] Y. Goh. *Heat transfer and flow characteristics inside a gas turbine combustor.* Thesis, 2006.

[84] M. Segall, P. Lindan, M. Probert, C. Pickard, P. Hasnip, S. Clark, and M. Payne. First-principles simulation: ideas, illustrations and the CASTEP code. *Journal of Physics: Condensed Matter*, 14(11):2717, 2002.

[85] S. Clark, M. Segall, C. Pickard, P. Hasnip, M. Probert, K. Refson, and M. Payne. First principles methods using castep. *Zeitschrift fr Kristallographie-Crystalline Materials*, 220(5/6):567–570, 2005.

[86] G. Kresse and J. Hafner. Ab initio molecular dynamics for liquid metals. *Physical Review B*, 47(1):558, 1993.

[87] G. Kresse and J. Furthm*ü*ller. Efficiency of ab-initio total energy calculations for metals and semiconductors using a plane-wave basis set. *Computational Materials Science*, 6(1):15–50, 1996.

[88] G. Kresse and J. Furthm*ü*ller. Efficient iterative schemes for ab initio total-energy calculations using a plane-wave basis set. *Physical Review B*, 54(16):11169–11186, 1996.

[89] P. Blöchl. Projector augmented-wave method. *Physical Review B*, 50(24):17953–17979, 1994.

[90] G. Kresse and D. Joubert. From ultrasoft pseudopotentials to the projector augmented-wave method. *Physical Review B*, 59(3):1758–1775, 1999.

[91] F. Poulsen and N. van der Puil. Phase relations and conductivity of Sr- and La-zirconates. *Solid State Ionics*, 5356, Part 2(0):777–783, 1992.

[92] J. Perdew and A. Zunger. Self-interaction correction to density-functional approximations for many-electron systems. *Physical Review B*, 23(10):5048–5079, 1981.

[93] A. Leach. *Molecular modelling: principles and applications*. Pearson education, 2001.

[94] Z. Lu. *Mechanical properties of zirconium and zirconia systems by molecular dynamics simulation*. Ph.D. thesis, 2015.

[95] L. Verlet. Computer experiments on classical fluids. i. thermodynamical properties of lennard-jones molecules. *Physical review*, 159(1):98, 1967.

[96] R. Hockney. Potential calculation and some applications. *Methods Comput. Phys. 9: 135-211(1970).*, pages 135–211, 1970.

[97] W. Swope, H. Andersen, P. Berens, and K. Wilson. A computer simulation method for the calculation of equilibrium constants for the formation of physical clusters of molecules: Application to small water clusters. *The Journal of Chemical Physics*, 76(1):637–649, 1982.

[98] J. Lee. *Computational materials science: an introduction*. Crc Press, 2011.

[99] A. van Duin, S. Dasgupta, F. Lorant, and W. Goddard. ReaxFF: a reactive force field for hydrocarbons. *The Journal of Physical Chemistry A*, 105(41):9396–9409, 2001.

[100] T. Liang, Y. Shin, Y. Cheng, D. Yilmaz, K. Vishnu, O. Verners, C. Zou, S. Phillpot, S. Sinnott, and A. van Duin. Reactive potentials for advanced atomistic simulations. *Annual Review of Materials Research*, 43:109–129, 2013.

[101] J. Labrincha, J. Frade, and F. Marques. $La_2Zr_2O_7$ formed at ceramic electrode/YSZ contacts. *Journal of Materials Science*, 28(14):3809–3815, 1993.

[102] H. Zhou, D. Yi, Z. Yu, and L. Xiao. Preparation and thermophysical properties of CeO_2 doped $La_2Zr_2O_7$ ceramic for thermal barrier coatings. *Journal of Alloys and Compounds*, 438(1-2):217–221, 2007.

[103] H. Kido, S. Komarneni, and R. Roy. Preparation of $La_2Zr_2O_7$ by sol–gel route. *Journal of the American Ceramic Society*, 74(2):422–424, 1991.

[104] Y. Matsumura, M. Yoshinaka, K. Hirota, and O. Yamaguchi. Formation and sintering of $La_2Zr_2O_7$ by the hydrazine method. *Solid State Communications*, 104(6):341–345, 1997.

[105] J. Zhang. Novel functional graded thermal barrier coatings in coal-fired power plant turbines. Report, 2015 NETL Crossingcutting Research Review Meeting, Pittsburgh, PA, April 2015.

[106] H. Guo, R. Vassen, and D. Stöver. Atmospheric plasma sprayed thick thermal barrier coatings with high segmentation crack density. *Surface and Coatings Technology*, 186(3):353–363, 2004.

[107] M. Doerner, D. Gardner, and W. Nix. Plastic properties of thin films on substrates as measured by submicron indentation hardness and substrate curvature techniques. *Journal of Materials Research*, 1(06):845–851, 1986.

[108] W. Oliver and G. Pharr. Measurement of hardness and elastic modulus by instrumented indentation: Advances in understanding and refinements to methodology. *Journal of materials research*, 19(01):3–20, 2004.

[109] M. Gell and E. Jordan. *Bond strength and stress measurements in thermal barrier coatings.* 1995.

[110] C. Hsueh. Thermal stresses in elastic multilayer systems. *Thin Solid Films*, 418(2):182–188, 2002.

[111] P. Townsend, D. Barnett, and T. Brunner. Elastic relationships in layered composite media with approximation for the case of thin films on a thick substrate. *Journal of Applied Physics*, 62(11):4438–4444, 1987.

[112] Y. Tsui and T. Clyne. An analytical model for predicting residual stresses in progressively deposited coatings part 1: Planar geometry. *Thin Solid Films*, 306(1):23–33, 1997.

[113] X. Zhang, B. Xu, H. Wang, and Y. Wu. An analytical model for predicting thermal residual stresses in multilayer coating systems. *Thin Solid Films*, 488(12):274–282, 2005.

[114] D. Marshall, B. Lawn, and A. Evans. Elastic/plastic indentation damage in ceramics: The lateral crack system. *Journal of the American Ceramic Society*, 65(11):561–566, 1982.

[115] D. Park, M. Cho, and H. Lee. Effects of the impact angle variations on the erosion rate of glass in powder blasting process. *The International Journal of Advanced Manufacturing Technology*, 23(5-6):444–450, 2004.

[116] A. Verma and G. Lal. A theoretical study of erosion phenomenon in abrasive jet machining. *Journal of Manufacturing Science and Engineering*, 118(4):564, 1996.

[117] P. Slikkerveer, P. Bouten, F. in' t Veld, and H. Scholten. Erosion and damage by sharp particles. *Wear*, 217(2):237–250, 1998.

[118] R. Wellman and J. Nicholls. A monte carlo model for predicting the erosion rate of EB–PVD TBCs. *Wear*, 256(910):889–899, 2004.

[119] M. Schmitt, B. Harder, and D. Wolfe. Process-structure-property relations for the erosion durability of plasma spray-physical vapor deposition (PS–PVD) thermal barrier coatings. *Surface and Coatings Technology*, 297:11–18, 2016.

[120] Standard test method for thermal diffusivity by the flash method, in ASTM E1461-11, 2011.

[121] C. Xu, C. Wang, C. Chan, and K. Ho. Theory of the thermal expansion of Si and diamond. *Physical Review B*, 43(6):5024–5027, 1991.

[122] H. Hayashi, T. Saitou, N. Maruyama, H. Inaba, K. Kawamura, and M. Mori. Thermal expansion coefficient of yttria stabilized zirconia for various yttria contents. *Solid State Ionics*, 176(56):613–619, 2005.

[123] V. Viswanathan, G. Dwivedi, and S. Sampath. Multilayer, multimaterial thermal barrier coating systems: Design, synthesis, and performance assessment. *Journal of the American Ceramic Society*, 2015.

[124] C. Levi, J. Hutchinson, M. Vidal-Sétif, and C. Johnson. Environmental degradation of thermal-barrier coatings by molten deposits. *MRS bulletin*, 37(10):932–941, 2012.

[125] A. Evans, D. Mumm, J. Hutchinson, G. Meier, and F. Pettit. Mechanisms controlling the durability of thermal barrier coatings. *Progress in Materials Science*, 46(5):505–553, 2001.

[126] B. Baufeld, M. Bartsch, and M. Heinzelmann. Advanced thermal gradient mechanical fatigue testing of CMSX–4 with an oxidation protection coating. *International Journal of Fatigue*, 30(2):219–225, 2008.

[127] M. Bartsch, B. Baufeld, S. Dalkilic, L. Chernova, and M. Heinzelmann. Fatigue cracks in a thermal barrier coating system on a superalloy in multiaxial thermomechanical testing. *International Journal of Fatigue*, 30(2):211–218, 2008.

[128] D. Song, U. Paik, X. Guo, J. Zhang, T. Woo, Z. Lu, S. Jung, J. Lee, and Y. Jung. Microstructure design for blended feedstock and its thermal durability in lanthanum zirconate based thermal barrier coatings. *Surface and Coatings Technology*, 2016.

[129] C. Soares. *Gas turbines a handbook of air land and sea applications.* Butterworth–Heinemann, 2011.

[130] R. Hill. The elastic behaviour of a crystalline aggregate. *Proceedings of the Physical Society. Section A*, 65(5):349–354, 1952.

[131] R. Ingel and D. Lewis. Elastic anisotropy in zirconia single crystals. *Journal of the American Ceramic Society*, 71(4):265–271, 1988.

[132] O. Anderson. A simplified method for calculating the debye temperature from elastic constants. *Journal of Physics and Chemistry of Solids*, 24(7):909–917, 1963.

[133] L. Wu and J. Zhang. Ab initio study of anisotropic mechanical properties of $LiCoO_2$ during lithium intercalation and deintercalation process. *Journal of Applied Physics*, 118(22):225101, 2015.

[134] G. Kresse, M. Marsman, and J. Furthmüller. Vasp the guide. *http://cms.mpi.univie.ac.at/vasp/vasp/*, 2013.

[135] J. den Toonder, J. van Dommelen, and F. Baaijens. The relation between single crystal elasticity and the effective elastic behaviour of polycrystalline materials: theory, measurement and computation. *Modelling and Simulation in Materials Science and Engineering*, 7(6):909, 1999.

[136] N. Arakere and G. Swanson. Effect of crystal orientation on fatigue failure of single crystal nickel base turbine blade superalloys. In *ASME Turbo Expo 2000: Power for Land, Sea, and Air*, pages V004T01A004–V004T01A004. American Society of Mechanical Engineers, 2000.

[137] W. Tang, E. Sanville, and G. Henkelman. A grid-based Bader analysis algorithm without lattice bias. *Journal of Physics: Condensed Matter*, 21(8):084204, 2009.

[138] G. Henkelman, A. Arnaldsson, and H. Jónsson. A fast and robust algorithm for Bader decomposition of charge density. *Computational Materials Science*, 36(3):354–360, 2006.

[139] S. Plimpton. Fast parallel algorithms for short-range molecular dynamics. *Journal of Computational Physics*, 117(1):1–19, 1995.

[140] J. Crocombette and A. Chartier. Molecular dynamics studies of radiation induced phase transitions in $La_2Zr_2O_7$ pyrochlore. *Nuclear Instruments and Methods in Physics Research Section B: Beam Interactions with Materials and Atoms*, 255(1):158–165, 2007.

[141] M. Hestenes and E. Stiefel. *Methods of conjugate gradients for solving linear systems*, volume 49. NBS, 1952.

[142] M. Barsoum. *Fundamentals of ceramics*. CRC Press, 2002.

[143] B. Liu, J. Wang, Y. Zhou, T. Liao, and F. Li. Theoretical elastic stiffness, structure stability and thermal conductivity of $La_2Zr_2O_7$ pyrochlore. *Acta Materialia*, 55(9):2949–2957, 2007.

[144] A. Fischer-Cripps and B. Lawn. Stress analysis of contact deformation in quasi-plastic ceramics. *Journal of the American Ceramic Society*, 79(10):2609–2618, 1996.

[145] E. Lilleodden, J. Zimmerman, S. Foiles, and W. Nix. Atomistic simulations of elastic deformation and dislocation nucleation during nanoindentation. *Journal of the Mechanics and Physics of Solids*, 51(5):901–920, 2003.

[146] V. Dupont and T. Germann. Strain rate and orientation dependencies of the strength of single crystalline copper under compression. *Physical Review B*, 86(13):134111, 2012.

[147] M. Blanco, E. Francisco, and V. Luaña. Gibbs: isothermal-isobaric thermodynamics of solids from energy curves using a quasi-harmonic debye model. *Computer Physics Communications*, 158(1):57–72, 2004.

[148] A. Chartier, C. Meis, J. Crocombette, L. Corrales, and W. Weber. Atomistic modeling of displacement cascades in $La_2Zr_2O_7$ pyrochlore. *Physical Review B*, 67(17):174102, 2003.

[149] P. Schelling, S. Phillpot, and R. Grimes. Optimum pyrochlore compositions for low thermal conductivity. *Philosophical Magazine Letters*, 84(2):127–137, 2004.

[150] A. Maiti, G. Mahan, and S. Pantelides. Dynamical simulations of nonequilibrium processes heat flow and the kapitza resistance across grain boundaries. *Solid State Communications*, 102(7):517–521, 1997.

[151] R. Kubo. *Statistical Physics II Nonequilibrium Statistical Mechanics*. Berlin, Heidelberg : Springer Berlin Heidelberg, Berlin, Heidelberg, second edition.. edition, 1991.

[152] J. Che, T. Ca*ğ*in, W. Deng, and W. Goddard. Thermal conductivity of diamond and related materials from molecular dynamics simulations. *The Journal of Chemical Physics*, 113(16):6888–6900, 2000.

[153] P. Schelling, S. Phillpot, and P. Keblinski. Comparison of atomic-level simulation methods for computing thermal conductivity. *Physical Review B*, 65(14):144306, 2002.

[154] F. M*ü*ller-Plathe. A simple nonequilibrium molecular dynamics method for calculating the thermal conductivity. *The Journal of Chemical Physics*, 106(14):6082–6085, 1997.

[155] F. M*ü*ller-Plathe. Reversing the perturbation in nonequilibrium molecular dynamics: An easy way to calculate the shear viscosity of fluids. *Physical Review E*, 59(5):4894–4898, 1999.

[156] X. Guo and J. Zhang. First principles study of thermodynamic properties of lanthanum zirconate. *Materials Today: Proceedings*, 1(1):25–34, 2014.

[157] A. Rapp*é*, C. Casewit, K. Colwell, W. Goddard III, and W. Skiff. UFF, a full periodic table force field for molecular mechanics and molecular dynamics simulations. *Journal of the American chemical society*, 114(25):10024–10035, 1992.

[158] X. Guo, B. Hu, C. Wei, J. Sun, Y. Jung, L. Li, J. Knapp, and J. Zhang. Image-based multi-scale simulation and experimental validation of thermal conductivity of lanthanum zirconate. *International Journal of Heat and Mass Transfer*, 100:34–38, 2016.

[159] L. Wang, D. Li, J. Yang, F. Shao, X. Zhong, H. Zhao, K. Yang, S. Tao, and Y. Wang. Modeling of thermal properties and failure of thermal barrier coatings with the use of finite element methods: A review. *Journal of the European Ceramic Society*, 36(6):1313–1331, 2016.

[160] L. Wang, Y. Wang, X. Sun, Z. Pan, J. He, and C. Li. Influence of pores on the surface microcompression mechanical response of thermal barrier coatings fabricated by atmospheric plasma sprayfinite element simulation. *Applied Surface Science*, 257(6):2238–2249, 2011.

[161] M. Arai, H. Ochiai, and T. Suidzu. A novel low-thermal-conductivity plasma-sprayed thermal barrier coating controlled by large pores. *Surface and Coatings Technology*, 285:120–127, 2016.

[162] J. Keyak, J. Meagher, H. Skinner, and C. Mote. Automated three-dimensional finite element modelling of bone: a new method. *Journal of Biomedical Engineering*, 12(5):389–397, 1990.

[163] ImageJ. Available from: https://imagej.nih.gov/ij/.

[164] COMSOL. Available from: https://www.comsol.com/.

[165] Z. Wang, A. Kulkarni, S. Deshpande, T. Nakamura, and H. Herman. Effects of pores and interfaces on effective properties of plasma sprayed zirconia coatings. *Acta Materialia*, 51(18):5319–5334, 2003.

[166] B. Nair, J. Singh, and M. Grimsditch. A model for residual stress evolution in air-plasma-sprayed zirconia thermal barrier coatings. In *24th Annual Conference on Composites, Advanced Ceramics, Materials, and Structures-A: Ceramic Engineering and Science Proceedings*, volume 238, page 133. John Wiley & Sons, 2009.

[167] J. Sun. Pulsed thermal imaging measurement of thermal properties for thermal barrier coatings based on a multilayer heat transfer model. *Journal of Heat Transfer*, 136(8):081601, 2014.

[168] M. Finnis. The theory of metal-ceramic interfaces. *Journal of Physics: Condensed Matter*, 8(32):5811, 1996.

[169] D. Mumm and A. Evans. On the role of imperfections in the failure of a thermal barrier coating made by electron beam deposition. *Acta Materialia*, 48(8):1815–1827, 2000.

[170] A. Evans and J. Hutchinson. The mechanics of coating delamination in thermal gradients. *Surface and Coatings Technology*, 201(18):7905–7916, 2007.

[171] X. Guo and F. Shang. Shear strength and sliding behavior of Ni/Al_2O_3 interfaces: A first-principle study. *Journal of Materials Research*, 27(09):1237–1244, 2012.

[172] A. Christensen and E. Carter. Adhesion of ultrathin ZrO_2 (111) films on ni (111) from first principles. *Journal of Chemical Physics*, 114(13):5816–5831, 2001.

[173] X. Guo, Y. Zhang, Y. Jung, L. Li, J. Knapp, and J. Zhang. Ideal tensile strength and shear strength of ZrO_2(111)/Ni(111) ceramic-metal interface: A first principle study. *Materials & Design*, 112:254–262, 2016.

[174] M. Zhang, M. Lu, Y. Du, L. Gao, C. Lu, and H. Liu. Hardness of FeB_4: Density functional theory investigation. *The Journal of Chemical Physics*, 140(17):174505, 2014.

[175] R. Bader. Atoms in molecules. *Accounts of Chemical Research*, 18(1):9–15, 1985.

[176] S. Ogata, J. Li, Y. Shibutani, and S. Yip. Ab initio study of ideal shear strength. In *IUTAM Symposium on Mesoscopic Dynamics of Fracture Process and Materials Strength*, pages 401–410. Springer, 2009.

[177] H. Ledbetter and R. Reed. Elastic properties of metals and alloys, 1. iron, nickel, and ironnickel alloys. *Journal of Physical and Chemical Reference Data*, 2(3):531–618, 1973.

[178] A. Becke and K. Edgecombe. A simple measure of electron localization in atomic and molecular systems. *The Journal of Chemical Physics*, 92(9):5397–5403, 1990.

[179] B. Silvi and A. Savin. Classification of chemical bonds based on topological analysis of electron localization functions. *Nature*, 371(6499):683–686, 1994.

[180] T. Liang, T. Shan, Y. Cheng, B. Devine, M. Noordhoek, Y. Li, Z. Lu, S. Phillpot, and S. Sinnott. Classical atomistic simulations of surfaces and heterogeneous interfaces with the charge-optimized many body (COMB) potentials. *Materials Science and Engineering: R: Reports*, 74(9):255–279, 2013.

VITA

VITA

Xingye Guo was born in Taiyuan, Shanxi Province, Peoples Republic of China in 1984. He graduated from Harbin Institute of Technology (China) with B.S. degree in Mechanical Engineering in Jul. 2007. Then he worked in FAW-Volkswagen Automobile Co. Ltd. as a mechanical engineer in Changchun, China until Aug. 2010. Before joining Purdue University in Jan. 2013, he studied in University of Science and Technology Beijing (China) and obtained an M.S. degree in Materials Science Engineering. He is currently a Ph.D. candidate in the School of Mechanical Engineering at Purdue University. His research under the direction of Prof. Jing Zhang and Prof. Yung C. Shin focuses on thermal barrier coating materials and multiscale modeling.

LIST OF PUBLICATIONS

LIST OF PUBLICATIONS

- Jing Zhang, Xingye Guo, Yeon-Gil Jung, Li Li, and James Knapp, Lanthanum Zirconate Based Thermal Barrier Coatings: A Review, Surface and Coatings Technology, 2016 (Accepted, in press, DOI: 10.1016/j.surfcoat.2016.10.019)
- Xingye Guo, Yi Zhang, Yeon-Gil Jung, Li Li, James Knapp, and Jing Zhang, Ideal Tensile Strength and Shear Strength of ZrO2(111) / Ni (111) Ceramic-Metal Interface: A First Principles Study, Materials & Design, vol. 112, pp. 254-262, 2016.
- Xingye Guo, Bin Hu, Changdong Wei, Jiangang Sun, Yeon-Gil Jung, Li Li, James Knapp, and Jing Zhang, Image Based Multi-Scale Simulation and Experimental Validation of Thermal Conductivity of Lanthanum, International Journal of Heat and Mass Transfer, vol. 100, pp. 34-38, 2016.
- Xingye Guo, Linmin Wu, Yi Zhang, Yeon-Gil Jung, Li Li, James Knapp, and Jing Zhang, First Principles Study of Oxygen Adsorption on Nano-Structured Lanthanum Zirconate Surfaces, Physica E: Low-dimensional Systems and Nanostructures, vol. 83, pp. 36-40, 2016.
- Xingye Guo, Zhe Lu, Li Li, James Knapp, Yeon-Gil Jung, and Jing Zhang, Thermal property, thermal shock and thermal cycling behavior of lanthanum zirconate based thermal barrier coatings, Metallurgical and Materials Transactions E, vol. 3, pp. 64-70, 2016.
- Xingye Guo, Linmin. Wu, Yeon-Gil Jung, Li Li, James Knapp, and Jing Zhang, Carbon dioxide adsorption on lanthanum zirconate nanostructured coating surface: a DFT study, Adsorption, vol. 22, pp. 159-163, 2016.

- Dowon Song, Ungyu Paik, Xingye Guo, Jing Zhang, Ta-Kwan Woo, Zhe Lu, Sung-Hoon Jung, Je-Hyun Lee, and Yeon-Gil Jung, Microstructure design for blended feedstock and its thermal durability in lanthanum zirconate based thermal barrier coatings, Surface and Coatings Technology, 2016.
- Xingye Guo and Jing Zhang, First Principles Study of Thermodynamic Properties of Lanthanum Zirconate, Materials Today Proceedings, vol. 1, pp. 25-34, 2014.